Light-driven diffusioosmosis: the manipulation of colloids using azobenzene containing surfactant

David Feldmann

Univ.-Diss.

zur Erlangung des akademischen Grades
"doctor rerum naturalium"
(Dr. rer. nat.)
in der Wissenschaftsdisziplin "Experimentalphysik“

eingereicht an der
Mathematisch-Naturwissenschaftlichen Fakultät
Institut für Physik und Astronomie
der Universität Potsdam

Ort und Tag der Disputation: Potsdam, den 24.09.2018
Hauptbetreuerin: Prof. Svetlana Santer
Weitere Gutachter: Prof. Carsten Beta
Associate Prof. Arri Priimägi

Published online at the
Institutional Repository of the University of Potsdam:
URN urn:nbn:de:kobv:517-opus4-417183
http://nbn-resolving.de/urn:nbn:de:kobv:517-opus4-417183

“We wander around strictly as amateurs equipped only with some elementary physics, and in the end, it turns out, we improve our understanding of elementary physics even if we don’t throw much light on the other subjects.”

(from “Life at low Reynolds numbers”, E. M. Purcell)

ABSTRACT

The emergence of microfluidics created the need for precise and remote control of micron-sized objects. I demonstrate how light-sensitive motion can be induced at the micrometer scale by a simple addition of a photosensitive surfactant, which makes it possible to trigger hydrophobicity with light. With point-like laser irradiation, radial inward and outward hydrodynamic surface flows are remotely switched on and off. In this way, ensembles of microparticles can be moved toward or away from the irradiation center. Particle motion is analyzed according to varying parameters, such as surfactant and salt concentration, illumination condition, surface hydrophobicity, and surface structure.

The physical origin of this process is the so-called light-driven diffusioosmosis (LDDO), a phenomenon that was discovered in the framework of this thesis and is described experimentally and theoretically in this work. To give a brief explanation, a focused light irradiation induces a local photoisomerization that creates a concentration gradient at the solid-liquid interface. To compensate for the change in osmotic pressure near the surface, a hydrodynamic flow along the surface is generated. Surface-surfactant interaction largely governs LDDO. It is shown that surfactant adsorption depends on the isomerization state of the surfactant. Photoisomerization, therefore, triggers a surfactant attachment or detachment from the surface. This change is considered to be one of the reasons for the formation of LDDO flow.

These flows are introduced not only by a focused laser source but also by global irradiation. Porous particles show reversible repulsive and attractive interactions when dispersed in the solution of photosensitive surfactant. Repulsion and attraction is controlled by the irradiation wavelength. Illumination with red light leads to formation of aggregates, while illumination with blue light leads to the formation of a well-separated grid with equal interparticle distances, between 2µm and 80µm, depending on the particle surface density. These long-range interactions are considered to be a result of an increase or decrease of surfactant concentration around each particle, depending on the irradiation wavelength. Surfactant molecules adsorb inside the pores

of the particles. A light-induced photoisomerization changes adsorption to the pores and drives surfactant molecules to the outside. The concentration gradients generate symmetric flows around each single particle resulting in local LDDO. With a break of the symmetry (i.e., by closing one side of the particle with a metal cap), one can achieve active self-propelled particle motion.

KURZZUSAMMENFASSUNG

Mit Aufkommen der Mikrofluidik entstand eine größere Nachfrage nach präziser und berührungsfreier Manipulation von mikrometergroßen Objekten. In dieser Arbeit wird gezeigt, wie Bewegung im Mikrometerbereich durch ein lichtschaltbares Tensid erzeugt werden kann, deren Hydrophobizität sich durch Beleuchtung ändert. Eine fokussierte punktförmige Laserbestrahlung erzeugt einen radial nach außen oder innen gerichteten Fluss an der Substratoberfläche je nach Laserwellenlänge. Mikropartikel die sich auf der Oberfläche befinden, bewegen sich dadurch passiv mit dem Fluss entweder zum Bestrahlungspunkt hin oder vom Bestrahlungspunkt weg. Die Partikelbewegung wird in Abhängigkeit von den folgenden Parametern untersucht: Tensid- und Salzkonzentration, Bestrahlungsbedingungen, Hydrophobizität der Oberfläche und Oberflächenstruktur.

Der Grund für die Bewegung kann in einem Prozess gefunden werden, der sogenannten lichtgetriebenen Diffusioosmose (LDDO), die im Rahmen dieser Dissertation entdeckt und theoretisch sowie experimentell beschrieben wurde. Der Prozess kann wie folgt betrachtet werden: Die fokussierte Bestrahlung induziert eine lokale Photo-Isomerisation der Tensidmoleküle, die eine Monomer-Konzentrationsänderung zur Folge hat. Lokal entsteht ein hierdurch ein höherer osmotischer Druck an der Oberfläche. Um den Druckunterschied an der Oberfläche auszugleichen, wird ein hydrodynamischer Fluss nahe der Oberfläche erzeugt. Hierbei bestimmt vor allem die Wechselwirkung zwischen Tensid und Oberfläche den induzierten Fluss. Es wird gezeigt, dass die Oberflächenadsorption des Tensids vom Isomerisationszustand abhängt. Somit kann eine Bestrahlung ein Ablösen von oder Anhaften an der Oberfläche erzeugen. Diese Änderung der Oberflächenkonzentration kann als einer der Gründe für die Flussentstehung angesehen werden.

Diese hydrodynamischen Oberflächenflüssen können nicht nur durch einen fokussierten Laser erzeugt werden, sondern auch durch eine gesamte Bestrahlung der Oberfläche. Hierbei zeigen poröse Partikel eine reversible Anziehung und Abstoßung, wenn sie sich in einer Tensidlösung und an einer Substratoberfläche befinden. Die Wechselwirkung kann hierbei durch die Bestrahlungswellenlänge kontrolliert werden.

In Dunkelheit oder in rotem Licht ziehen sich die Partikel gegenseitig an, währenddessen sie sich unter blauer Bestrahlung abstoßen und ein Partikelnetz erzeugen mit äquidistanten Abständen zwischen den Partikeln. Die Partikelabstände hängen von der Partikeldichte an der Oberfläche ab und variieren zwischen 2µm und 80µm. Der Grund für die reversible Anziehung und Abstoßung wird ähnlich zu LDDO in einer lichtinduzierten Konzentrationsänderung gesehen. Tensidmoleküle adsorbieren innerhalb der Poren der Partikel. Durch eine lichtinduzierte Isomerisation werden die Moleküle ausgestoßen. Hierbei entsteht die Konzentrationsänderung um jedes poröse Partikel herum, währenddessen sie in LDDO um den Laserpunkt entsteht. Somit werden diffusioosmotische Flüsse symmetrisch um jedes Partikel erzeugt, wohingegen sie in LDDO nur um den Laserpunkt erzeugt werden.Demzufolge stoßen sich die Partikel durch eine hydrodynamische Wechselwirkung ab. Es wird gezeigt, dass aufgrund eines Symmetriebruchs durch ein Abdecken einer Partikelhälfte eine aktive selbstgetriebene Partikelbewegung erzeugt werden kann.

CONTENT

CONTENT

ABBREVIATIONS

AFM – atomic force microscope

AzoC6 – azobenzene containing surfactant with a spacer of 6 CH_2 groups

AzoCn – azobenzene containing surfactant with a spacer of n CH_2 groups

AzoC4 – azobenzene containing surfactant with a spacer of 4 CH_2 groups and a tail of 2 CH_2 groups

CMC – critical micelle concentration

DOE – diffractive optical element

DO – diffusioosmosis

EDL – electrostatic diffuse layer

ITO – Indium tin oxide

IEP – isoelectric point

LDDO – light-driven diffusioosmosis

NPD – nearest particle distance

QCM-D – quartz crystal microbalance with dissipation

PSD – particle surface density

SRG – surface relief grating

SZP – surface zeta potential

RT – room temperature

1 INTRODUCTION

This work is dedicated to a newly discovered phenomenon known as light-driven diffusioosmosis (LDDO). Diffusioosmosis (DO) has been known for decades and was described by Derjaguin as a capillary-driven flow.[1, 2] With this flow at a solid-liquid interface, he explained diffusiophoretic motion of particles in a solute gradient.[3] The model of diffusiophoresis was analyzed in more detail and was extended by Anderson and Prieve.[4–7] The physical origin of DO is rooted in the electrostatic diffuse layer, which is the nanometers thick layer in which solvent and solute organize to compensate surface charge and to balance entropy and energy—or in another view to equalize the chemical potential between bulk and surface. This diffuse layer functions as a drive for surface-induced flows. Diffusioosmosis is one kind of surface flow that is triggered by a concentration gradient in the diffuse layer. Surface flows can be induced by gradients, for example, in electric potential (i.e., electroosmosis) or temperature (i.e., thermoosmosis). Light-driven diffusioosmosis, the topic of this dissertation, belongs to the class of diffusioosmotic flows. The concentration gradient in LDDO can be directly triggered by light with a laser point of only a few micrometers. The key element of the LDDO phenomenon is a photosensitive surfactant—light triggers the change in molecular properties such as surface activity of the surfactant.

The first chapter of this work introduces photosensitive surfactants that are based on the photoisomerization of the azobenzene moiety. This molecule is the key to the light-driven surface flow. What follows is an introduction to surface flows that are related to osmotic pressure. A method and materials section covers the basic knowledge of the methods that were used in this work; this is presented in **Chapter 2**. **Chapter 3** introduces the experimental results of LDDO, i.e., an analysis of particle motion under ultraviolet (UV) and green light irradiation. In **Chapter 4** the theoretical model is described, in which diffusioosmosis is the basis in understanding the model. **Chapter 5** then focuses on the variation of different parameters, such as ionic strength, illumination, particle size and shape, and surfactant hydrophobicity. In particular,

particle motion is analyzed. In **Chapter 6** the effect of surface hydrophobicity and surface morphology on particle motion is analyzed and discussed. A more complex flow profile is presented in this chapter. In order to understand LDDO, the surfactant adsorption is measured and analyzed in **Chapter 7**. Both isomers adsorb in a different way, which is considered to be a major reason for the light-induced surface flow. Because of differences in flow direction under UV irradiation on a hydrophilic and hydrophobic substrate, both surfaces are compared. **Chapter 8** shows that not only single beams but split beams and elongated laser profiles can be utilized to structure particle ensembles in a desired fashion. **Chapter 9** introduces another effect that is considered to be related to LDDO: Porous particles show aggregation and separation depending on the wavelength of the illuminating light. Instead of point-like laser light, global illumination is required for the collective motion. When these particles are covered on one side with a metal, they are known as Janus particles. When illuminated with blue light they show an increased movement beyond Brownian motion. This motion is briefly presented and analyzed. The last two chapters show the proof of a principle, which can be seen as a starting point for further research. The last chapter closes with a final summary and conclusion.

1.1 Photosensitive surfactants based on azobenzene

Combining a surfactant with a photoactive azobenzene group has been proven to be a powerful tool to manipulate objects in the micro and nanoworld by light. For example, a cationic surfactant based on azobenzene—like in **Figure 1.1a**—binds to a backbone of an oppositely charged polyelectrolyte or DNA by ionic interaction.[8–14] The resulting complex is rendered photosensitive in this way. As a result, when it is exposed to light, an isomerization leads to physicochemical changes in the surfactant molecule. These changes are transmitted to the backbone of the polymer or DNA so that a DNA strain transforms from a coiled to an elongated state. In addition, a microgel particle can shrink or swell under irradiation depending on the irradiation wavelength.[15–18] Other effects include the swelling and shrinking of polyelectrolyte brushes [19–22] and the control of color and aggregation of gold nanoparticles in the water solution.[23]

These phenomena are attributed to changes of surfactant properties under irradiation, which is coupled to the azobenzene moiety. When it is irradiated with UV

light azobenzene itself turns from a planar, rod-like *trans* state into a kinked bulky shape – the *cis* state. A transition back to the *trans* state occurs by thermal relaxation or by irradiation with visible light back in visible light (**Figure 1.1b)**. Azobenzene's stability makes it ideal for long-living photoswitch systems in which degradation should be inhibited.[24] Under isomerization, a negligible dipole moment in the *trans* state increases up to 3 Debye in the *cis* state.[25, 26] Incorporated into the surfactant tail, the same molecule can either be hydrophobic (*trans*) or hydrophilic (*cis*). These simple changes modify several properties, for example, the critical micelle concentration (CMC), solvent solubility, interfacial energy, or the interaction with other substances.[27]

In the case of azobenzene containing surfactants, the change in the critical micelle concentration (CMC) under irradiation plays a major role. For conventional surfactant, the CMC increases by decreasing the length of the hydrophobic tail at a fixed head group.[28–31] However, in azobenzene containing surfactants, one can change the CMC just by light. Hydrophobicity can be increased by a lengthening of the alkyl part of the surfactant. In turn, the CMC can decrease multiple times. Other factors, such as size and type of the head (anionic, cationic, nonionic), additives like salt, change of pH, or other ingredients can influence its mutual interaction. Indeed, the *trans* and *cis* state of azobenzene containing surfactant can have different CMCs. For the cationic surfactant used in this work, the CMC is increased, for example, from 0.5mM to ~4mM (obtained by surface tension measurements). Therefore, photoisomerization can lead to a destruction or spontaneous formation of micelles.[32] At the solid-liquid interface, surface aggregates can be affected and undergo structural changes. This was observed for photosensitive surfactants based on spiropyran.[33]

At a solid-liquid interface, aggregation can occur at a much lower concentration, which depends on the interaction between surface and surfactant. Aggregation structures can be formed at the interface. The structure of the aggregates can vary strongly depending on the mutual interaction and surface-surfactant interaction. Atomic force microscopes (AFMs) and other studies show the formation of hemi-micelles, complete micelles, rod-shaped micelles, monolayers, double layers or multilayers, to name just a few.[34–36]

In solution, isomerization by light always leads to a mixture of surfactants present in both isomers. This results from an overlap of the absorption bands of *trans*

and *cis* isomers. The fraction of *trans*/*cis* depends on the light wavelength.[37] When a solution is illuminated for certain duration, a *photostationary* state is reached with a constant *trans*/*cis* fraction. For example, the surfactant used in this work, when irradiated at 365nm was found to be in a 1/9 (*trans*/*cis*) fraction. When followed by blue irradiation (λ = 453nm), 2/3 of the surfactant was converted to the *trans* state, whereas 1/3 remained in the *cis* state.[37] The photostationary state does not depend on the initial photostationary state of the solution. That means, a blue irradiation of a dark solution (i.e. 100% *trans*) leads mainly to a *trans*-to-*cis* photoisomerization, though, the probability to induce a *cis*-to-*trans* isomerization is larger.

Several review articles give insight into fields of azobenzene containing surfactants utilized for different purposes, such as micelle-to-vesicle transitions, interaction with DNA, rheological properties, reversible solubilization of oils, interaction with biomolecules for cell transport, and reversible droplet wettability.[38–41]

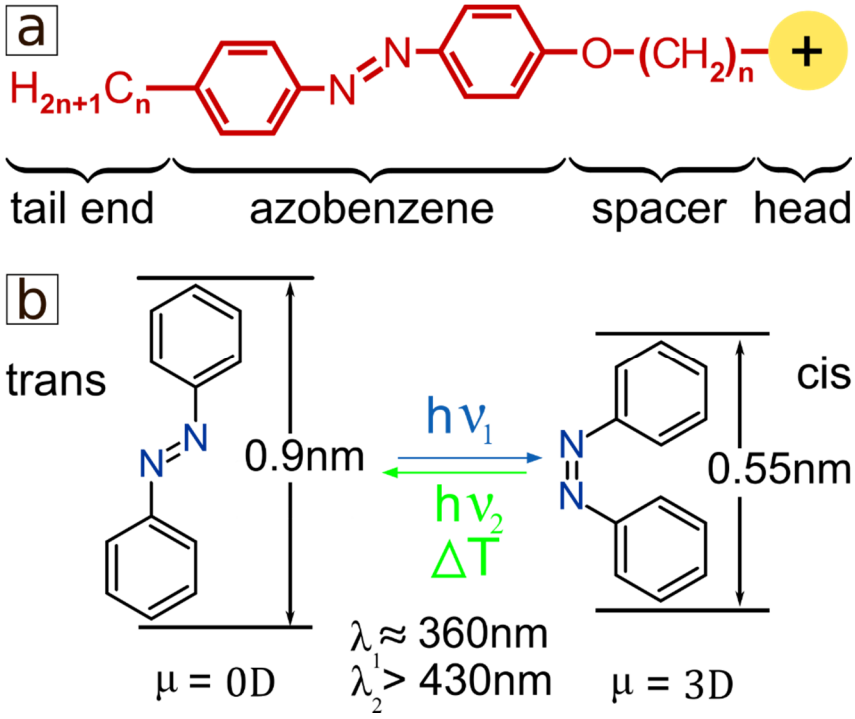

Figure 1.1. (a) Reversible photoisomerization of the azobenzene group. Absorption of UV light switches azobenzene from a stable *trans* state into a metastable *cis* state. Two routes of back-conversion are possible: light-induced under absorption of visible light and thermal relaxation. The geometric change is accompanied by a change in a dipole moment. (b) Chemical structure of the photosensitive surfactant: the azobenzene group incorporated into the tail of a cationic surfactant.

Other more detailed works have discussed systems in which azobenzene tunes light-sensitive systems with reversible properties, including control of fluid viscosity[42], gelation of polymers[43], foam stability[44–48], formation and disruption of vesicles[49], solubilization of oil substances[50], critical phase separation in water-in-decane microemulsions[51], protein folding[52], and host-guest modulation.[53–55]

In this work the focus is put on "photofluidics," in which light makes fluid and objects to move, especially at interfaces. In the following section, different kinds of surface flows that differ in the type of interface are discussed, beginning with surface flows at the liquid-air and liquid-liquid interfaces. Thereafter, a more detailed discussion is presented of flows at the liquid-solid interface, especially DO, which is referred to as a membrane free osmotic transport.[56]

1.2 Marangoni flows using azobenzene containing surfactants

Surface flows at the liquid-vapor interface can be induced by gradients in surface tension. Similar to a gradient in pressure that drives bulk water, surface tension gradients drive flows at an interface. At the liquid-air or liquid-liquid interface this type of flow is known as Marangoni flow,* which occurs when a gradient in surface tension creates a flow of the liquid layer from lower to higher surface tension. An intriguing example of this is soap boats: A coin sized boat sits on water with a soap reservoir at the end. When soap is released, surface tension is lowered, which creates a flow propelling the boat forward. Several publications have reported on Marangoni flows, sometimes also referred to as thermal capillary flows (involving surface tension gradients due to temperature gradients).[46, 47, 65–69, 57–64] Some of these publications also have reported on surface driven Marangoni flows that involve photosensitive azobenzene containing surfactant.[46, 47, 58, 60, 65, 66, 68, 69]

Microfluidics enable a great variety of applications.[40] The critical parameter for the usage in microfluidics is the reversible change of surface tension.[69–71] A continuous

* Marangoni, Carlo was an Italian physicist who explained the effect „tears of wine". Shake wine in a glass and you see that drops form at the edge, the tears of wine. Adhesion at the side of the glass pulls on the liquid which is composed of water and alcohol. Since, alcohol evaporates faster, it is depleted at the side of the glass. Surface tension of alcohol is lower than water. Thus, liquid from the bulk phase is pulled up – drops are formed. At a certain volume of the drops, they slide down because of their own weight—the glass sheds their tears of wine.

irradiation creates an equilibrium state at the interface, in which the surfactant molecules constantly ad- and desorb while being switched. For example, a solution of azobenzene containing surfactant is locally irradiated by UV light. At the interface, the surfactant molecules in the *trans* state are converted to the *cis* state. Because of the larger hydrophilicity in this state, the molecules desorb much faster into the aqueous phase. It was shown that *cis* adsorbs 10 times and desorbs 300 times faster than surfactant in the *trans* state.[72] This is mostly independent of the light wavelength but rather depends on light intensity. Therefore, continuous irradiation can greatly change the surface tension and, in turn, can lead to Marangoni flows.[73]

Switching surface tension with light gives rise to various interesting phenomena in the field of microfluidics. In microfluidics mixing is difficult due to laminar flow and low Reynolds number regime. Typically, creative microfluidic geometries are built to induce mixing. With photosensitive surfactants, other approaches have been proposed. Baigl et al. demonstrated the formation of picoliter sized water droplets containing azobenzene surfactant under UV irradiation.[74] In another case, they produced a flow of two oil phases with a third aqueous phase in between that contained an azobenzene containing surfactant. Without irradiation, the phases remained unmixed in a three-layer flow, but under irradiation with UV light, a mixing of the oil phases into droplets was achieved. When the light was switched off, the three-layer flow reappeared.[75] Similarly, dual droplets and mixed droplets of two water phases could be produced under UV irradiation in a flow of the two water phases—one with azobenzene containing surfactant—when the water phases were enclosed by oil phases.[76]

Several other phenomena based on Marangoni flows involving azobenzene containing surfactants have been demonstrated, such as trapping of oil droplets,[68] light-controlled modification of the coffee ring effect via control of particle stickiness,[77] light-structuring of evaporation patterns,[58] or light-triggered accumulation or separation of swimming particles,[78] or driving particle stabilized droplets in or against the direction of the Marangoni flow depending on the thickness of the bulk layer.[79] Also, oil drops on a water surface can be controlled by light with speeds of hundreds of µm per second.[40, 68] The remarkable speed of Marangoni flows is based on the mobility and thickness of the liquid layer. As can be seen, a great variety of complex

phenomena can arise from simple light-triggered manipulation of Marangoni flows using azobenzene containing surfactant. These phenomena have been observed at interfaces between two liquids or between liquid and vapor.

1.3 Flows at liquid-solid interfaces

Surface flows at the solid-liquid interface are different in nature than liquid-air interfaces. A solid phase is very dense, can be crystalline or amorphous, and interacts with the solvent and solute molecules. The surface chemistry and structure affect their interaction, which can be attractive or repellent. When the solute or solvent contacts the solid surface, reactions can occur, which can modify the surface by oxidation, for example. Liquid motion at a solid-liquid interface is subject to a no-slip boundary condition which limits the speed of hydrodynamic flows compared to Marangoni flows.

The key property that gives rise to hydrodynamic flows induced at a solid-liquid interface is the formation of the electrostatic diffuse layer (EDL). When a solid surface is exposed to water, an interaction potential attracts or repels solute. As a result, an excess or depletion of solute at the interface is created to equalize the chemical potential of the solution at the surface.

This work focuses primarily on diffusioosmotic flows driven by light. Diffusioosmosis belongs to the category of surface-driven flows, which are generated along a flat and solid surface by a gradient in concentration of solute. The term osmosis is commonly known and mostly associated with flows through a semipermeable membrane. Diffusioosmosis, however, does not include a membrane. To clarify these terms, the origin of osmosis is discussed, and the traits of diffusioosmotic surface flows are presented in the following.

1.4 Osmosis and osmotic pressure

The word osmosis has its origin in the Greek language and stems from the word *ōmos* which means *a push*. The term osmosis is defined by Encyclopedia Britannica as "the spontaneous passage or diffusion of water or other solvents through a semipermeable membrane (one that blocks the passage of dissolved substances—i.e. solutes)." This motion of water through a semipermeable membrane is created by a pressure difference on both sides of the membrane. This pressure difference can be

measured by exerting pressure on the side into which the water flows. The pressure at which the flow stops is commonly referred to osmotic pressure Π. As a simple example, a selective membrane separates a water bath from a water bath with dispersed solutes. The chemical potential of pure water is higher than that of water with added solutes. Therefore, osmotic pressure builds up and drives the water into the water bath with added solutes. In this case, van't Hoff proposed the law of osmotic pressure for dilute solutions:

$$\Delta\Pi = k_B T \Delta c$$

where k_B is the Boltzmann constant, T the temperature, and Δc the solute concentration difference between the two reservoirs. On the microscopic scale, a selective membrane consists of nanochannels that are open for water but impenetrable for solute molecules. When a solute molecule hits the aperture of the nanochannel, a force pushes the solute away from the channel. The viscous forces in the fluid drag the surrounding molecules and solvent with the repelled solute molecule away from the membrane creating a layer of lower pressure. The net effect is a force acting on the whole solution. Therefore, osmotic pressure is a result of Brownian motion.[80, 81] The interaction between solute and channel aperture can be described as a potential or energy barrier for the solute molecules.[81, 82] This picture, however, can be seen for noninteracting solute molecules. It changes when forces such as electrostatics are involved.

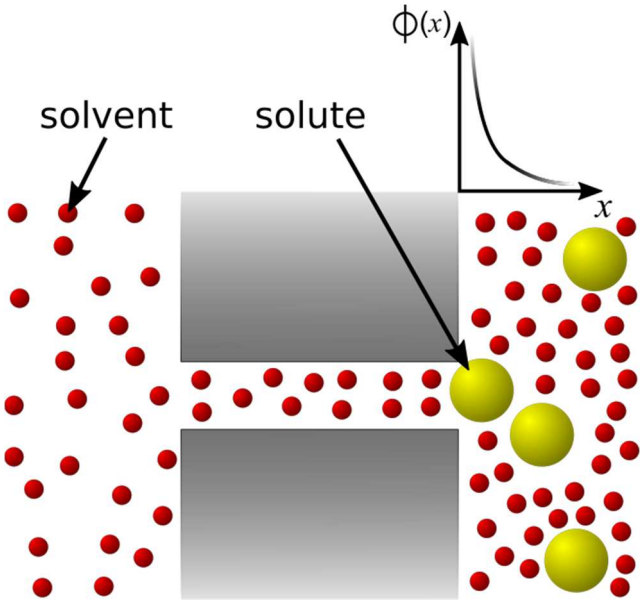

Figure 1.2. Simple model for osmosis. A membrane, impermeable to solute but permeable to solvent divides two reservoirs. The impermeability is described as a potential $\Phi(x)$. Solute molecules are repelled from the channel opening. Fluid around the solute molecule is dragged with it, creating a region of low pressure at the channel opening. More solvent molecules move into the reservoir on the right side.

What follows is a short derivation of the osmotic flow for dilute solution in order to compare it to DO flow. Marbach et al. demonstrated a mechanical approach, which facilitates an understanding of the connection between osmosis and DO.[82] Microscopically, pores can be seen as nanosized channels with length L. These channels are permeable for water but not for solute molecules. In case of an absent concentration gradient—equal concentrations on either side of the channel—there is still a flux through the membrane due to a pressure drop: $Q = \mathcal{L}_{hyd}\Delta p$, with Q the flux of water through the membrane and $\mathcal{L}$ the solvent permeance. One can describe impermeability by a potential Φ close to the channel opening. A solute molecule experiences a force $-\partial_x\Phi$ when it approaches the channel opening. Because solute molecules directly interact with solvent molecules, this force is translated to the fluid. In the regime of low Reynolds numbers, the force balance can be described by Stokes equation:

$$\partial_x p - \eta\nabla^2 v = c(x)(-\partial_x\Phi(\mathrm{x})) \tag{1}$$

where η is the viscosity and v the velocity of the fluid. The fluid flow is induced by a pressure drop: $-\partial_x \mathcal{P} = \partial_x p + c(x)\big(-\partial\Phi(x)\big)$. With integration this yields

$$-\Delta\mathcal{P} = -\Delta p + \sigma\Delta\Pi \tag{2}$$

with $\Delta\Pi$ the osmotic pressure difference and σ the rejection factor, a dimensionless factor with $|\sigma| \leq 1$, which is solute, solvent, and membrane-specific and usually reduces the osmotic pressure. In case of a fully solute-impermeable membrane and with $\sigma \to 1$, **Equation (2)** yields the known result: $-\Delta\mathcal{P} = -\Delta(p + \Pi)$. That is, the overall pressure drop results from the hydrostatic pressure and the osmotic pressure due to solute molecules. This results in a flux of water through the membrane by $Q = -\mathcal{L}_{hyd}\Delta(p - \Pi)$.

1.5 Electroosmosis

In the case of ionic solution, the surface charge is balanced by a counterion cloud; seen from the bulk, the surface appears to be neutral, taking into account surface charge plus counterion cloud. Separately, the surfaces bear a finite charge. When an electrical potential is applied along the surface, a net body force is applied to the fluid: $\rho_e \nabla\Phi$, with ρ_e the charge density and the total potential $\Phi = \psi + \phi$, where ϕ is the applied electric potential and ψ the potential at the Helmholtz plane. As stated in the experimental part, this potential ψ can be accessed by zeta potential measurements. The electrical body force drives a hydrodynamic surface flow (only in the diffuse layer) known as electroosmosis and was first observed at the beginning of the nineteenth century by Reuss.[83, 84] He observed not only electroosmosis but also the motion of clay particles, which is known as electrophoresis. The term phoresis means “migration” and refers to the motion of colloids. Phoresis has the same origin as electroosmosis, but the flow is generated along the particle surface, dragging the particle through the fluid. Indeed, it took around one century to explain this motion of apparently negative particles.[84] Electrophoresis and electroosmosis are driven by an electrical potential gradient.

1.6 Diffusioosmosis

In contrast to osmosis, DO describes flows at a solid-liquid interface driven by a solute concentration gradient in a thin interfacial layer.[1, 4–7, 85–87] Diffusioosmosis can be used to create osmosis in fully permeable nanochannels by a solute gradient between two baths connected by these nanochannels.[88, 89] The flow induced in diffusioosmosis is able to drive, for example, spherical particles in a solute gradient. If the diffusioosmotic flow is generated on the particle surface, the particle itself starts to move while it is pushed or pulled by the flow through the solvent. This particle motion is known as diffusiophoresis with neutral or electrolyte solute.[1, 4–7, 85–87]

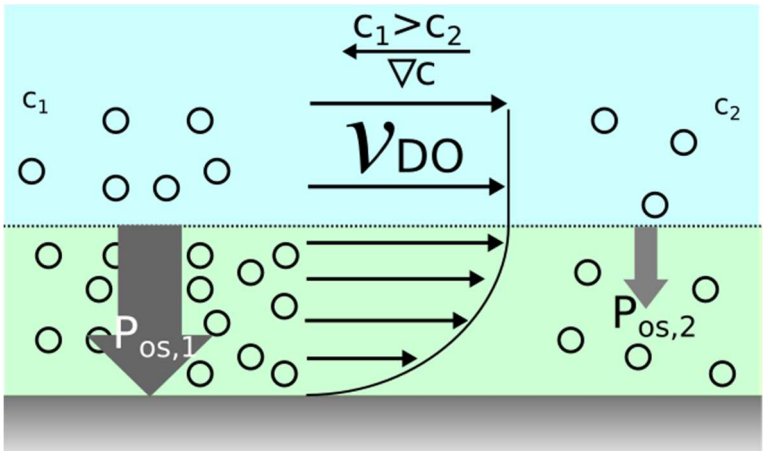

Figure 1.3. Diffusioosmosis in a gradient of neutral molecules. Solute concentration near an interface differs from solute concentration in the bulk. This results in a concentration gradient at the interface. In an interfacial region, called the diffuse layer, solute molecules interact with the solid surface. When interaction is attractive, as in this scheme, solute molecules accumulate in the diffuse layer. The concentration gradient normal to the surface generates osmotic pressure (large arrows). Because of the large scale concentration gradient along the surface, osmotic pressure drops from the region of large surface excess to the region of low surface excess. This drives a hydrodynamic flow toward the region of low surface excess. Hydrodynamic flow develops in the diffuse layer, in which saturation results in the slip velocity v_{DO}. The flow is driven by the osmotic pressure gradient and hampered by the viscous stress due to the no-slip boundary condition. The balance between both determines the slip velocity. The resulting shear induces a flow in the interfacial region towards low concentration, but only when there is an attractive interaction between solute and surface.

A scheme of diffusioosmosis with neutral solute molecules is depicted in **Figure 1.3**. When neutral solute molecules diffuse near a solid-liquid interface, they interact with

the interface, for example, through van der Waals forces. Interaction could be attractive or repulsive and depends on the solvent. Near the interface a thin EDL layer is generated with an increase or decrease of solute molecules compared to solution. Due to Brownian motion, this diffuse layer expands some distance away from the surface, which is in the range of nanometers. The thickness of the EDL is denoted as λ Interaction can be described by a potential Φ that depends on the distance to the surface. Away from the diffuse layer, solute molecules do not "feel" the surface and the potential is nearly zero $\Phi(z > \lambda) \approx 0$. Inside the diffuse layer, the balance between attraction and Brownian motion leads to a concentration profile following Boltzmann distribution:

$$c(z) = c_\infty \, e^{-\frac{\Phi(z)}{kT}} \tag{3}$$

where c_∞ is the concentration of solute in the bulk. Depending on the interaction type, the potential Φ(z) can be attractive or repulsive. In the scheme, attractive interaction leads to an accumulation of solute near the surface. Due to an increased (or decreased) concentration gradient normal to the interface, a pressure gradient is induced. This gradient is balanced by a hydrostatic pressure gradient. If a concentration gradient is imposed in the bulk parallel to the surface, the concentration profile follows:

$$c(x,z) \approx c_\infty(x) \exp\left(-\frac{\Phi(\mathrm{z})}{\mathrm{k_B}T}\right) \tag{4}$$

This holds true if it is assumed that the equilibrium in *z* (normal to surface) is reached much faster than the gradient in *x* is relaxed. In local equilibrium the chemical potential near and far away from the surface should be the same:

$$\mu[c(x)] + \Phi(\mathrm{z}) \cong \mu[c_\infty(x)] \tag{5}$$

With $\mu(c) = k_B T \ln\left(\frac{c}{c_\infty}\right)$ in the dilute regime, the result above is yielded. Using the local equilibrium condition from **Equation (5)**, one derives the local force acting on a unit volume of the fluid: [82]

$$c\left(-\partial_z \Phi(z)\right) = c\partial_z \mu = c\partial_z \left(\frac{\partial f}{\partial c}\right) \equiv \partial_z \Pi(c) \tag{6}$$

In which $f = \frac{F}{V}$ is the Helmholtz free energy density. The transport in the fluid is similarly approached as in osmosis through a membrane, starting from Stokes equations[†]:

$$\nabla p - \eta \nabla^2 v = -c(x,z)\nabla\Phi(\mathrm{z}) \tag{7}$$

The z-projection (normal to the surface) of **Equation (7)**, taking into account $v_z = 0$, yields

$$\partial_z p(x,z) - \partial_z[\Phi(z)c(x,z)] = 0 \tag{8}$$

Combining **Equation (6)** and **(8)** results in

$$\partial_z p = \partial_z \Pi(c) \tag{9}$$

Therefore, when in equilibrium, the hydrostatic pressure gradient $\partial_z p$ balances the osmotic pressure gradient $\partial_z \Pi$ in z direction. Now the total pressure difference is found to be

$$p(x,z) - p_\infty = \Pi\big(c(x,z)\big) - \Pi(c(\infty)) \tag{10}$$

The fluid velocity along the surface can be calculated using **Equation (10)** and **(7)** projected on the *x*-axis:

$$\partial_x \left(\Pi\big(c(x,z)\big) - \Pi(c(\infty)\big) = \eta \partial_z^2 v_x \tag{11}$$

Integration leads to the velocity component in *x* direction, which is only induced in the thin interfacial layer:

[†] To the complete set of Stokes equations belongs the continuity equation: $\nabla \cdot \vec{v} = 0$

$$
\begin{aligned}
v_x(x,z) &= \frac{1}{\eta}\int_0^{z'} dz \int_{z'}^{\infty} dz''(\Pi(\mathrm{c}_\infty(x)) - \Pi(c(x,z'))) \\
&= \frac{1}{\eta}\int_0^{z'} dz \int_{z'}^{\infty} dz''\big(\mathrm{c}_\infty(x) - c(x,z'')\big)\,\partial_x\mu\big(c_\infty(x)\big) \\
&= -\frac{1}{\eta}\int_0^{\infty} dz' z' \left(\frac{c(x,z')}{c_\infty(x)} - 1\right)\partial_x\Pi(c_\infty(x)) \\
&= K_{DO}\,\partial_x\Pi\big(c_\infty(x)\big)
\end{aligned} \tag{12}
$$

This version of the diffusioosmotic flow includes the gradient in osmotic pressure. This result was first derived by Anderson and Prieve when they described the slip velocity (velocity at the edge of the diffuse layer) as a function of the gradient of the bulk concentration gradient along the surface:

$$v_s(x,z) = -\frac{\mathrm{kT}}{\eta}\mathrm{L}\times\mathrm{K}\nabla\mathrm{c}_\infty(\mathrm{x}) \tag{13}$$

with $L = \frac{1}{K}\int_0^\infty z\left[(\exp\left(\frac{\Phi(z)}{kT}\right) - 1\right]dz$ the characteristic size of the diffusive layer and $K = \int_0^\infty \left[(\exp\left(\frac{\Phi(z)}{kT}\right) - 1\right]dz$ the adsorption of solute, normalized by c_∞. The term under the integral can be written in different ways. To understand the similarity of **Equation (13)** and **(12)**, the integral term is a result of the concentration difference:

$$
\begin{aligned}
c(x,z) - c_\infty(x) &= c_\infty(x)\exp\left(\frac{\Phi(z)}{kT}\right) - c_\infty(x) \\
&= \left[(\exp\left(\frac{\Phi(z)}{kT}\right) - 1\right]c_\infty(x) \\
&= \left[\frac{c(x,z)}{c_\infty(x)} - 1\right]c_\infty(x)
\end{aligned} \tag{14}
$$

Diffusioosmosis can be described in several ways, for example, by a gradient in osmotic pressure[82], bulk concentration[7], or chemical potential.[90] The following section describes LDDO in terms of the concentration gradient.

With the previous introduction to DO in mind, LDDO is described similarly described in **Chapter 4**. However, LDDO differs from DO, which is described above. The solute in LDDO is a cationic surfactant that is photoswitchable. Due to electrostatic interaction, an EDL is formed. In general, DO can have two different contributions to the flow: electroosmotic and chemiosmotic. Chemiosmosis results from a difference in

concentration, whereas electroosmosis results from an electrical field that is induced by a separation of ions and counterions in a concentration gradient. In the case of neutral molecules, DO is driven only by chemiosmosis. In concentration gradients of salt, however, electroosmosis and chemiosmosis contribute to the flow. In the specific case of LDDO, we assume only chemiosmosis as a driving force because the total concentration of surfactant remains uniform everywhere. The special characteristic of the surfactant relies on its photoactivity. Its property changes at a *trans-cis* isomerization lead to differences in surface-surfactant interaction potential and, therefore, concentration differences in the EDL under isomerization. At concentrations around the CMC, irradiation destroys micelles. When micelles are destroyed, the bulk concentration of monomeric surfactant is increased. On the surface, this leads to a higher osmotic pressure. When the light is focused, this concentration gradient can become large and induce a DO flow. The flow can be induced in the simplest way—by a point-like laser spot, which directs to or away from the laser spot. This flow was termed LDDO, and observations and theory are explained in the following chapters.

2 EXPERIMENTAL PART

2.1 Materials

2.1.1 Azobenzene containing surfactant

The "central actor" of this work is an amphiphilic molecule that consists of a charged head group and hydrophobic tail (**Figure 2.1**). At the air-water interface, the hydrophilic part points into water and the hydrophobic part extends into air. In this way, the surface energy of water is lowered by the addition of amphiphilic molecules. Due to their tendencies to align at interfaces, these molecules are known as surface active agents, or simply surfactants. The surfactants used in this work are photosensitive, which means they change their physicochemical properties under light irradiation. These surfactants are composed of an alkyl chain that acts as a hydrophobic tail and an ammonium bromide head group that is positively charged (cationic surfactant) in water. What makes the surfactant reactive to light is an azobenzene group. Azobenzene adopts two conformations: a stable *trans* state and a metastable *cis* state. Under the absorption of UV light, azobenzene photoisomerizes from the *trans* state to the *cis* state. Irradiation with visible light or thermal relaxation returns the azobenzene to the *trans* state. When this azobenzene containing surfactant is dissolved in water, it adopts a photostationary state that depends on the irradiation conditions. When the solution is kept in the dark, the dissolved molecules are found to be 100% in the *trans* state (despite fluctuations). Continuous irradiation at 365nm leads to a photostationary state, during which more than 90% of the molecules are found to be in a *cis* state. Continuous irradiation with a simple blue LED (emission maximum at 442nm) leads to a state in which around 66% of the molecules are in a *trans* state and 34% in a *cis* state.

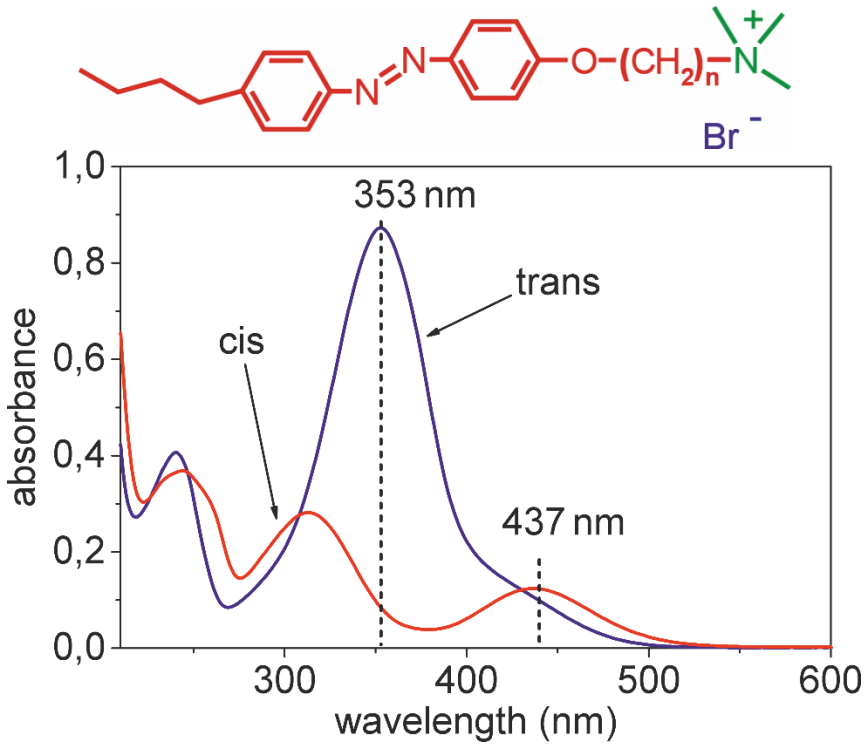

Figure 2.1. The absorption spectra of *trans* (blue line, relaxed in the dark) and *cis* (red line, UV illuminated) isomers of azobenzene containing surfactant shown above with n = 6.

The life time of *cis isomer*s in the dark is around 48h. The absorption spectra[‡] of azobenzene containing surfactant with n = 6 in water is plotted for both a dark (*trans*) solution and a UV irradiated (*cis*) solution (**Figure 2.1**). The absorption maximum for the *trans* state is 353nm, which corresponds to the $\pi - \pi^*$ transition of the azo-bond. Due to symmetry breaking, a *trans* to *cis* isomerization occurs along the symmetrically forbidden $n - \pi^*$ band under illumination of light at 437nm—with low efficiency, however. After sufficient UV illumination, two maxima of the azobenzene can be found—around 314nm and 442nm. Another characteristic peak around 243nm is assigned to the benzene rings. Under irradiation with green light (532nm), the surfactant can be switched from *cis* to *trans*. UV/vis spectra reveal that illumination of dark solution (100% *trans*) with green light can switch some molecules from *trans* to *cis*. Under irradiation, the properties of the azobenzene change significantly: the shape

[‡] Spectroscopy performed by a Cary 5000 UV-Vis-NIR spectrophotometer (Varian Inc.)

switches from “rod-like” to kinked, and the dipole moment increases from 0 D to ~3D in a *trans* to *cis* isomerization. This means that under irradiation one can reversibly trigger the hydrophilicity of the surfactant and thus change its solubility, critical micelle concentration (CMC), and strength of interactions with other substances.

The synthesis of the azobenzene containing surfactant was conducted by another group member according to the scheme reported elsewhere.[91] Different surfactants of the same type have been used with variations only in the spacer (n = 6, 8, 10, 12), and another surfactant with a spacer of n = 4 and tail with only 2 methyl groups instead of 4. The corresponding abbreviations for these surfactants are AzoC6, AzoC8, AzoC10, AzoC12, and AzoC4 (for convenience). If not explicitly mentioned, the surfactant with n = 6 is typically used. The CMC of the surfactant in aqueous solution is 0.5mM (AzoC6), 0.18mM (AzoC8), 0.06mM (AzoC10), and 0.04mM (AzoC12).[14] The surfactants were dissolved in water (MilliQ) with different initial concentrations and kept in the dark to ensure complete relaxation to the *trans* state. Thereafter, the solution was diluted to the appropriate concentration for subsequent experiments. The water solubility of AzoC12 is strongly reduced in the *trans* state, and only low concentrations are possible. In this case, water solubility can be much increased under irradiation with UV light.

2.1.2 Particles

Silica particles of different sizes were obtained from Micromod GmbH or Microparticles GmbH, Germany. Micromod particles are manufactured in such a way that particles at sizes larger than 3µm in diameter are porous with a BET[§] value of 850m^2/g and a mean pore diameter of 6nm. All nonporous silica particles with diameters above 3µm were obtained from Microparticles GmbH. All particles were delivered in 5 w% aqueous dispersions.

2.1.3 Substrates

The glass substrates are cover slips (borosilicate, hydrolytic class 1) of

[§] The BET value gives the surface area obtained from adsorption isotherms of gas in the pores applying varying pressure. The theory for surface area calculation was given by Brunauer, Emmet and Teller in 1938.[166]

24x50mm size and thickness between 0.13mm and 0.17mm (VWR International GmbH or Carl Roth GmbH + Co. KG). For the preparation of hydrophobic substrates, a soluble fluoropolymer resin (Teflon™ AF 1600, DuPont de Nemours GmbH, Deutschland) was used. It was dissolved in Fluorinert™ Fluid FC-77. UV-transparent microchannels (µ-Slide VI 0.1/0.4 Uncoated, Ibidi GmbH, Germany) with thickness of 0.4mm and 0.1mm were used for irradiation measurements. The investigating fluid was pipetted into the channel with a volume of 65µl and sealed with Parafilm (Bemis Company, Inc., USA) to avoid evaporation.

All chemicals were obtained from Sigma-Aldrich if not stated otherwise.

2.2 Methods

All experiments were conducted in room temperature if not explicitly mentioned differently.

2.2.1 Optical microscopy

An inverted optical microscope (Olympus, model: IX71) was utilized to visualize particle motion. A scheme of the setup is given in **Figure 2.2**. It is equipped with four objectives: 4x, 10x, 20x, 40x. A monochromatic light source (Polychrome, Agilent Technologies) replaces the bright light source typically used for imaging microscopy. Since the photostationary state depends on the illumination wavelength, this light source gives full control over the photostationary state of the sample. Normally, it illuminates at 600nm (red light) to inhibit undesired isomerization. The whole setup is also kept under red light (λ = 600nm) or in the dark to prevent any undesired isomerization from external sources. To induce diffusioosmotic flows, two lasers are coupled into the microscope: a UV laser (Genesis CX, 355nm, Coherent Inc., USA) and a green laser (Samba, 532nm, Cobolt, Sweden). The green laser is directed through a system of mirrors (giving enough degrees of freedom for adjustment). Before coupling into the microscope, the beam is widened and collimated by two lenses. It then enters the microscope through the back port and is directed into the optical infinity light path of the microscope by a dichroic mirror (DMLP550R, Thorlabs GmbH, Germany). The UV laser is coupled into a single mode fiber (SM300, Thorlabs GmbH, Germany), decoupled, and collimated. Before entering through the side port of the

microscope, it can be manipulated by other optical elements, such as a cylindrical lens or an iris, to change the beam shape and diameter.

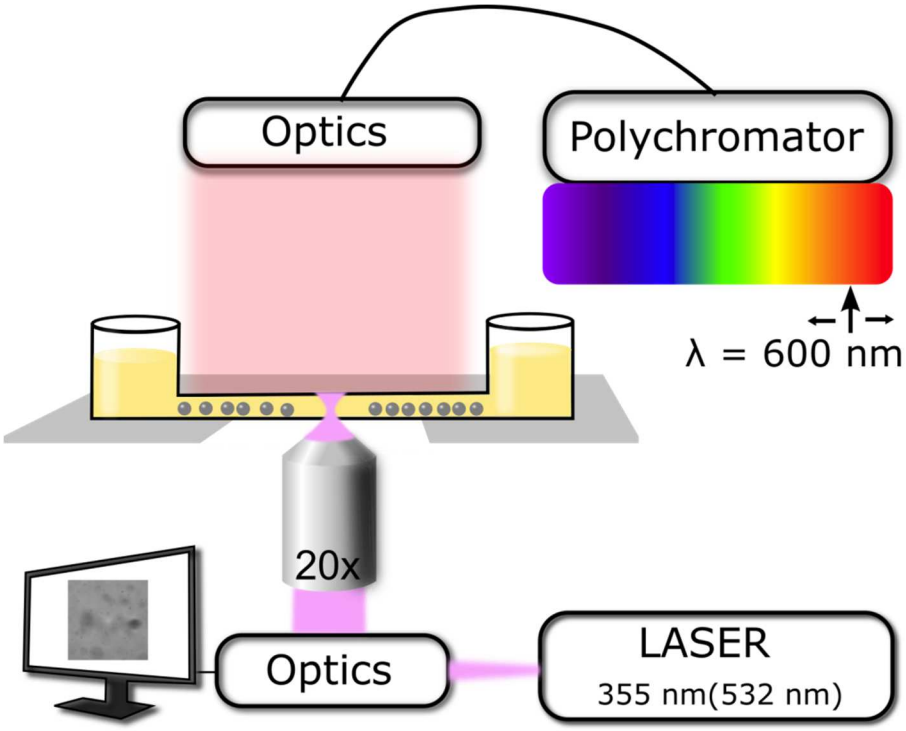

Figure 2.2. Scheme of microscopy setup. A UV laser is coupled to the side port of the microscope, and the green lasers enters the microscope through the back port. A system of mirrors and lenses collimates the beam before it enters the microscope. The size and shape of the beams can be altered by a cylindrical lens or an iris located in the beam path. A filter wheel equipped with several wavelength dependent filters selects the beam that is directed into the beam infinity path of the microscope. An objective focuses the beam onto the surface of the sample leading to LDDO at the sample surface driving particle motion. Illumination wavelength can be chosen by a polychromator. The red light illuminates the sample in order to inhibit undesired isomerization.

A fixed built-in mirror located inside the microscope directs this beam into the observation path. A filter wheel can be rotated to choose a wavelength dependent filter, which directs the beam into the infinity beam path. The filter for 532nm does not transmit UV light completely, but it transmits sufficient UV light to simultaneously irradiate with UV and green light. The collimated beams are focused onto the focal plane through the objective and onto the solid-liquid interface. Particle motion is imaged by a monochromatic camera (Olympus XM10) which acquires image sequences of a maximum of 13 frames per second. The laser power was measured by

an optical power meter 1918-R with a sensor 918D-UV-OD3R (Newport Corp., Irvine, CA, USA).

2.2.2 Tracking and data analysis

Single particle tracking was done with the Mosaic Single Particle Tracking plugin[92] for ImageJ.[93] Each particle position at each frame was exported into a table. This data was further analyzed by a self-written script for the software MATLAB.[94]

2.2.3 Quartz crystal microbalance

Surfactant adsorption from aqueous solution on solid substrates was monitored (in real-time) by a quartz crystal microbalance with dissipation (QCM-D, model: Q-Sense E4, Biolin Scientific Holding AB, Sweden).

The quartz crystal is piezoelectric which means it deforms in an electrical field. When an alternating electrical field is applied to the quartz crystal at its resonance frequency, the crystal oscillates. When mass is added to the crystal, the resonance frequency shifts. Sauerbrey[95] found the relation between frequency shift and added mass:

$$\Delta m = -\frac{\Delta f \rho_d \nu_d}{n} = -\frac{C\Delta f}{n}$$

with n the overtone number of the oscillation for n = 1, 3, 5, 7, etc.[**] This is valid for two conditions: the added mass is 1) much smaller than the crystal mass or 2) rigidly adsorbed to the surface. When the electric field is turned off (or the voltage on electrodes is switched off), the oscillation decays. The decay time is related to the dissipation factor D:

$$D = \frac{1}{\pi f_0 \tau}$$

with f_0 the resonance frequency and τ the decay time. This is related to the dissipated energy of the system. Dissipation plays a role when the surface is not rigidly adsorbed. As a result, it is possible to analyze not only the adsorbed amount but the viscoelastic properties of the adsorbed layer.

[**] The crystal oscillations are shearing oscillations. A standing wave is induced at resonance frequencies and its overtones. When n is even, waves interfere destructively. Thus, only odd numbers are used.

The system consists of a pump and a measurement chamber in which four measurement cells can be implemented for simultaneous measurement of up to four sensors. The fluid is dragged through microtubing and the cells. Before the surfactant is injected, the cells are rinsed thoroughly with water until the temperature is equilibrated at 20°C and the frequency shift remains constant. When the surfactant solution is dragged into the system and the cells are flushed, surfactant adsorbs to the sensor surface. Since the molecules adsorb continuously up to a saturation amount, the frequency shift over time is recorded. From this, it is possible to analyze the adsorption kinetics.

For measurements of adsorption isotherms, each stepwise increase of concentration was done after the equilibration of the frequency shift, including frequency shifts of less than 0.2Hz in 5 minutes. The third frequency overtone was selected, and for each concentration the equilibrium surface adsorption Γ given in ng/cm^2 was calculated using the Sauerbrey relation. The Sauerbrey approximation is applied when $\frac{\Delta D_n}{\Delta f_n/n} \ll 4 \cdot 10^{-7}\mathrm{Hz}^{-1}$.[96] Besides noise errors, this holds true for all conducted measurements. In addition, if the ratio of $\Delta f(n)/n$ yields the same results, Sauerbrey is considered to be trustworthy. Because these conditions were fulfilled, the Sauerbrey equation was applied to calculate all mass changes.

The measurements were conducted in a continuous flow of surfactant solution over the sensor surface. All measurements were done in the dark to prevent unintentional photoisomerization.

In this work, the adsorption of azo-surfactant solution onto glass (Borosilicate) and coated Teflon (Teflon AF 1600, DuPont) was measured. All sensors were distributed from LOT-QuantumDesign GmbH. These sensors were chosen to model surfactant adsorption to a microscopic glass slide and the Teflon AF1600 coated glass slide used in LDDO observations. Before measurement, the sensors were cleaned according to the cleaning protocol from Biolin Scientific: for a Borosilicate-coated surface, the sensors were treated with either UV/ozone (UV/Ozone ProCleaner™, Bioforce Nanosciences Inc., USA) or a plasma cleaner (PDC-32 G, Harrick Scientific Inc., USA) using ambient air as plasma for 10 minutes, then kept in 2% Sodium Dodecyl Sulfate (SDS) aqueous solution for 30 minutes, and rinsed in milliQ water, dried with nitrogen gas, and finally treated with UV/ozone or plasma cleaner for 10

minutes. Teflon-coated sensors are more sensitive to cleaning and were only treated with milliQ water and dried under continuous flow of nitrogen, as recommended by the manufacturer.

2.2.4 Contact angle and surface tension measurement

Glass surfaces are typically hydrophilic, whereas Teflon-coated glass surfaces are highly hydrophobic.

When a droplet sits on a solid surface (sessile drop) three interfacial tensions determine the contact angle: the solid-liquid γ_{SL}, the solid-vapor γ_{SV}, and the liquid-vapor γ_{LV}. The relation between those parameters is the so-called Young's equation[97]:

$$\gamma_{\mathrm{LV}} = \gamma_{\mathrm{SV}} \cdot \cos\theta + \gamma_{SV}$$

where θ is the contact angle.

Static contact angle and surface tension was measured with a SURFTENS Basic (OEG GmbH, Germany). To analyze the contact angle of a substrate, a droplet of water was carefully dispensed onto the surface of the substrate, and contour images of the drop are recorded by a CCD. To ensure a clear contour of the droplet, a red LED is mounted at the other end of the setup behind the droplet. The dispensing system is based on a syringe fixed to the system from the top so that its needle points onto the substrate. Micrometer screws ensure a careful generation of a droplet at the tip of the needle, which is placed onto the surface. The SURFTENS software detects the contact line between liquid and solid (baseline) and fits the countour of the droplet by an ellipse or polynomial. With this data, it calculates the contact angle. In the same setup, the surface tension (liquid-air interface) was measured by the pendant drop method.[98, 99] This method is based on the analysis of the droplet shape formed at the end of a capillary. Because of the gravitational force, the droplet becomes pear-like in shape instead of spherical. The contour of the droplet is monitored by a camera. From the profile of the droplet, the surface tension of the liquid is calculated. The calculation is based on the Young-Laplace equation[100, 101]:

$$\Delta p = \gamma_{LV}\left(\frac{1}{R_1} + \frac{1}{R_2}\right)$$

Where Δp is the pressure difference between the inside and the outside of the droplet, R_1 and R_2 are the principal radii of curvature (in plane of image and normal to the

imaging plane).[102]

For surface tension measurements of azo-surfactant solution, the setup was kept in the dark or in red light to prevent isomerization. When the *cis*-enriched solutions were measured, the solution was illuminated with UV light for 10 minutes beforehand. The volume of the droplet was carefully increased until the weight reached the critical point at which a further increase in volume would make the droplet to drip off the tip of the needle. This ensures that gravity is strong enough and that the measurement yields correct results. The surface tension of azobenzene containing surfactant solution is shown in **Figure 2.3** for different irradiation condition (i.e. dark, UV, blue). From these measurements the CMC was measured around 0.5mM for *trans* surfactant and around 4mM for UV illuminated (i.e. *cis* dominated) solution.

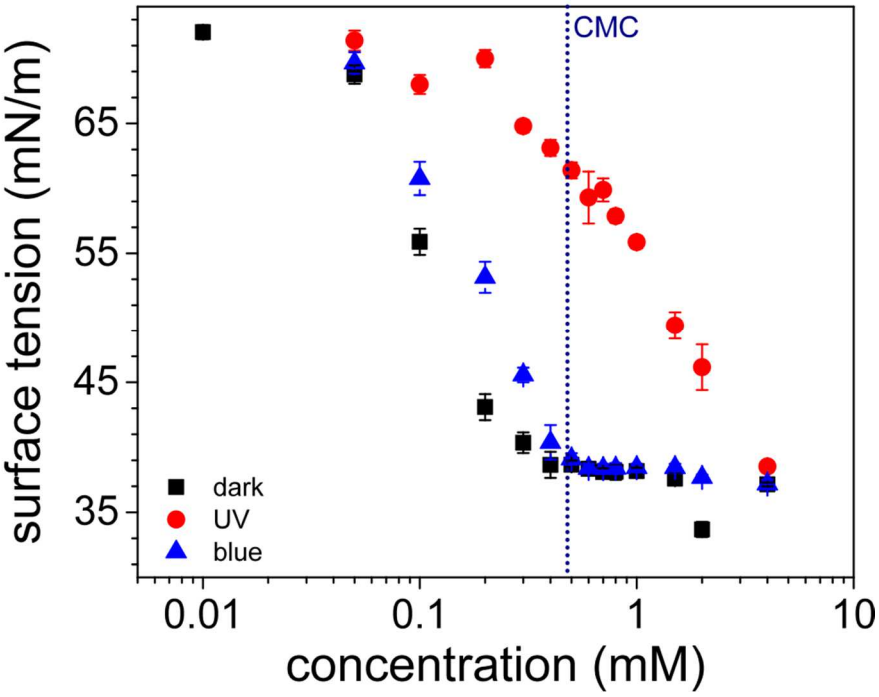

Figure 2.3. Surface tension as a function of the surfactant concentration measured by the pendant drop method. The CMC of dark solution (i.e. surfactant in the *trans* state) is marked by a dashed vertical line. The illumination wavelength was chosen to be UV (λ = 365nm) and blue (λ = 453nm).

2.2.5 Sample preparation

2.2.5.1 *Hydrophobic Substrates*

Teflon AF 1600 in solid form was dissolved in Fluorinert FC-77 by constant stirring for 3 to 4 hours to a concentration of 5w%. Microscope slides were cleaned in an ultrasound bath with acetone, 2% Hellmanex solution, and water (milliQ), each for 15 minutes, and dried with nitrogen before use. Hydrophobic samples were made with spin coating (model WS-650SZ-6NPP/LITE, Laurell Technologies Corp. USA) at spin rates of 2000 RPM for 30 seconds. Subsequently the substrates were heated up to 110°C, which is above the boiling point of the solvent FC-77.

The hydrophobicity was confirmed by contact angle measurements, which resulted in values between 110° and 120°. The surface thickness was measured between 50nm and 100nm.

2.2.5.2 *Patterned Surface*

A patterned surface was prepared by the following procedure. Liquid Polydimethylsiloxane (PDMS) was poured onto a patterned surface with different surface relief gratings (SRGs) and cured for 24h at RT. PDMS stamps were detached from the polymer films and deposited on glass slides. PDMS was prepared by mixing elastomer and a curing agent in a ratio of 10:1. The SRGs were made with a thin layer of photosensitive polymer irradiated with a UV interference pattern.[103]

2.2.5.3 *Janus Particles*

Silica particles were diluted to an appropriate concentration with milliQ water (i.e., 0.5 mg/ml for 5µm particles). Clean, hydrophilic microscopy slides (2cm x 2cm) were placed onto the spin coater. A droplet of 200 µl was pipetted onto the surface to cover the whole surface. After a spinning speed of 1500 RPM for 30s followed by 3000 RPM for 10s, the surface was free of solution, leaving only single particles distributed over the surface. In an evaporation chamber, metal was deposited onto the top of the substrate to a desired thickness. A lens cleaning tissue was cut into a small-sized piece and wetted with milliQ water. To collect the Janus particles, the tissue was gently moved over the surface. When the tissue is dropped into a vessel with milliQ water the Janus particles are released. After removal of the tissue, the dispersion was ready for usage.

2.2.6 Zeta potential

The zeta potential can be seen as the magnitude of electrostatic repulsion between particles dispersed in solution. Thus, it yields information about suspension stability. The larger the absolute zeta potential, the larger the particle repulsion and the more stable the suspension. When particles have a low zeta potential they coalesce for or aggregate and even precipitate.

When a particle is placed in a solution of a high dielectric constant (like water), the surface gets charged. For silica particles in water, the silanol groups dissociate, and the surface becomes negatively charged. Close to the surface, an EDL (**Figure 2.4**) is formed that is composed of two layers: the Stern layer, consisting of the inner and outer Helmholtz layer, and the diffuse layer. When an electrolyte is present, the ions with higher surface affinity align along the surface to form the inner Helmholtz layer. Typically, anions have a higher surface affinity because they are less hydrated.[104] This is often true even for negatively charged surfaces. At distances very close to the surface, the van der Waals attractive forces outperform electrostatic repulsion. The next layer, which is formed by counterions, is the outer Helmholtz layer. In this so-called Stern layer, the ions are considered to be fixed and immobile (different than liquid-liquid interfaces). The next layer, in which primarily cations can be found, is called the diffuse layer. At a certain distance from the surface, the particle is neutral because the ions in the electrostatic diffuse layer compensate the surface charge. When particles perform Brownian motion, the mobile diffuse layer can be sheared off due to diffusion. Some of the ions that lead to neutrality are lost, resulting in a nonzero net charge. Therefore, when an electric field is applied, the particles experience a force and start to move.

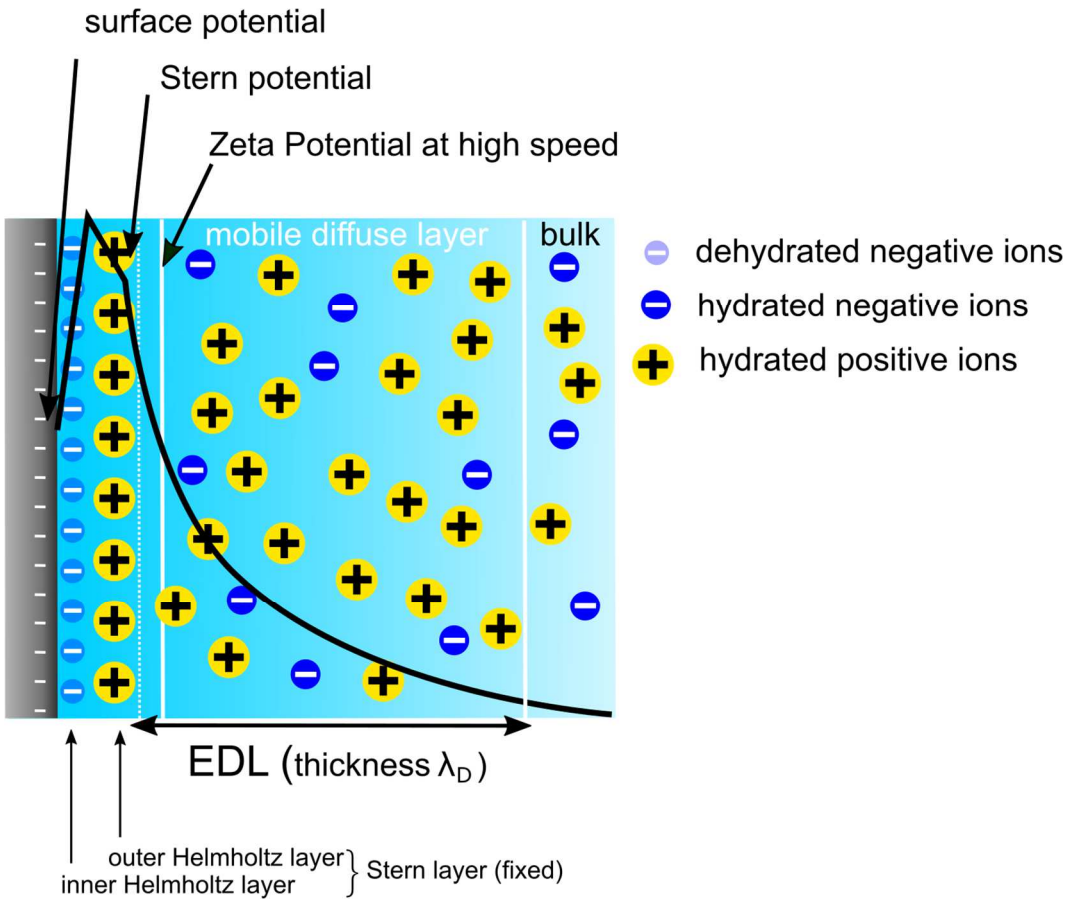

Figure 2.4. Scheme of the charged surface immersed in a solution with the characteristic layers: Stern layer, in which the ions are immobile, and the mobile diffuse layer of a thickness λ_D (Debye length). The negative surface potential drops exponentially in the diffuse layer. In the bulk layer, the concentration of positive and negative ions is equal, and the surface is neutral. At a certain speed of the particle, almost all ions are sheared off. This is where the zeta potential is measured, which is often assumed to be close to the Stern potential.

This phenomenon is called electrophoresis. With stronger electric fields, the speed can be increased. This shears off even more ions, and, thus, the net charge of the particle increases. When the particle speed is sufficiently large the diffuse layer is sheared off almost completely. At this shear plane the zeta potential is measured. It is often considered to be equal to the Stern layer potential. The thickness of the EDL is often given by the Debye length λ_D, which can be calculated from Debye-Hückel theory.[105] The length varies from around 900nm in bare water to just a few nanometers, increasing with the concentration of electrolyte in solution:

$$\lambda_D \sim \left(\sum_i z_i^2 c_i^\infty \right)^{-\frac{1}{2}}$$

with z_i the charge number and c_i^∞ the bulk concentration of the i-th ionic species.

In this work, the zeta potential of particles in water and azobenzene surfactant solution was measured by a Zetasizer Nano ZS (Malvern Instruments Ltd, UK) in disposable folded capillary cells (DTS1070) provided by Malvern. The measurement is based on the electrophoretic mobility of particles by dynamic light scattering. [††] From the electrophoretic mobility, the zeta potential is determined.

Measurements of the surface zeta potential (SZP) of the substrate provide information about the electrostatic interactions. With the SZP accessory (ZEN1020, Malvern Instruments Ltd, UK) for the Zetasizer series, the zeta potential of a flat surface can be measured.

The SZP of borosilicate substrates and Teflon (Teflon AF1600, DuPont) coated glass substrates was measured. Prior to the measurement, the samples were treated as follows: 1) A substrate was cut into pieces of roughly 4mm x (5 to 7) mm size, 2) glued onto a sample holder (provided by the Malvern), which was 3) screwed onto the accessory. 4) A suspension consisting of water, 300nm particles, and surfactant was prepared, and an amount of 1.2ml of the suspension was poured into a disposable plastic cuvette (1cm x 1cm, DTS0012). The accessory was placed in the cuvette and inserted into the measurement chamber of the Zetasizer. The substrate is located between two electrodes where a voltage is applied (**Figure 2.5**). Near the surface, an electroosmotic flow is created. Similarly, the tracer particles move by electrophoresis. Electroosmotic flow strength decreases with the distance to the surface. Taking both contributions into account, the surface zeta potential can be evaluated by measuring the mobility of the tracer particles as a function of the distance to the surface of the substrate. Far away from the surface, the particles only move by electrophoresis.[106]

[††] For detailed information about dynamic light scattering the reader is referred to text books i.e. from Berne and Pecora[167]

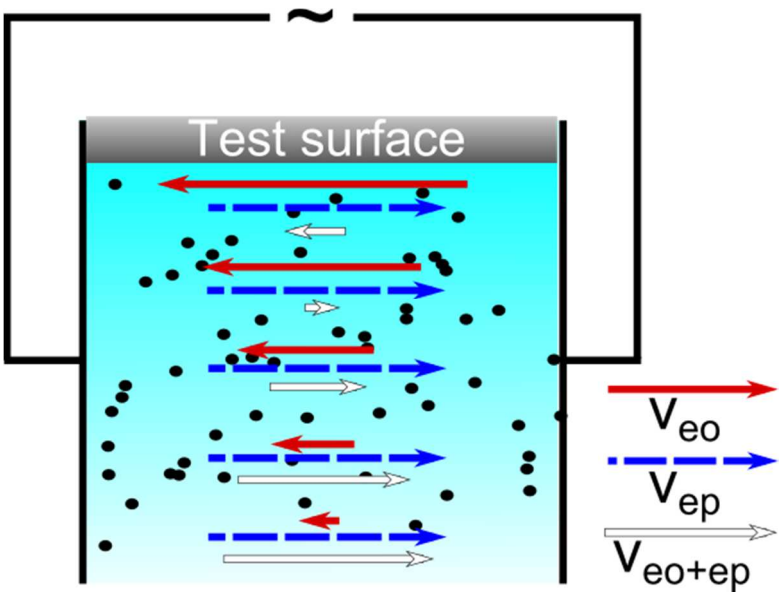

Figure 2.5. Schematics of flow fields near a test surface between two electrodes. An alternating voltage is applied (0.5Hz to 2Hz) The mobility of the tracer particles (white arrow) depends on the contributions of electroosmosis v_{eo} (red arrow) and electrophoresis v_{ep} (blue dashed arrow).

3 PARTICLE ACCUMULATION AND SEPARATION

This chapter demonstrates that photosensitive surfactants can induce LDDO flows near the solid-liquid interface. These flows can be used to manipulate particle ensembles trapped on the surface by focused irradiation. In a first section, it is reported on LDDO based on localized UV laser irradiation that leads to an outward motion of micrometer sized particles (i.e. away by the laser spot). An inward particle motion (i.e. towards the laser spot) under green laser irradiation is described in a second section. Third, findings are presented discussing the dependence of LDDO on the surfactant concentration and the CMC.

3.1 Particle separation in UV light

Figure 3.1a shows a scheme of the experimental setup: silica particles (2µm in diameter) dispersed in an aqueous solution of azobenzene containing surfactant (with a concentration of c = 1mM) are settled on a glass surface. The CMC of the surfactant is equal to 0.5mM. The irradiation direction is from below, the focal plane of the UV laser (λ = 355nm, P = 1.5µW) is at the level of the interface where the particles perform Brownian motion. Before irradiation, the silica particles form a densely packed monolayer at the glass surface. When illumination with UV light is turned on (the red cycle in **Figure 3.1b** indicates the center of the laser spot), the colloids are expelled from the illuminated spot leaving behind a completely clean area (60µm in diameter) after 5 minutes of irradiation. Along with the local irradiation, a spatially heterogeneous distribution of *trans* and *cis* isomers is created because under UV irradiation the surfactant molecules photoisomerize correspondingly. Without the presence of the surfactant, the particle assembly does not change, ruling out heating effects or gradients in the electromagnetic field as a possible driving mechanism.

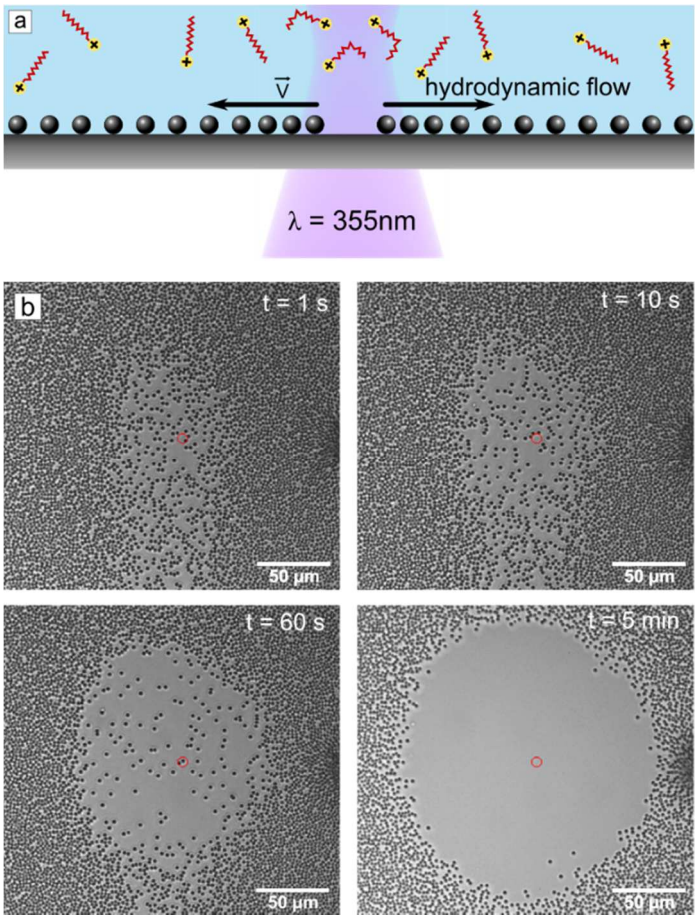

Figure 3.1. (a) A scheme demonstrates the characteristics of LDDO induced by UV light. The focused beam triggers local photoisomerization from *trans* to *cis* state. Particles on the surface are moved by a light-induced hydrodynamic flow. (b) Microscopic images of 2µm silica particles on a surface show motion away from the UV laser spot (red ring). Particles are dispersed in 1mM of azobenzene containing surfactant solution (AzoC6). The corresponding movie can be found in Appendix C1.

We tracked the trajectory of each individual particle and compiled corresponding statistics of particle distance and velocity. The particles were grouped in 30µm rings depending on their initial distance from the laser spot. For example, all particles from 0 to 30µm from the laser spot were considered to be in group 1. In group 2 were all particles located initially between 30µm and 60µm, and so on. All particles in one group were averaged to have a combined distance from the laser spot. On UV irradiation, the average distance increased, which was plotted in **Figure 3.2e**. Radial speed was calculated from the distance, taking time steps of 10s:

$$v_i = \frac{\Delta \overline{d}}{\Delta t} = \frac{\overline{d_{i+10}} - \overline{d_i}}{t_{i+10} - t_i} \tag{15}$$

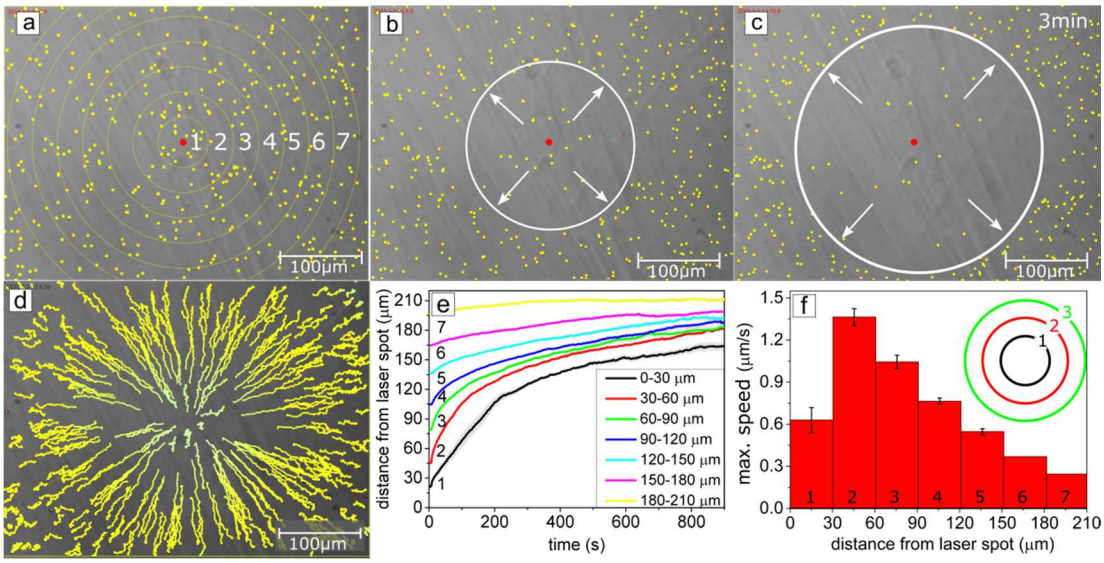

Figure 3.2. Micrographs of silica particles (marked in yellow) dispersed in solution of azobenzene surfactant under irradiation of focused UV light and corresponding analysis of tracked particles. (a) Particles distributed on the glass surface after sedimentation with 7 rings drawn around the laser spot in which particles were grouped and distances averaged for analysis. As irradiation started particles began to move radially outward; snapshots were taken at (b) 1min and (c) 3min. Corresponding movies can be found in Appendix C2. Particle trajectories are depicted in (d) after particle tracking. (e) For statistical analysis the particle distance from the laser spot was drawn as a function of time with corresponding maximal radial outward speed that differs for each group of particles. (f) The average maximum velocity of the particles as a function of the distance from the center of the laser spot.

The position of the particles enclosed in these rings was averaged and plotted as a function of time (**Figure 3.2e**). Particle motion differs depending on the initial position relative to the center of the laser spot. From these distance-time curves a maximal average velocity for each ring was calculated. A maximal average speed of 1.3µm/s was obtained for particles in the ring between 30µm and 60µm from the center of irradiation (**Figure 3.2f**). In more detail, the averaged radial particle speed away from the laser spot is shown in **Figure 3.3**. Particles located near the laser spot sped up rapidly when UV is switched on. They traveled away from the laser spot, the origin the flow, and their speed gradually decreased from a micrometer per second down to a few

hundreds of nanometers per second. Particles located farther away sped up later with lower maximum velocity. For example, in the ring 150µm away from the laser spot, particles sped up only to a maximal value of 250nm/s after several seconds, whereas particles in the first two rings suddenly jumped up to speeds of roughly 1.3µm/s. For all particles, the speed leveled off slowly the further they traveled away. A difference was found for very close particles, which experienced two maxima: the first directly after the laser was switched on and a second one after some minutes. Their maxima were less pronounced than the maxima for particles in the outer rings. After the second maximum, the velocity leveled off again to values below 0.2µm/s.

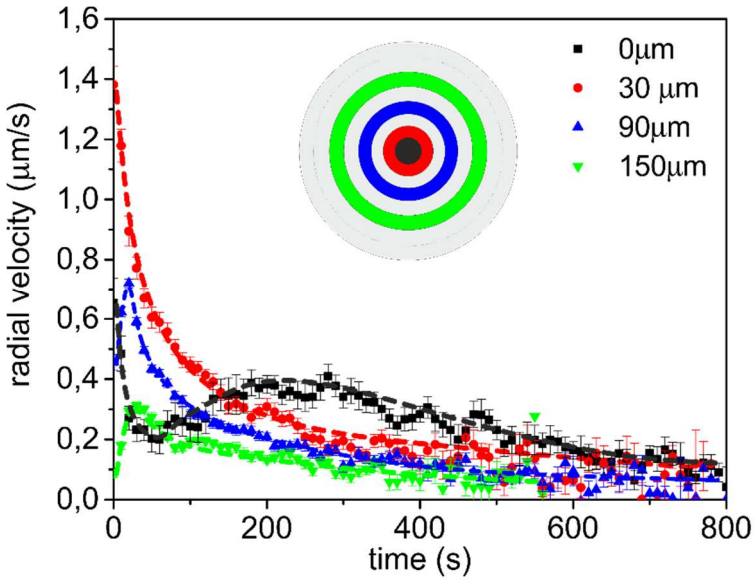

Figure 3.3. Particle velocity away from the laser spot as a function of time. Velocity was calculated from averaged distances of particles located before irradiation within distances of 0µm to 30µm (black), 30µm to 60µm (red), 90µm to 120µm (blue), and 150µm to 180µm (green). The rings depict the averaged distances. Velocities for other groups are omitted for clarity.

Since the UV laser was focused on the surface, the laser spot covered a certain effective volume in which the molecules were isomerized. Diffusion transferred *cis* molecules from inside the effective volume to the outside. When a Gaussian distribution of the *cis* concentration gradient was assumed after UV irradiation, diffusion broadened and lowered this distribution. In **Figure 3.4a** a scheme depicts the broadening of the concentration profile at successive time points. Under the assumption of a diffusioosmotic flow, the concentration gradient is directly related to flow speed (see **Chapter 4**). The concentration gradient decreased with time and with

distance. Therefore, particle speed decreased, which is shown schematically in **Figure 3.4b**. Particles very close to the laser spot were located inside the effective area of the laser, in which the speed was reduced due to a weaker concentration gradient. The largest concentration gradient was at the edge of the effective volume; thus, highest speeds were found at the edge of the irradiated area. Farther away from the laser spot, particle speed decreased again.

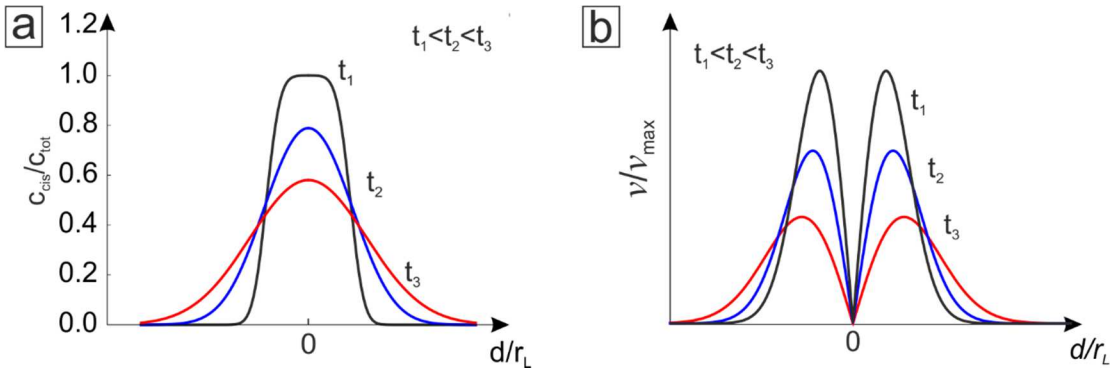

Figure 3.4. (a) Concentration distribution of normalized surfactant in *cis* state as a function of distance normalized by the size of the laser spot. Different times show the broadening of the profile under continuous irradiation. At time t_1 irradiation had just begun. (b) A corresponding velocity profile related to the distance from the spot.

In the previous analysis, the particles were grouped depending on their distance. An averaged distance of particles was used for analysis of their motion. To encounter particle motion from another viewpoint, the ring area was fixed and particle velocity was calculated for each ring as a function of time. That analysis reveals how flow strength changes with time at a certain distance. When looking at the average speed in a ring over time, the velocity of particles that pass that ring was measured, and it seems that the maximum speed was reached in the second ring. However, the velocity levels off in short time to lower speeds of only 0.3µm/s. In the outer rings, the initial speeds were lower, but, the speed remained higher for longer. In ring 4 (90µm to 120µm), an average speed of 0.6µm was reached and remained constant. It was the largest constant speed of all rings. This indicates the strongest flow was at this distance. This analysis method can yield artifacts. In the calculus, the velocity was averaged over all particles in that area. When a particle has left the area, particle velocity jumps and finally reaches zero when all particles have left. Information for the first ring is quite limited because particles left that area fastest.

3.2 Particle aggregation in green light

The direction of particle motion can be reversed by inverting the distributions of *cis* and *trans* isomers. This can be achieved by first bringing the majority of the surfactants in a *cis* state by global irradiation with UV light and then illuminating locally with green light to trigger the return to a *trans* state (**Figure 3.5a)**. In this case, during irradiation with light of $\lambda = 532$nm, the particles moved toward the center of the laser spot (**Figure 3.5b-d**). The gathering of colloids at the center of the laser spot continued during the whole irradiation period and resulted in the formation of a pile of particles (**Figure 3.5d**).

In principle, LDDO flow can be conducted as long as a sufficient amount of *cis* surfactant is present in the solution. In practice, an underlying volume flow often builds up over time, constantly driving the particle hill in one direction. For long periods, this can result in an elongated particle aggregate.

Larger particles, such as those 7μm in diameter, were driven similarly to the center of the laser spot. They then gathered at the laser spot creating a monolayer of particles. Because they are not as affected by thermal Brownian motion as 2μm particles, they formed a 2D crystal-like hexagonal monolayer **(Figure 3.6**).

With time, flow strength weakened. As a result, Brownian motion prevailed and the particle aggregate separated. This limitation could be overcome if the supply of *cis* isomers could be kept constant by simultaneous global illumination with UV light instead of red light.

With an increasing amount of gathered particles, the velocity distribution was naturally affected, but within the first stages of illumination (with only few particles accumulated), the trend of the particle velocity as a function of radial distance from the laser spot center was similar to that of the outward flow pattern (induced by UV irradiation). Particles situated somewhat away from the center (in our examples roughly 50 μm) had a maximal velocity of 1.2 μm/sec (**Figure 3.7**).

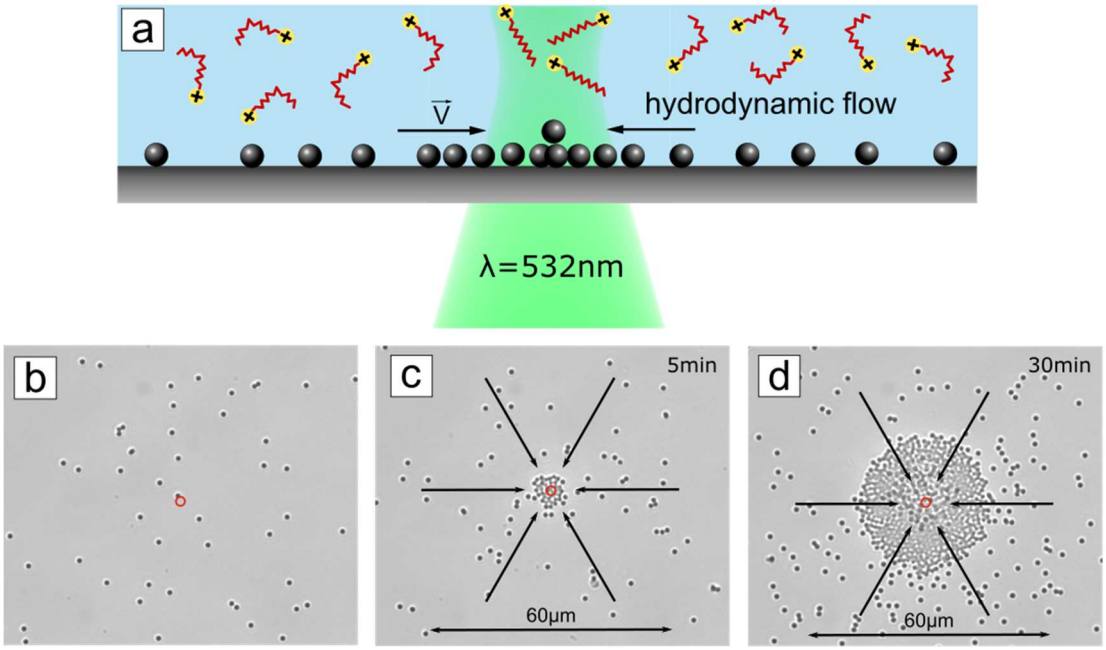

Figure 3.5. (a) Scheme of inward flow under green irradiation in *cis*-enriched surfactant solution gathering particles. (b) Optical micrograph of silica particles (d = 2µm) on a glass surface immersed into aqueous surfactant solution (c = 1mM), obtained after global illumination with UV light (10 min). A focused green laser (red circle) induced LDDO, driving particles radially inward to the laser spot; particles gathered at the center, after (c) 5 min and (d) 30 min of irradiation. The direction of particle motion is indicated by black arrows. The corresponding movie can be found in Appendix C3.

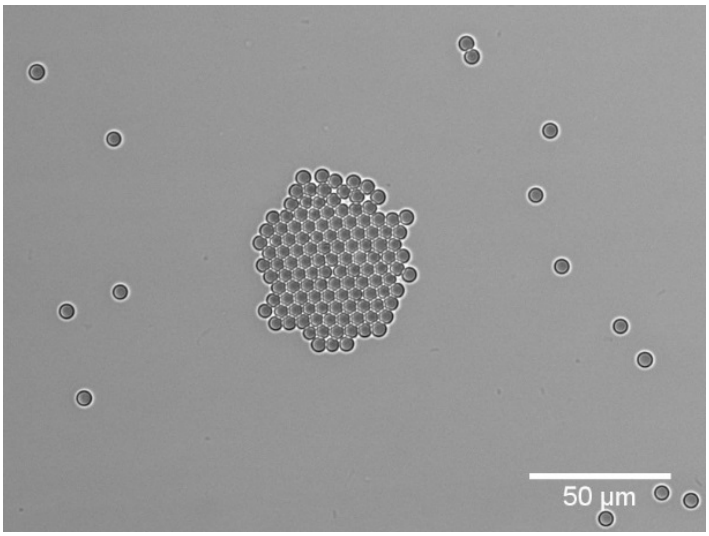

Figure 3.6. Micrograph of silica particles (7µm) forming a 2D crystal-like structure on a glass slide under irradiation with a focused green (λ = 532nm) laser. Particles were dispersed in a solution of 1mM azobenzene containing surfactant. A corresponding movie can be found in Appendix C4.

In **Figure 3.7a** the average particle distance from the laser spot is plotted as a function of time for different initial distances. Initially, the distance decreased until a specific distance was reached at which it increased again. The distance they could reach depended on the size of the particle aggregate, which increased as more and more particles approached the center. Averaged particle speed was calculated from the distances and plotted as a function of time (**Figure 3.7b**). In the first group around the laser spot, the maximal velocity was reached within the first seconds but dropped quickly when the particles reached the center of the laser spot. Particles initially located farther away from the laser spot reached their maximal speed later with lower speeds. Near the laser spot particle velocity rose quickly but also dropped quickly. Farther away, particles slowly increased speed and reached a maximum at around 75µm from the laser spot. Thereafter, speed decreased and even fell below zero, which means they were driven away from the laser spot. As particles reached the aggregate, they were first pushed inward and then outward again. This seemed to have happened for all groups of particles for unclear reasons that result in speculation: perhaps they drifted inside the aggregate but were then pushed away by inside particles and Brownian motion. However, the observation could also be an artifact resulting from particle tracking. Tracking particles inside the aggregate was difficult because they moved up and down and with other particles nearby. Therefore, particles were lost in the inside, and the average distance moved jumped to larger values.

When the maximal speed was plotted as a function of the initial distance from the laser spot (**Figure 3.7b** inset), a picture was drawn looking very similar to the results for outward motion under UV irradiation. A maximal speed was found in the second ring. Particles located farther away moved more slowly with distance. The maximal speed found in the second ring yields values of 1.2µm/s, similar to speeds reached for outward flows.

As UV irradiation has shown to trigger a radial outward flow when the surfactant solution is enriched of molecules in *trans* conformation, green irradiation has shown to trigger a radial inward flow accompanied by a particle gathering when surfactant solution was enriched of molecules in *cis* conformation. Speed analysis yielded similar results to outward motion for maximal velocities.

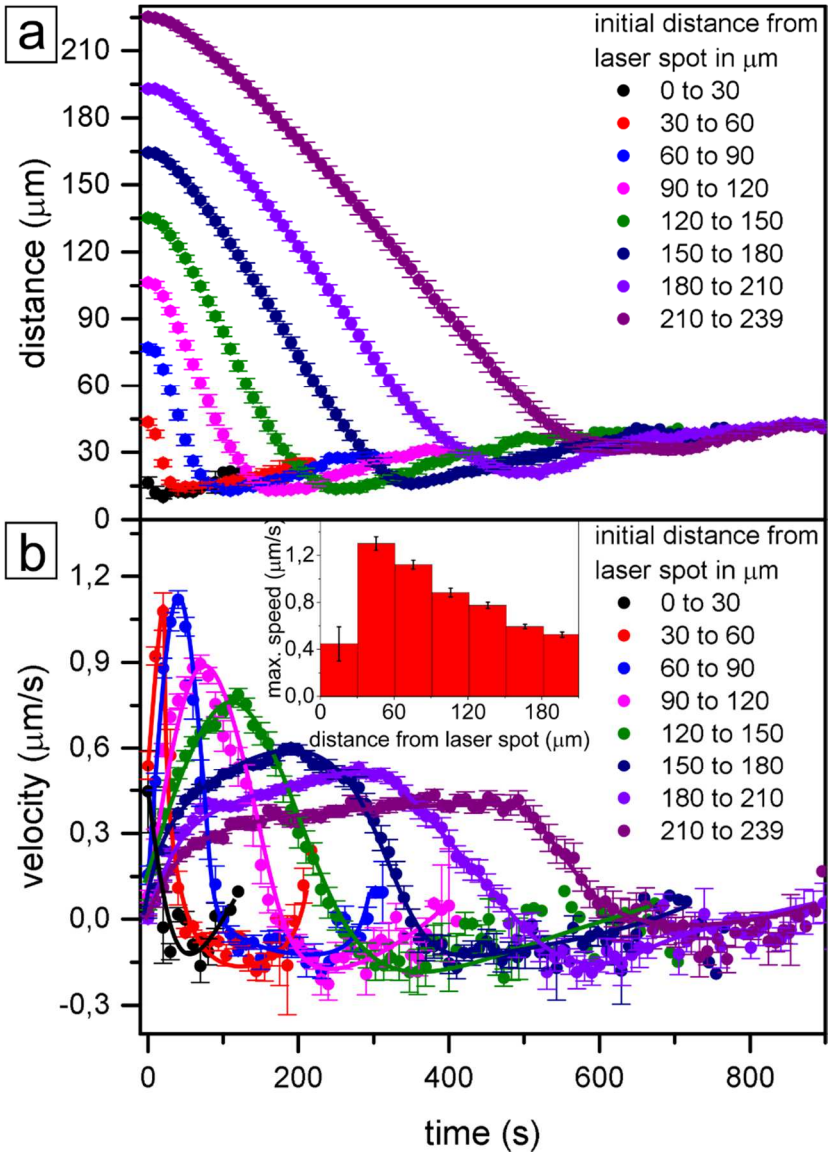

Figure 3.7. (a) Distance from the laser spot and (b) radial velocity as a function of time for 2μm particles dispersed in 1mM solution of AzoC6. Lines were drawn for better viewing. Inset: maximum velocity as a function of the initial distance from the laser spot.

3.3 Dependence of particle motion on surfactant concentration

Surfactant concentration largely affected the flow strength. In case of the absence of surfactant (i.e., in pure water), particles were unaffected by laser light. In this section, the flow strength was measured by maximal particle speed, which was plotted as a function of the surfactant concentration (AzoC6)(**Figure 3.8**). For all experiments the particle concentration was kept constant.

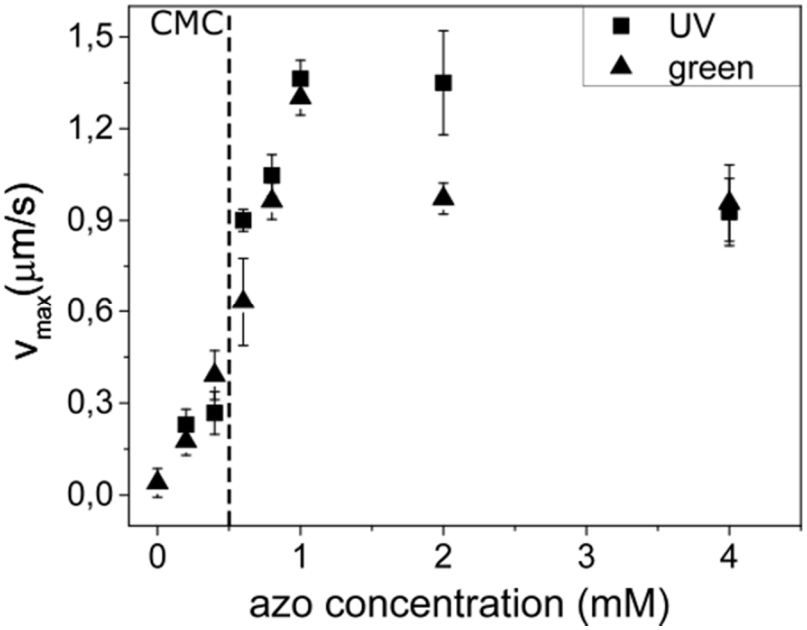

Figure 3.8. Maximal speed of silica particles of 2 µm in diameter as a function of surfactant concentration for two different irradiation wave lengths: UV (squares), and green light (triangles). The CMC of the surfactant concentration is designated by the dashed line.

For both irradiation wavelengths, a similar pattern was observed. Speed below the CMC of the surfactant remained low. When the concentration increased and overcame the CMC, the speed increased strongly with a maximum between 1mM and 2mM. A further increase of surfactant resulted in a slight reduction of particle speed found at 4mM of concentration. Similar behavior was found for green irradiation but with a faster decrease in speed—already at 2mM.

Clearly, the flow was affected by the surfactant concentration. Below the CMC, isomerization led to weak flows. Micellization seems to affect DO remarkably. Under UV irradiation, micelles are destroyed because the surfactant in a *cis* state has a larger CMC compared to surfactant molecules in the *trans* state. Upon irradiation, the concentration of *cis* monomers strongly increases with the decomposition of micelles. In reverse, green irradiation induces the formation of micelles, leading to a large reduction in the concentration of monomers in the vicinity of the laser beam. This dependence on the concentration gradient leads to a variation in flow strength. When a concentration gradient along a surface is imposed a diffusioosmotic flow can build up.

As shown, surfactant is required for flow generation. Temperature measurements near the laser spot ruled out thermal effects, such as convection or thermoosmosis or thermophoresis because the temperature remained constant under laser irradiation. In pure water, particles were unaffected by laser irradiation at powers as low as 1.5µW. Additionally, picric acid was dissolved in water and similar irradiation experiments were conducted. Picric acid has a similar extinction coefficient as AzoC6 but turns absorption into heat. At the laser power used in this work for irradiation experiments, inward or outward motion was absent in picric acid solution under irradiation. Furthermore, laser powers used in this work, the effect of radiation pressure is negligible. Even a manifold increase in laser power did not lead to particle motion. Only an increase of three to four orders of magnitude with laser powers in the range of 10mW to 100mW could induce particle motion. Motion at a higher laser power with or without surfactant can be induced by heating or by radiation pressure, with the latter being intentionally used in optical tweezers or traps.[107, 108]

3.4 Summary

Photosensitive azobenzene containing surfactant induced the collective motion of microparticles. Silica particles located at a solid-liquid interface dispersed in a surfactant solution were collectively moved under the irradiation of a focused laser. UV irradiation drove silica particles away from its point of irradiation. Therefore, a continuous flow led to a cleaning of the surface. Under green irradiation, particle motion was directed inward when the solution was transferred into a *cis*-dominated solution by global UV illumination beforehand. In this way, particles were gathered around the green laser spot, causing a pile of particles to accumulate. An analysis of particle motion revealed a dependence of particle speed on the initial distance from the laser spot. Particles with an increased initial distance moved with slower maximal speeds; however, particles very close to the laser spot moved slower. The lower particle speed near the laser spot might be caused by the width of the *cis* distribution imposed by the laser. When particle speed is related to the concentration gradient, the gradient is minimal at the center of irradiation. Therefore, particles very close to the center of the laser spot moved slower. Maximal particle speeds of ~1.3µm/s were found for surfactant concentrations of 1mM for laser power of 1.5µW for UV light and 30µW

for the green laser. A decrease in surfactant concentration led to a decrease in particle speed. Particle motion was absent below 0.2mM. An increase above 1mM showed a slight decrease in maximal speeds. In the following chapter, a theoretical consideration based on diffusioosmosis is given.

4 LIGHT-DRIVEN DIFFUSIOOSMOSIS: MODEL AND THEORY

In the previous chapter, it was shown that focused UV light can induce particle motion near a surface when an appropriate amount of surfactant is dissolved in solution. Based on those results a theoretical model was proposed of diffusioosmotic flows based on the photoisomerization of light-sensitive surfactants. This theory was developed in collaboration with Salim Maduar and Olga Vinogradova from Moscow State University, Russia. This chapter presents a simple model of LDDO, from which a basic understanding of the physical origin of LDDO can be derived.[109]

Essentially, DO can have a chemiosmotic and electroosmotic contribution. In the case of nonionic solute, DO is driven by chemiosmosis—i.e., a concentration gradient of solute molecules in the electric diffuse layer. In the case of ionic solute, an electroosmotic part contributes to the flow. In this theory, the electroosmotic contribution to DO can be omitted because the total concentration remains constant under irradiation $c_{tot} = c_{trans} + c_{cis} = const.$

One of the interactions that drives adsorption of surfactant to the surface is of an ionic nature. The total interaction can be described by means of an electrostatic potential $\phi(y)$, which depends on the distance *y* normal to the surface. In addition to electrostatic interaction, hydrophobic interactions also contribute to the potential that determines the surfactant adsorption. The interaction between solute and surface leads to EDL formation. The surfactant concentration in the EDL follows a Boltzmann distribution:

$$c(y) = c_{\infty} e^{-\frac{\phi(y)}{k_B T}}, \tag{16}$$

with c_{∞} the bulk concentration, k_B the Boltzmann constant, and T the temperature.

The approximate thickness of the EDL is given by the Debye length, which can be estimated from linearized Poisson-Boltzmann (Debye-Hückel theory) for an

electrostatic potential of $|\phi| \leq 25\text{mV}$, depending on the ion concentration:

$$\lambda_D = \sqrt{\frac{\epsilon_r \epsilon_0 k_B T}{\sum_i^N e_i^2 n_i^0}} \sim n_0^{-\frac{1}{2}} \approx 10\text{nm}, \tag{17}$$

with $\epsilon = 80$ for water, $n_i^0 = 1\text{mM}$ (for both ions), T the temperature, k_B the Boltzmann factor, and e the elementary charge.

The structure and size of the EDL depends primarily on the adsorbed ions. A negatively charged surface attracts positively charged surfactant ions. Including the other attractive interactions, this yields a larger concentration inside the EDL, which also depends on the isomeric type. Therefore, the surfactant concentration in the EDL exceeds the bulk concentration; surfactant adsorption to the surface is given by the surface excess, Γ, with units in g/cm^2 or in mol/cm^2.

Focused UV irradiation leads to a local *trans*-to-*cis* isomerization. Due to laser focusing and a very fast (picoseconds) switching of azobenzene, a sharp gradient appears, dividing the fluid into spaces of either exclusively *cis* isomers or *trans* isomers. A difference in chemical potentials for surfactant in a *trans* and *cis* state results in a difference of osmotic pressure at the surface for *cis* and *trans*-dominated fluid volume:

$$p(x,y) - p_\infty = k_B T[c_+(x,y) + c_-(x,y) - 2c_0(x)], \tag{18}$$

with p_∞ the osmotic pressure due to solute in bulk solution with vanishing potential, $\phi(x, y \gg \lambda_D) = 0$, $c_0(x)$ the bulk surfactant concentration, and $c_\pm(x,y)$ the local ion concentration within the EDL. As the concentration increases locally, the osmotic pressure gradient normal to the surface is translated into a component along the surface. This pressure difference is compensated by a hydrodynamic flow—a diffusioosmotic flow. The flow field v satisfies Stokes' equations:

$$\eta \nabla^2 v = \nabla p, \nabla \cdot v = 0, \tag{19}$$

where η is the fluid viscosity. The diffusioosmotic slip velocity along the surface (*x*-direction) at the edge of the EDL, v_{DO}, can be obtained when **Equation (19)** is solved within the EDL:

$$v_{DO} \propto -\frac{k_B T}{\eta}\frac{\mathrm{d}(\Gamma_{EDL}\lambda_D)}{\mathrm{dx}}, \tag{20}$$

with the surface excess of ions:

$$\Gamma_{EDL} = \int_0^\infty [c_+(x,y) + c_-(x,y) - 2c_0(x)]\mathrm{d}y, \tag{21}$$

which is similar to the equations derived above for diffusioosmotic flow (see **Equation (12)** and **Equation (13)**). To account for the nonuniform concentration of *trans* and *cis* species, the equations are modified. A local isomerization only alters a fraction of *trans* to *cis* concentrations, but, in total, the monomer concentration remains constant. To express **Equation (20)** in terms of concentration gradients for *trans* and *cis* surfactant, the gradient $\frac{\mathrm{d}\Gamma_{EDL}\lambda_D}{\mathrm{d}x}$ is exchanged:

$$v_{DO} \propto -\frac{k_B T}{\eta}\left(\frac{\partial(\Gamma_{EDL}\lambda_D)}{\partial c_t}\nabla c_t + \frac{\partial(\Gamma_{EDL}\lambda_D)}{\partial c_c}\nabla c_c(x)\right), \tag{22}$$

with c_t and c_c for *trans* and *cis* concentrations, respectively. The terms $\frac{\partial(\Gamma_{EDL}\lambda_D)}{\partial c_{t/c}}$ represent adsorption isotherms of surfactant in a *trans* and *cis* state to the solid surface inside the EDL. These terms are accessible experimentally by measurements of adsorption isotherms and zeta potential.

From **Equation (21)** one can see that the surface excess Γ_{EDL} depends on the concentration of ions inside the EDL, which is related to the interaction potential by Boltzmann's distribution—see **Equation (16)**. Combining this dependence with Grahame's equation[‡‡] and under the assumption of a surface potential less than 100mV, this leads to the following expression for surface excess in the EDL:[110, 111]

$$\Gamma_{EDL}(x) \sim (c_+(0) + c_-(0) - 2c_0)\lambda_D \sim c_0\lambda_D\left(\frac{e\phi_0}{k_B T}\right)^2 \tag{23}$$

Together with **Equation (22)**, this shows that the flow depends on the total concentration and on the varying adsorption strength of *trans* and *cis* isomers with

[‡‡] Grahame equation relates surface charge density and surface potential to a concentration difference, which in turn relates to the EDL.

variation of the zeta potential that relates to ϕ_0.[104]

Above, we have considered the inner flow velocity—i.e., the flow within the EDL. With the result of the slip velocity found from **Equation (22)**, the outer velocity flow profile (i.e., the flow profile outside the EDL) is calculated. The outer flow can be visualized by its streamlines, which can be calculated by applying the curl vector operator ($\nabla \times$) to **Equation (19)**:

$$\nabla^2(\nabla \times v) = 0 \tag{24}$$

with stream functions that satisfy the continuity equations:

$$v_x = \partial_y \psi(\mathrm{x,y}) \text{ and } v_y = \partial_x \psi(x,y) \tag{25}$$

To calculate the velocity profile, two boundary conditions are applied. The first one takes into account that the outer velocity at the surface is equal to the inner velocity at the edge of the EDL:

$$\partial_y \psi(\mathrm{x},0) = v_{DO}(x) \tag{26}$$

The second boundary condition takes into account that the solid surface is impenetrable by the fluid:

$$\partial_x \psi(\mathrm{x},0) = 0 \tag{27}$$

Under these assumptions **Equation (24)** can be rewritten as a biharmonic equation for a stream function $\psi(x,y)$:

$$\frac{\partial^4 \psi(\mathrm{x,y})}{\partial x^4} + \frac{2\partial^4 \psi(x,y)}{\partial x\, 2\, \partial y^2} + \frac{\partial^4 \psi(x,y)}{\partial y^4} = 0 \tag{28}$$

General solutions of the biharmonic equation have been used to calculate flow profiles numerically.[112] The diffusioosmotic slip velocity v_{DO} was deduced from the velocity values of the experimental data from outward particle motion under UV irradiation. In **Figure 4.1** a scheme of LDDO with streamlines is presented. It is important to note that the dimensions of the stream lines are in the micrometer range, whereas the dimension of the flow is in the nanometer range.

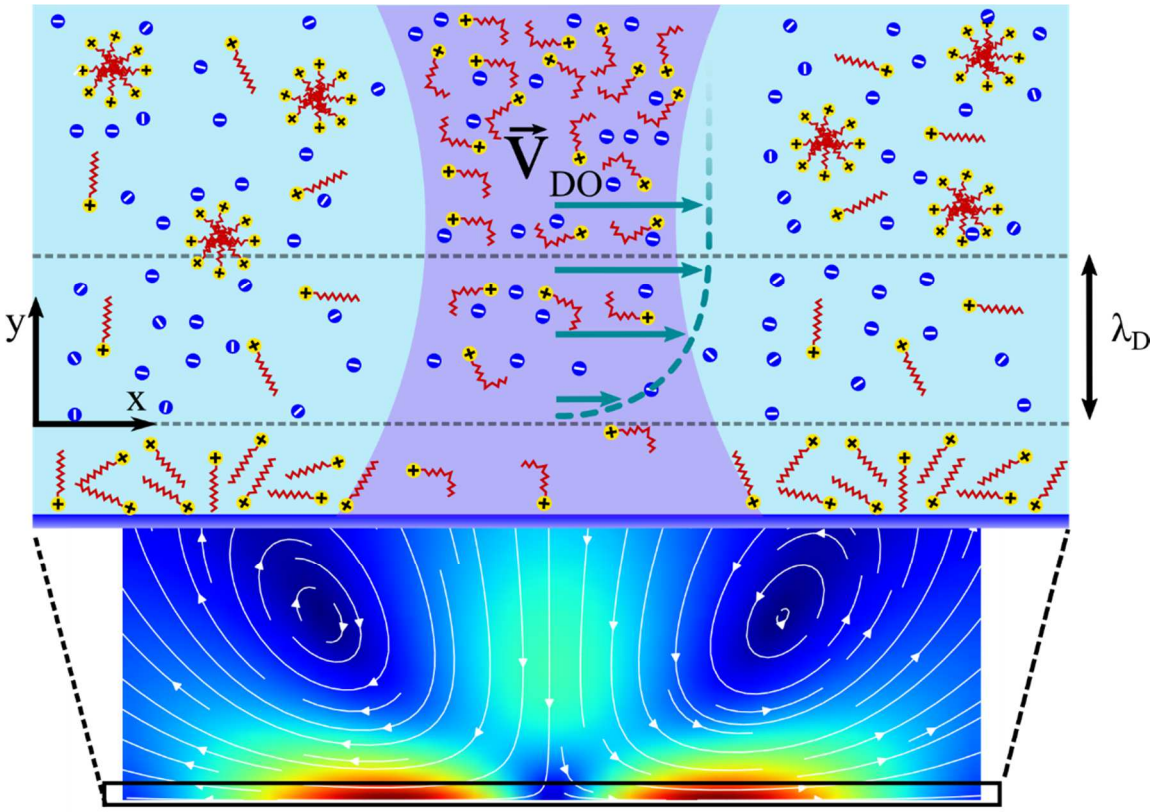

Figure 4.1: Schematic representation of light-driven generation of local diffusioosmotic flow. Schematic streamlines of liquid flow are presented at the bottom. Color represents regions with different absolute values of the liquid velocity, being at maximum in red. The thickness of the EDL is given as λ_D.

In the following sections, two different situations are discussed: below and above the CMC. If the surfactant concentration is below the CMC, irradiation leads to a change of the fraction of *trans* to *cis* isomers. For example, under UV irradiation ~90% of the surfactant molecules are found in *cis* state. When *trans* is converted to *cis,* or vice versa, the concentration of *cis* surfactant can be expressed as $c_c = c_0 - c_t$. Therefore, **Equation (22)** can be written as follows:

$$v_{DO} \propto \frac{k_B T}{\eta}\left(\frac{\partial(\Gamma_{EDL}\lambda_D)}{\partial c_t} - \frac{\partial(\Gamma_{EDL}\lambda_D)}{\partial c_c}\right)\nabla c_c(x), \qquad (29)$$

which shows that the velocity depends on the relative adsorption of *cis* and *trans* isomers.

If the surfactant concentration exceeds the CMC, addition of surfactant in the *trans* state leads to the formation in micelles—for surfactant in the bulk—and surface

aggregates[§§] with a monomer concentration that remains constant $c_{t,mono} = c_{CMC} = const$. Therefore, the *cis* concentration cannot be expressed by $c_c = c_0 - c_t$. If we assume a constant monomer concentration of monomeric *trans* surfactant, the gradient yields $\nabla c_t \approx 0$, and only the gradient in the *cis* concentration becomes important:

$$\nu_{DO} \propto \frac{k_B T}{\eta} \left(\frac{\partial(\Gamma_{EDL} \lambda_D)}{\partial c_c} \right) \nabla c_c(x). \tag{30}$$

With these derivations and a scaling analysis, we can estimate the diffusioosmotic velocity for surfactant concentrations above the CMC as follows:

$$\nu_{DO} \propto \frac{\lambda_D}{\eta} \cdot \frac{k_B T \Gamma_{EDL}}{L} = \frac{\lambda_D^2}{\eta} \cdot \frac{RT c_0}{L} \cdot \left(\frac{e\phi_0}{k_B T} \right)^2 \tag{31}$$

in which L is the diameter of the laser spot. Considering reasonable estimations for the parameters L = 60µm, $\lambda_D = 10\text{nm}$ at $c_0 = 1\text{mM}$, $\eta = 1\text{mPa·s}$, and T = 20°C and for the surface potential $\phi_0 = 70\text{mV}$ (taken from SZP measurements for $c_0 = 1\text{mM}$) an diffusioosmotic velocity yields values of $\nu_{DO} \approx 7\mu\text{m/s}$. This estimation is in line with the experimental results for the maximal speed, which was around 1.5µm/s. Diffusioosmotic flows are generally much slower than light-driven Marangoni flows based on azobenzene surfactant, which can be in the order 500µm/s to mm/s.[60, 61, 113]

In **Figure 4.1**, a scheme summarizes the important points of the model. A photosensitive cationic surfactant interacts with a solid surface mainly by electrostatic and hydrophobic interaction. This interaction can be described by an attractive potential between surface and surfactant. Mutual interaction between surfactant molecules leads to the formation of aggregates on the surface and in the bulk. This formation depends on the bulk concentration and, crucially, on the isomer state. The concentration of surfactant inside the EDL follows a Boltzmann distribution and is given by the surface excess, which depends on the surfactant adsorption strength and total concentration.

[§§] Surface aggregates appear even below the CMC due to attractive interaction between surface and surfactant as well as a loss in entropy when surfactant molecules are removed from water.

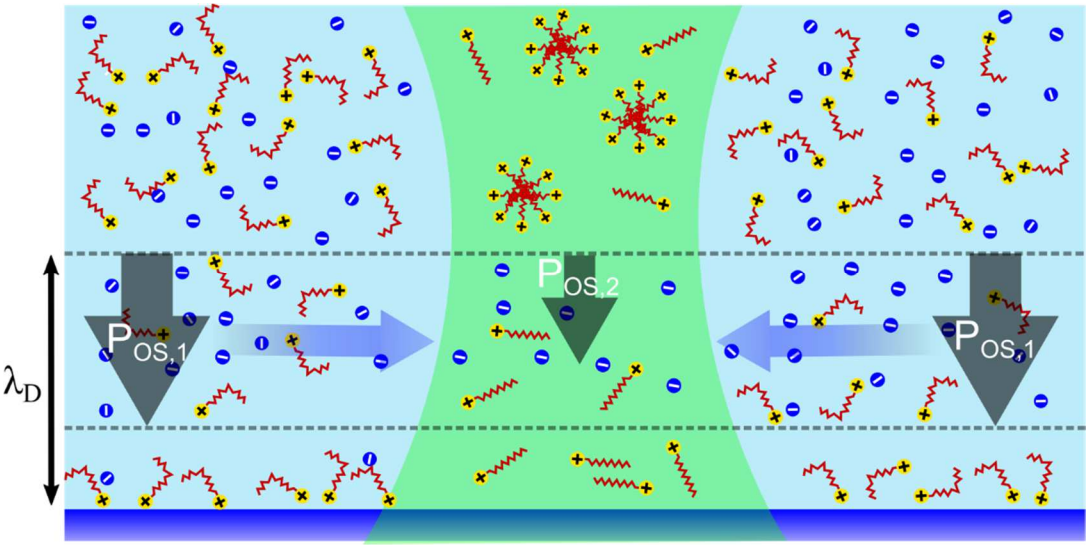

Figure 4.2. Scheme of LDDO under green irradiation. A local *cis*-to-*trans* isomerization lowers the concentration in the irradiated area due to micellization. A difference in osmotic pressure in the irradiated area creates an inward hydrodynamic flow.

When UV light is focused onto a solid-liquid interface, a *trans*-to-*cis* isomerization leads to a local gradient of isomer concentration and, therefore, to an osmotic pressure difference along the surface. Depending on the relative interaction between surfactant in a *trans* or *cis* state with a surface, which determines the surface excess in the EDL, an inward or outward diffusioosmotic flow is created in the EDL. Below the CMC, *trans* and *cis* adsorption has to be taken into account. Above the CMC, only *cis* adsorption is taken into account because UV irradiation mainly leads to a decomposition of micelles and to an increase in the surfactant's concentration of monomers in a *cis* state. In that case, the diffusioosmotic flow is mainly driven by a *cis* concentration gradient.

In the presence of green light, the situation is reversed and *cis* is converted into *trans*. Similarly, an osmotic pressure difference at the interface between irradiated and nonirradiated creates a diffusioosmotic flow that directs inward (**Figure 4.2**). Indeed, when green light converts *cis* to *trans,* suddenly there is a drastic decrease in the concentration of *cis isomer*s near the irradiated area. Nearby, the *cis* isomers are still attracted to the surface. This generates an osmotic pressure gradient pointing toward the laser beam. Above the CMC, green irradiation leads to the formation of *trans*

isomers and micellization, which results in a decrease in concentration of *cis* surfactant in this region and a larger gradient—and thus, a stronger flow and particle speed.

Flow strength and direction of motion depend on the concentration gradient in the EDL and, thus, on the surface excess of surfactant molecules. Surface excess in the EDL depends on the surface potential and surface properties. Adsorption of surfactant is analyzed in the following chapter.

In LDDO a local isomerization by light induces a concentration gradient and, thus, a diffusioosmotic flow. The isomerization properties of azobenzene introduce light-sensitivity into surfactants. Because surfactants are active at surfaces, they bring this light-sensitivity into interacting systems, such as the boundary between solids and liquids. Due to the interaction between the liquid molecules and solid atoms, the interfacial layer acts as a place where surface flows can be created, such as DO. A combination of light-sensitive surfactants dissolved in water and a solid interface can induce a surface flow driven by light.

5 DEPENDENCE OF LIGHT-DRIVEN DIFFUSIOOSMOSIS ON IONIC STRENGTH, PARTICLE SIZE AND SHAPE, SURFACTANT HYDROPHOBOCITY, AND ILLUMINATION PARAMETERS

In the previous chapter, the concept of LDDO was introduced to explain the observed motion of particles under local UV and green laser irradiation in the presence of azobenzene containing surfactant.

This chapter presents a discussion regarding how LDDO depends on different parameters, such as ionic strength, particle size and shape, surfactant nature, and irradiation conditions.

This chapter is structured in five sections in which the following parameters are investigated: ionic strength, which influences the Debye length and the CMC; particle size and shape, which indicate whether a diffusiophoretic part is involved; surfactant hydrophobicity, which provides knowledge about the influence of the CMC; illumination conditions, which shift the photostationary state into different fractions of *cis* to *trans* isomers; and laser focus, which affects the local isomerization.

5.1 Ionic strength

According to theoretical considerations, a change in the Debye length must alter the LDDO flow. To check this, we chose the electrolyte NaBr to vary the ionic strength because Br^- also represents the native counterions of the cationic surfactant. As shown in **Figure 5.1**, the particle speed decreases with an increasing NaBr concentration. At a concentration of 2mM NaBr, the flow shows a slow cleaning effect, which becomes visible after more than 15 min of UV irradiation.

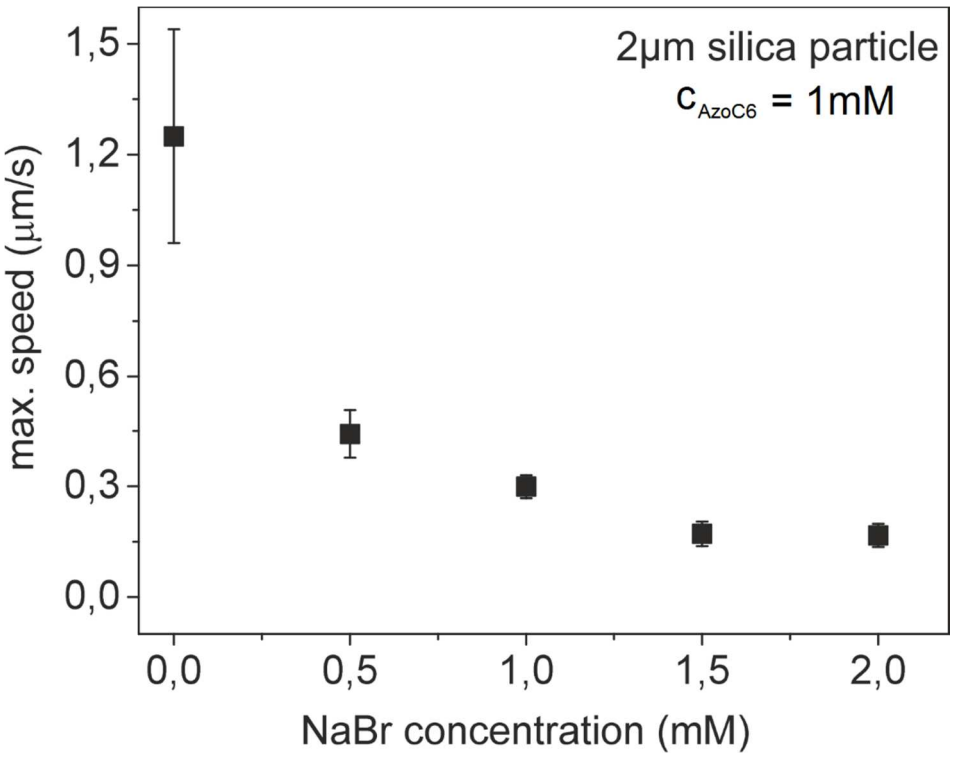

Figure 5.1. Maximal averaged particle (d = 2µm) speed as a function of NaBr concentration under UV irradiation in a solution of AzoC6 (c_{Azo} = 1mM).

An increase in the ionic strength alters three important parameters: (1) the Debye length, (2) the CMC, and (3) the amount of surfactant adsorbed to the surface. When electrolyte is added to surfactant solution, it shields the head-to-head repulsion of neighboring surfactant. Additionally, the CMC shifts to lower concentrations.[37] Since surfactant-surfactant interaction plays an important role in adsorption to the surface, electrolyte enhances adsorption below the CMC.[34, 114] Some have reported on the adsorption of cationic surfactant to silica, on which the surfactant molecules form spherical aggregates as AFM imaging reveals—even a change from spherical to cylindrical is possible.[114] As the CMC is shifted to lower concentrations when electrolyte is added, the flow response should similarly shift to lower concentrations if LDDO only depends on the CMC and micelle decomposition. As this is not the case, the following paragraphs explain why the addition of electrolyte suppresses LDDO.

At concentrations of 5mM, the Debye length is around 4nm. In comparison, without added salt at c_{Azo} = 1mM, λ_D = 10nm (see **Equation** (**17**)). As one can see from **Equation** (**20**) (**Chapter 4**), the term $\frac{d(\Gamma_{EDL}\lambda_D)}{dx}$ involves a change in the Debye length.

An irradiation involves a change in surfactant adsorption and, thus, a change in Debye length. An addition of salt screens the surface and fixes the Debye length to a few nanometers. Therefore, the gradient between irradiated and nonirradiated areas is reduced, and LDDO flow decreases.

5.2 Particle size and shape

This section investigates how particle velocity depends on the size and shape of particles. Throughout this section, the surfactant concentration was 1mM and the irradiation was performed with UV light. **Figure 5.2** shows that the particle speed remains constant when particles have diameters ranging from 1µm to 10µm. Small velocity decreases were observed with increasing particle size. This decrease could be a result of the decreasing flow speed with the distance from the surface and, therefore, an influence of Stokes friction, as shown in **Figure 5.3**.

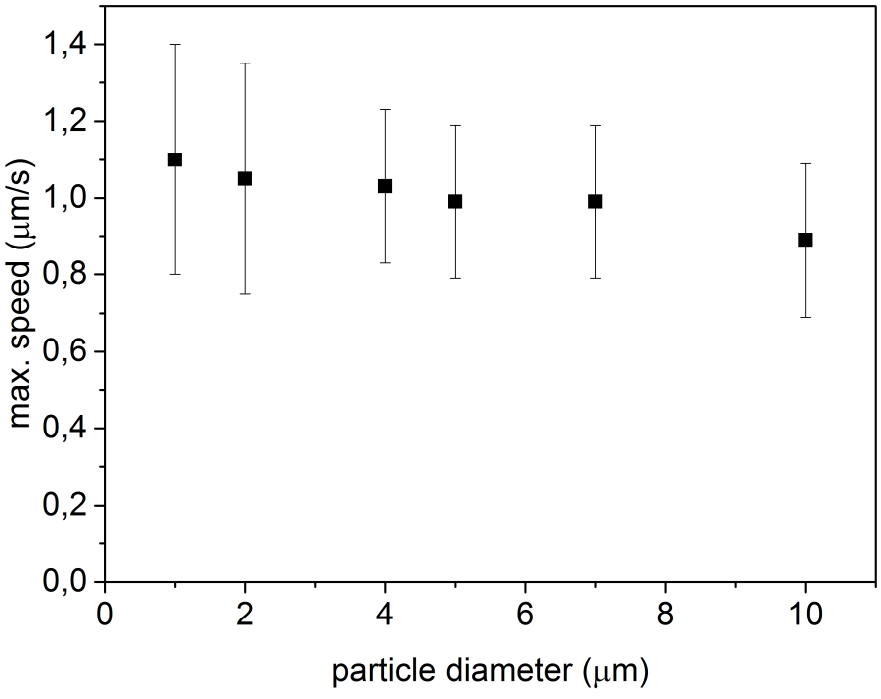

Figure 5.2. Maximal speed of spherical particles of different diameters in 1mM AzoC6 solution under UV irradiation.

For the investigation of asymmetric objects, cylindrical microrods were dispersed in 1mM solution of azobenzene containing surfactant. They varied in length from 10µm to 30µm and had a diameter of 3µm (Nippon Electric Glass Co., Japan). Similar to the motion of spherical particles, the microrods moved with the flow, either radially outward under UV or inward under green laser light irradiation with comparable maximal speeds of around one micrometer per second. While gathering (i.e., under green irradiation) due to its rod-like shape, the collective inward motion the impression that the rods are alive and gather like bacteria to an attracting chemical (chemotaxis). Static images of LDDO-induced gathering of microrods under green irradiation are shown in **Figure 5.4**.

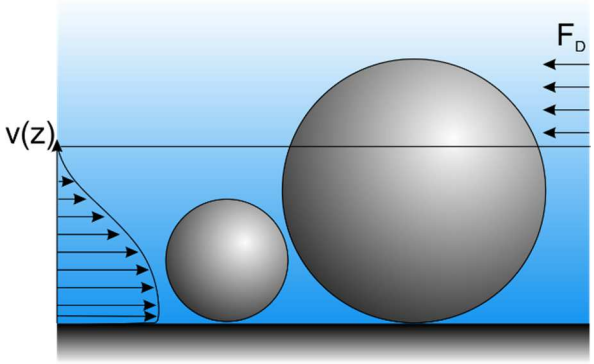

Figure 5.3. Scheme of how particle size affects flow speed

When the laser point is moved along the surface, the gathering point is changed, which results in guidance of the microrod aggregate, as shown in Appendix C5. In the video, the top illumination was occasionally set to UV to increase the amount of *cis* molecules which improved particle speed. [***]

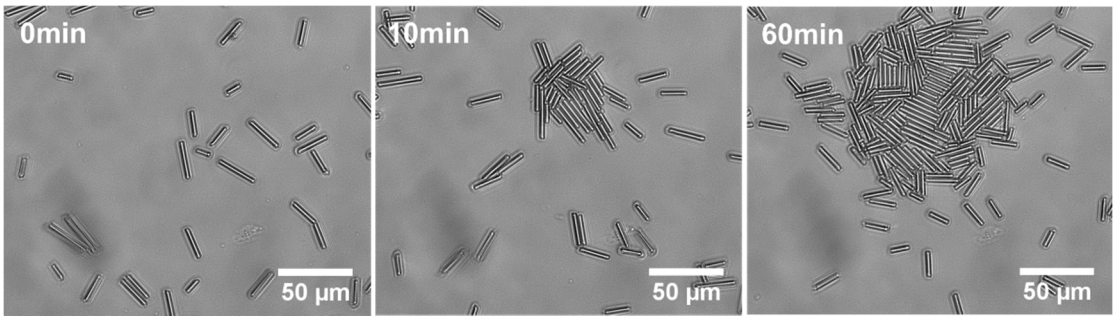

Figure 5.4. The micrographs show the gathering of microrods by LDDO (c_{Azo} = 1mM). They are directly attracted to the green laser spot (λ = 532nm). The suspension was globally illuminated with UV light before the droplet was deposited onto the glass slide to create a *cis*-enriched solution.

[***] At these points the green laser spot is directly visible. UV light is much less intense, therefore, the camera exposure time was increased; the green laser spot is shown much brighter due to increased sensitivity of the microscope camera

The green laser spot was placed near the end of a single microrod. When the laser spot was moved slowly around in a circle, only the near end was attracted by the laser spot. The rod turned around like a pointer of a ticking clock.

5.3 Variation of surfactant hydrophobicity

In this section, the influence of surfactant hydrophobicity on LDDO flows is analyzed (**Figure 5.5**). The hydrophobic part of a surfactant strongly affects cooperative properties, such as micellization and interaction with an interface. Hydrophobicity can be increased in several ways, making the head less hydrophilic or increasing the hydrophobicity of the tail. The latter can be done by adding more CH_2 groups to the tail. The longer the alkyl tail, the more hydrophobic the surfactant. By increasing the hydrophobicity, the CMC decreases because the gain in entropy on micellization is larger for more hydrophobic surfactants.[115-117] In **Section 3.3** it was shown that LDDO depends strongly on the surfactant concentration with a peak velocity just above the CMC.

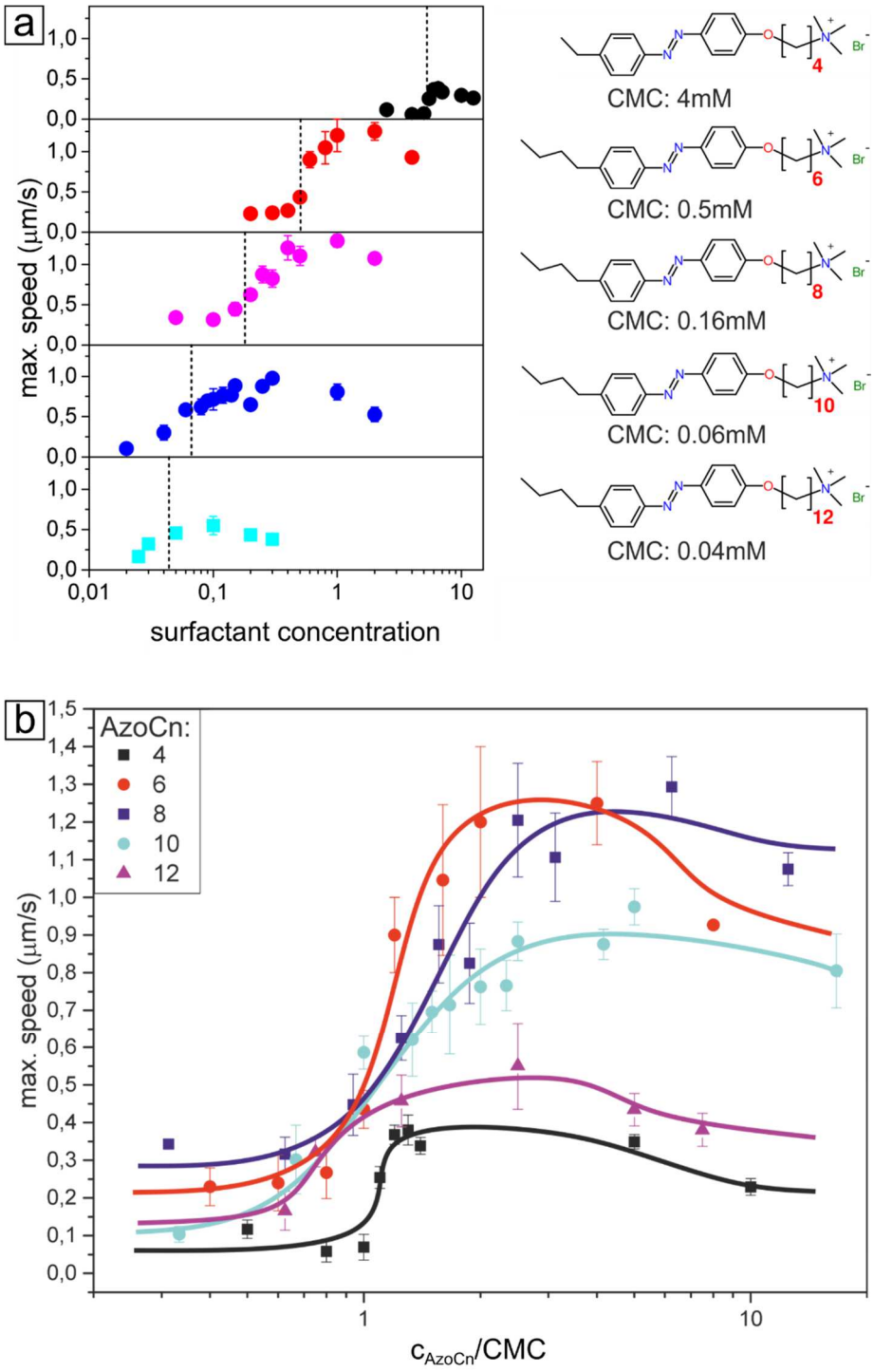

Figure 5.5. Maximal particle speed for different surfactants as a function of (a) surfactant concentration, including surfactant structure on the right hand side and (b) normalized surfactant concentration. Hydrophobicity increases with tail length and lowers the CMC. Names are given as AzoCn, in which n corresponds to the number of CH_2 groups in the spacer of the surfactant tail. Note that AzoC4 has two fewer CH_2 groups in the tail.

Surfactants were synthesized similarly to AzoC6, but the alkyl spacer was increased to 8, 10, and 12 CH_2 groups in between. Additionally, a shorter surfactant was analyzed with four CH_2 groups in the spacer and two CH_2 groups at the end. The CMC was measured for the short surfactant and AzoC6, which lie at 5mM and 0.5mM, respectively. A lengthening of the hydrocarbon chain leads to a decrease in CMC: 0.18, 0.06, and 0.04mM, reported for 8, 10, and 12 CH_2 spacers, respectively.[14]

Similar measurements as those presented in **Section 3.3** were conducted. In those measurements, the dependence of surfactant concentration on LDDO was investigated. For each surfactant, the maximal radial particle velocity was analyzed as a function of surfactant concentration (**Figure 5.5**). All surfactants show similar cleaning behavior under UV irradiation—however, with different peak velocities. Below the CMC, particles move very slowly and mostly in Brownian motion; at concentrations reaching the CMC, the speed increases drastically until it reaches a maximum at surfactant concentration to be multiples of the CMC, followed by a slight decrease at larger concentrations. When the surfactant concentration is normalized by the CMC of each surfactant, the meaning of the CMC becomes much more clear (**Figure 5.5b**). The results indicate that micellization is essential for flow formation.

One can see that longer surfactants have a much steeper slope than shorter surfactants because of micelle formation (i.e., CMC) at much lower concentrations for the longer surfactants. For example, when the steep increase around the CMC is fitted linearly, the slope of the shortest surfactant is ~0.29µm s^{-1} mM^{-1}. This is in contrast to the longest surfactant, in which the speed increases by ~10µm $s^{-1}mM^{-1}$.

In **Figure 5.6** the peak velocity values obtained from **Figure 5.5** are plotted as a function of the alkyl length of each surfactant, including only the length of the spacer and tail. Note that the azobenzene group is not taken into account, but the spacer is added to the methyl groups of the tail on the end of the surfactant molecule. The picture shows a maximum for LDDO around 10 (AzoC6) and 12 (AzoC8) methyl units. Increasing and decreasing the hydrophobicity leads only to a decrease in speed. The most effective surfactants seem to be those with 10 and 12 methyl groups in the tail.

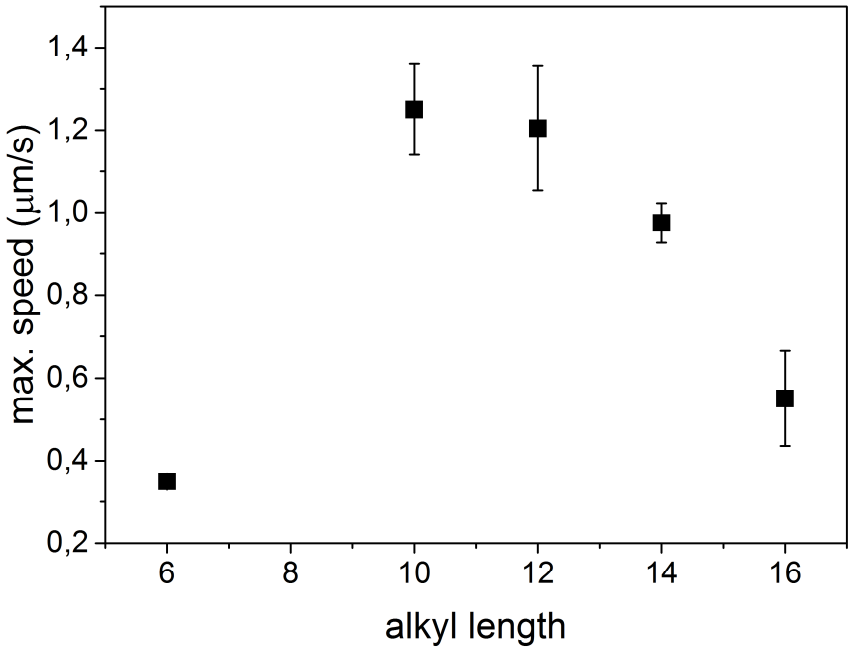

Figure 5.6. Maximal speed in LDDO as a function of surfactants given the length of methyl groups: 6 – AzoC4, 10 – AzoC6, 12 – AzoC8, 14 – AzoC10, 16 – AzoC12. The values were taken from the peak velocities in **Figure 5.4**.

Maximal speeds are reached only above the CMC. This suggests that micelle formation and decomposition plays a major role. As described in **Section 3.3**, the speed depends on the concentration gradient. The micelles serve as an effective source of *cis* isomers during UV irradiation, and micelle decomposition provides a sufficient concentration difference to induce increased diffusioosmotic flows. The results suggest that there is an optimal tail length for this type of surfactant. When speed is taken as measurement, the optimal surfactants are AzoC6 and AzoC8. Most probably, the difference in the adsorbed amount to the surface determines the strength of LDDO flow, as discussed in **Chapter 7**. In both extreme cases, too low and too high hydrophobicity the two isomers become more equal. As the interaction potential differences between both isomers play a major role, LDDO weakens (**Figure 5.5**).

Additionally, an increase in surfactant concentration lowers the Debye length, which, according to the model, lowers the flow speed. This could also explain why the velocity drops when increasing the concentration far beyond the CMC.

5.4 Global light illumination

While a focused laser beam from the bottom generated LDDO flows, the sample was also exposed to additional illumination from the microscope (or environment) with nonfocused light. In most microscopes, a halogen lamp radiates white light—a spectrum that includes all wavelengths in the visible range. This condition is unfavorable when working with azobenzene because it absorbs light ranging from UV to green. Depending on the wavelength, the bulk solution adopts a photostationary state with a specific fraction of azobenzene in the *trans* and the *cis* state. To gain control of the state, a monochromatic light source was connected to the microscope. With this setup it was possible to observe differences in particle speeds in LDDO flows under UV irradiation. For wavelengths in the visible range (i.e., 400nm to 690nm), local UV irradiation created a radial LDDO that drove particles away from the laser spot. The speed of the particles, however, varied with wavelength and the initial distance from the laser spot (

Figure 5.7). Under red light (or in the absence of light), particles on the outside clearly moved outward. However, particles seemed to be more confined under blue light: particles near the laser spot moved, but when they were located farther away, they showed almost no motion. It is apparent that all illumination wavelengths caused particle speed to decrease with increased distance from the laser spot and that switching to longer wavelengths increased particle speed with a saturation starting from 600nm. That increase, however, varied with the initial distance from the laser spot. Whereas the particle speed increased more strongly for particles near the laser spot, the speed increased with longer wavelengths for particles located farther away. For example, particles located between 0µm and 30µm experienced a large increase in speed from ~0.4µm/s to 0.8µm/s between the wavelengths 405nm and 450nm. Whereas farther particles (i.e., 120µm to 150µm) barely increased their speed. At this distance, the speed was more than doubled between 450nm and 532nm. The curves showed a sigmoidal shape. For particles near the laser spot (i.e., between 0µm and 60µm), the increase in speed was close to or beyond the infliction point of the curve. However, for particles further away (i.e., distances from 60 µm) the increase in speed appeared before the infliction point. Under blue light (λ = 450nm), particles from 0µm to 60µm moved

clearly away from the laser spot, whereas more distant particles barely moved at all. Under red light (similar to no illumination), however, all particles showed considerable motion.

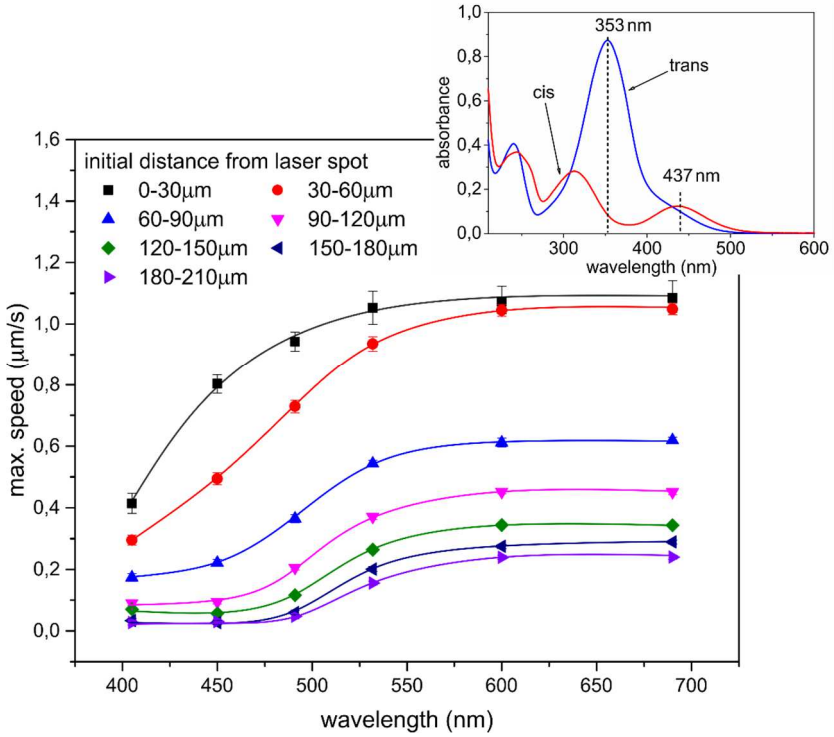

Figure 5.7. Maximal particle speed as a function of illumination wavelength in LDDO under UV irradiation. Experiments were conducted under the following experimental conditions: P = 1.5µW; c_{AzoC6}=1mM, 1-2 minutes of illumination before the UV laser was switched, a sealed microchannel of substrate. The inset shows the absorption spectrum of AzoC6 in water solution.

The results show that illumination can strongly influence LDDO. This may be a result of the photostationary state the bulk solution adopts under certain illumination. Illumination with wavelengths 600nm or longer leaves the surfactant isomerization unaffected. Surfactant is almost found in a 100% *trans* state. An illumination with shorter wavelengths leads to isomerization and, thus, another stationary *trans* to *cis* composition. For example, the *trans* to *cis* fraction is about 2:1 in blue light, decreasing even more with lower wavelengths.

The strength of LDDO, however, depends on the concentration gradient of *cis* above CMC. Illumination with wavelengths ranging from UV to green light decreases this concentration gradient because it already switches a certain amount into the *cis* state. Therefore, under local UV irradiation, a smaller amount of *trans* is switched to

cis. Hence, the concentration gradient is decreased, and LDDO strength drops.

In short, illumination wavelength has an effect on LDDO strength. Wavelengths beyond the absorption bands of azobenzene yielded the best results regarding speed. Particle speed also depended on the initial distance from the laser spot. Under blue light, motion was more confined to central particles, and left those on the outside more unaffected than UV irradiation in red light. Illumination with visible light created a photostationary state with azobenzene in certain fractions of *trans* and *cis*. As LDDO at the glass surface depends on the *cis* concentration gradient according to the theory of LDDO (discussed in **Chapter 4**), the largest gradient builds up under UV irradiation when a large amount of azobenzene surfactant is present in the *trans* state. A high fraction of *cis* decreases LDDO efficiency.

Switching from blue to red light (similar to dark) after continuous blue illumination the particle speeds resemble similar values for outward motion as found in **Chapter 3.** This recovery leads to a question regarding what kind of effect kinetics have on LDDO. Constant illumination of blue light, for example, constantly switches surfactant to maintain a 2:1 fraction of *trans* to *cis*. Therefore, *trans* surfactant is always found in solution. The concentration gradient that induces LDDO should be found in a stationary state as well. The duration of this flow should be unlimited, whereas for red light (i.e., nonisomerizing light), a constant conversion from *trans* to *cis* should lead to a drop in flow and finally to a stop. This, however, has not yet been analyzed, so this question is left open.

5.5 Particle motion depending on the focal plane of the laser

This section discusses how the focal plane of the UV laser affects the particle speed and distribution with regard to outward motion. To investigate this point, we constructed a sample consisting of three solid-liquid interfaces placed on each other, a so-called sandwich sample (**Figure 5.8**). The distance between the glass surfaces was kept constant (~150µm), ensuring constant volume of the surfactant solution.

The UV laser was then focused onto the middle layer (2). On the low (1) and high layers (3), a ring-shaped pattern developed with larger particle density in the center, followed by a depleted ring shaped area toward the outer edge (**Figure 5.8**). The diameter of the ring was larger than that of the middle layer (2). When the laser focused

on the top layer, particles moved away from the beam center. At the layers below, however, rings developed with a larger diameter than those in the middle and low layers (**Figure 5.8ii**). A similar particle distribution was created by irradiation with a focal point at the low layer, but in inverted direction (**Figure 5.8iii**). To this point, the laser was focused in the focal plane of the objective. When the laser focus was shifted to the high layer, away from the objectives' focal plane, the observed particles in the middle plane moved outward with a ring distribution similar to that from **Figure 5.8ii**, which is shown in the micrograph in **Figure 5.8iv**. Tracking analysis for the latter case revealed that particles in the center were moving outward but much slower than particles initially located inside the depletion area. As a result, depending on the irradiation time, the central position was depleted as well. These results are similar to the results discussed in previous studies[109], where we found that particle velocities depended on the initial distance from the laser spot center. This finding indicates that the induced flow is strongest at the edge of the laser beam, where the concentration gradient of *trans* and *cis* is the largest. Thus, a sharp concentration gradient due to micelle decomposition and surfactant-surface interaction seem to be the major players forming these surface flows.

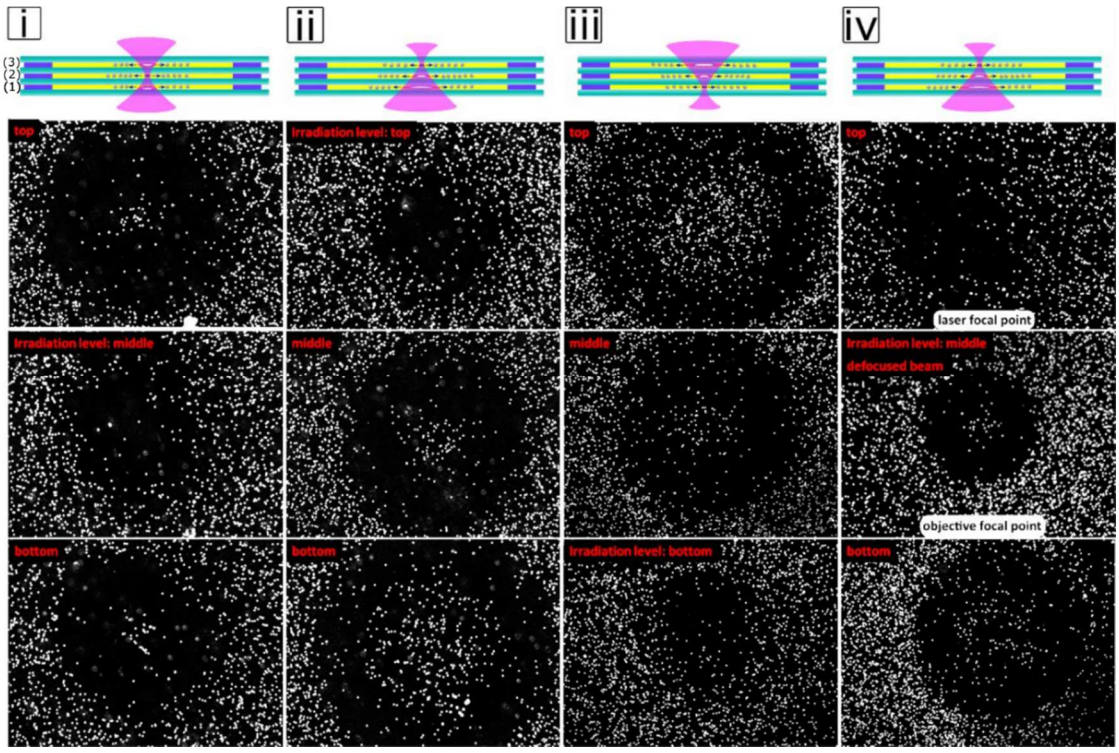

Figure 5.8. Irradiation scheme of the sandwich sample and corresponding micrographs showing particle distributions. Focal point of UV laser in (i) middle (2), (ii) high (3) and (iii) low layer (1). Particles moved away from focal point, but they moved much slower when the laser was unfocused. This defocused irradiation resulted in a kind of ring—with a depletion of particles and higher particle density in the center and on the edges. In (iv) the focal point of the laser was shifted to the high layer while maintaining the focus of observation (focal point of the objective) on the middle layer. The time of measurement was about 5 minutes.

5.6 Summary and conclusions

Light-driven diffusioosmosis is sensitive to various parameters, such as salt concentration, surfactant hydrophobicity and concentration, and illumination parameters. Low salt concentrations can suppress LDDO. Particle size and shape leave maximal velocities largely unaffected. In the case of particles smaller than 1µm, Brownian motion may disturb a clear separation, and the size becomes increasingly important above 10µm. Changing the surfactant hydrophobicity shifts the concentration region in which LDDO occurs. Particle velocities increased pronounced around the CMC of each surfactant—however, with variations in flow velocity. Illumination conditions influence particle motion as well. For example, changing the wavelength from red to blue shrinks the effective area and reduces particle speeds. The

more the wavelength shifts to UV, the slower the particles become. Particles far away from the laser spot tend to speed up less than particles near the laser spot. In addition to illumination on LDDO, the focal plane of the laser spot also results in notable effects. A clearly focused UV laser drives particles from the center. When the laser is unfocused particles on the edge move away, but those on the inside tend to remain.

The fact that the addition of salt diminishes flow strength could be explained under consideration of the theory derived for LDDO which predicts a shrinking of the thickness of the EDL (i.e., Debye length). The variation of the particle size and shape confirms that particles are driven by surface flows and phoretic motion is absent, or at least immeasurable. A change in surfactant hydrophobicity allows the conclusion that micellization is mostly necessary for a strong flow. This suggests that the concentration increase after destruction (or the concentration decrease after formation of micelles) is an important parameter affecting LDDO flow.

A question is left open regarding how much the switching kinetics affect particle speed. It seems that continuous illumination has a separate effect compared to what occurs with illumination prior to UV irradiation. The finding that a focused and unfocused laser generate different particle organizations is of great use. Whenever trying to apply LDDO for cleaning with UV irradiation, a focused laser beam is necessary. The focused UV laser induces a spatial concentration profile; therefore, the largest concentration gradient is near the center of the spot. An unfocused UV laser induces a concentration profile in which the largest concentration gradient is located near the edges of the beam, inducing a flow away from that position, and a ring-like pattern appears.

6 DEPENDENCE OF LIGHT-DRIVEN DIFFUSIOOSMOSIS ON SURFACE MODIFICATION

Until this chapter, the substrate surface was left out of consideration. In the previous experiments, Ibidi microchannels and glass substrates were used as substrate material. Whereas glass substrates are largely hydrophilic, Ibidi microchannels are composed of a more hydrophobic polymer material. As seen from **Chapter 4**, LDDO includes surface excess of the surfactant in the form of Γ_{EDL} and its spatial variation under illumination as necessary for flow creation.

This chapter investigates how LDDO flow and particle motion are affected by 1) surface hydrophobicity and 2) surface morphology.

In the first section, particle motion under UV and green irradiation on hydrophilic samples are observed. This observation includes borosilicate glass, sapphire glass, mica, and glass coated in Indium-Tin-Oxide (ITO). A second section describes particle motion on a Teflon-coated surface under the same experimental conditions. In the last section, particle motion is observed in a system of parallel microchannels with varying parameters, such as channel depth, periodicity, and particle sizes.

6.1 Hydrophilic surface

Glass slides (borosilicate) have been used as model substrates, which yield water contact angles between 13° and 25°. Additionally, motion on ITO-covered glass slides, sapphire glass slides, and mica substrates was observed. To test substrates that are conductive, ITO was chosen as it is used in electronic devices, such as the fabrication of organic solar cells. Sapphire has a crystalline structure and is composed of mostly aluminum oxide groups (Al_2O_3). At a neutral pH, the substrates' zeta potential yield values are between -6mV and +6mV. Mica is highly hydrophilic, is negatively charged (SZP ≈ -80mV), and is a muscovite material with a crystalline

structure. Its layers can be cleaved off so that substrate thickness can vary. Mica absorbs light in the UV range, depending on the thickness of the sample. However, laser power was adjusted to meet similar irradiation conditions. All samples were covered with a cover slip, and a spacer (~400µm) was placed in between to prevent Marangoni flows.

On a glass slide, the flow direction and maximal speeds were investigated for 2µm silica particles under UV and green irradiation at surfactant (AzoC6) concentrations of 0.3mM and 1mM. The analysis of particle motion yielded similar results as those presented in **Section 3.3,** in which microchannels were used. For both concentrations, particle motion directs radially outward with speeds below the CMC, with ~0.3µm/s and above ~1.5µm/s. Under green irradiation, particles move to the laser spot with speed similar to UV irradiation of ~1.5µm/s.

In the case of the other substrates, the flow moves particles away from the laser spot under UV irradiation, whereas green irradiation drives particles inward. The maximal speeds above the CMC are around 1µm/s. Similarly, particle motion below the CMC is much slower, with maximal speeds between 0.1µm/s and 0.3µm/s.

Particle velocity seems to be largely unaffected by the type of the substrate. A slightly weaker flow velocity was identified for mica, sapphire, and ITO-coated glass. Even sapphire shows similar results, although it bears almost no charge at a normal pH in milliQ water. This indicates that surface charge is not a critical parameter for LDDO velocity, although it is considered to be one of the main contributors to surfactant adsorption, which is discussed in more detail in **Chapter 7**.

These results suggest that LDDO is suitable for a great variety of transparent or even semitransparent substrates. As this section focused mostly on flow strength and flow direction of hydrophilic substrates, the influence of surface roughness, crystal structure, and charge was not considered, thus leaving an opportunity for a more detailed investigation in the future.

6.2 Hydrophobic surface

Diffusioosmotic flows induced by UV and green light were analyzed on glass slides coated with Teflon. In contrast to hydrophilic surfaces, one can distinguish three concentration regimes (denoted as (1), (2), (3)), at which particles show different

directions of motion. (1) Below the CMC, the particles are driven toward the laser spot at a velocity of 0.1µm/s under continuous irradiation (**Figure 5.8**). Static images of inward motion are shown in **Figure 6.1a,b**, in which particles are distributed initially and aggregated after 15 min of UV irradiation. The motion of particles was tracked, and their positions were recorded (**Figure 6.1b)**. This aggregation process lasts for hours. This contradicts the situation on glass surfaces, where the particles are moved out of the irradiated area. However, it is important to mention that at the beginning of irradiation (in the range of several tens of seconds), we observed a global displacement of particles, outward from the laser spot at a velocity of 0.3µm/s (**Figure 6.1c-f**). The duration of outward motion and the time at which the particles changed direction inward depend on the initial particle distance: the farther away the particles are initially located from the laser spot, the later they direct inward. This nonequilibrium state is present at concentrations of up to 1mM (i.e., in the first two regimes). At this point, this effect could not be explained. Later, we speculate about the possible reasons.

(2) Increasing the concentration above the CMC to 1mM leads to a more complex motion pattern. Depending on the position relative to the laser spot, two different directions of particle motion are apparent. The particles near the laser spot are driven inward, whereas those situated at distances of more than 40µm move outward (**Figure 6.2**). (3) A further increase in surfactant concentration to 2mM results in particle motion outward, as in the case of glass surfaces. The particle speed is around 1.4µm/s, which is similar to the speeds obtained for glass slides.

In the beginning of UV irradiation, particles show instantaneous outward motion, as if being hit by a wave. This phenomenon might be explained by a sudden pressure rise around the laser spot that is induced by immediate isomerization of surfactant coupled with a concentration gradient around the laser spot. This pressure difference is transmitted outward travelling like a wave—similar to a wave created by a single raindrop falling into a motionless pond. The wave broadens and weakens over distance.

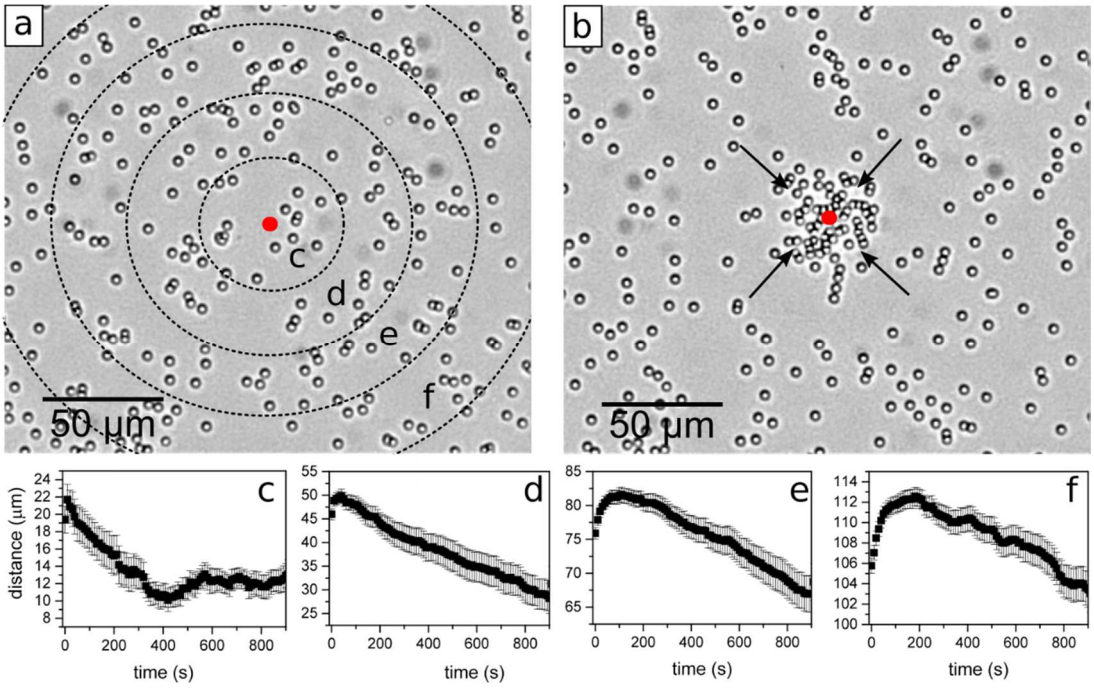

Figure 6.1. Optical micrograph of 2µm silica particles in 0.3mM surfactant solution on a hydrophobic surface with motion analysis. (a) before irradiation and (b) after 15 minutes of UV irradiation. The red dot marks the focal point of the UV laser, and the black arrows indicate flow direction. The averaged particle distance was analyzed as a function of time for particles initially located at distances from the laser spot between (c) 0µm-30µm, (d) 30 µm-60µm, (e) 60µm-90µm, (f) 90-120µm. The dashed lines mark the border of averaging group. The corresponding video can be found in Appendix C6.

Destruction of surface aggregates upon irradiation might explain this initial observation. Inside the EDL, surfactant molecules form surface aggregates (discussed in **Chapter 7**). During isomerization, size and shape change, the dipole moment increases, thus destroying those surface aggregates. This dynamic nonequilibrium process creates pressure in the irradiation center. Continuous irradiation leads to an equilibrium state with an inward flow profile.

Before green irradiation, the solutions were illuminated with UV light to induce a *trans*-to-*cis* isomerization (with a photostationary state of ~90% *cis*). When these solutions were irradiated with green laser light under a red illumination condition, particles moved to the laser spot with similar speeds, similar to what occurred with the glass substrate. No difference to motion on glass substrates could be found as a result of green irradiation.

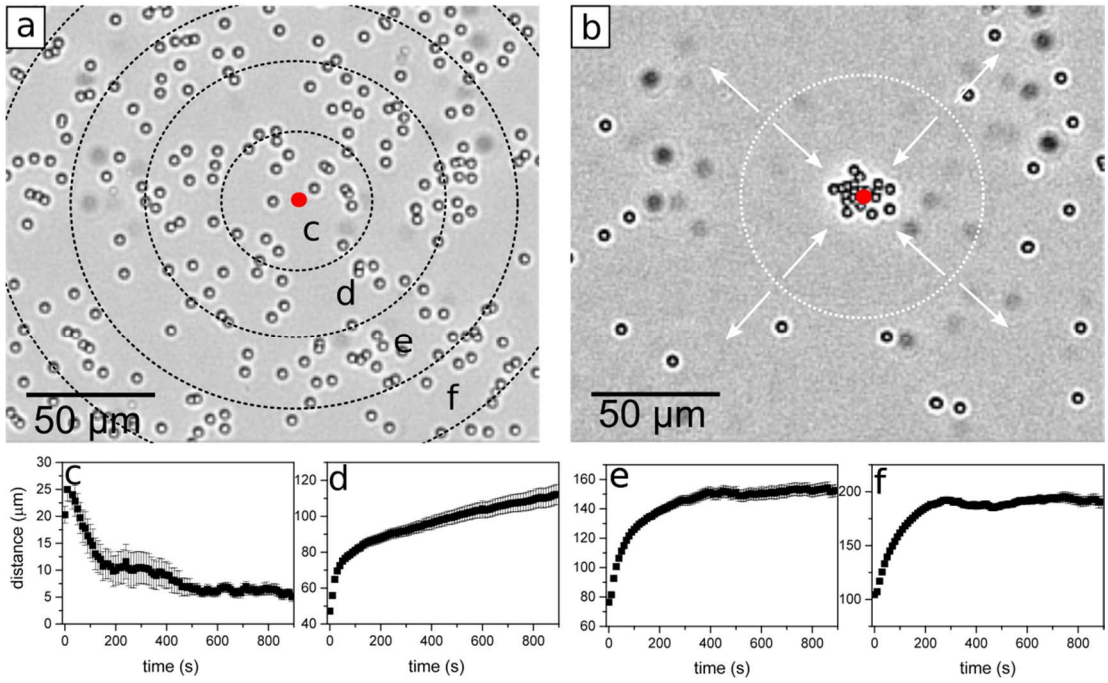

Figure 6.2. Optical micrograph of 2µm silica particles in 1mM surfactant solution on a hydrophobic surface with motion analysis. (a) before irradiation and (b) after 15 minutes of UV irradiation. The red dot marks the focal point of the UV laser, and the white arrows indicate flow direction. The averaged particle distance was analyzed as a function of time for particles initially located at distances from the laser spot between (c) 0µm-30µm, (d) 30 µm-60µm, (e) 60µm-90µm, and (f) 90-120µm. The dashed lines mark the border of the averaging group. The corresponding video can be found in Appendix C7.

To summarize, a light-induced flow under UV irradiation and on hydrophilic surfaces drives particles outward. Particle direction on a highly hydrophobic substrate depends on the surfactant concentration: 1) An inward motion occurs below the CMC (0.3mM). 2) Both an inward and outward motion occur above the CMC at 1mM; particles close to the laser spot drift inward, whereas particles farther away drift outward. 3) Solely an outward motion occurs above the CMC, at 2mM. Under green irradiation, particles move inward in all cases.

The reason for this type of motion is unclear. It is supposed to be related to the adsorption of surfactant in the EDL, which differs from a hydrophilic surface because of modulated surface-surfactant interaction. Returning to the model of LDDO, **Equation (29)** shows that the relative adsorption gradients between *trans* and *cis* should be taken into account. The sign of the equation (i.e., the direction of the flow)

can be inverted depending on the gradients.

What is, however, puzzling is that green irradiation still induces inward motion for concentrations below and above the CMC. Intuitively, the flow profile should change the direction similarly to UV light. Surfactant-surface interaction is therefore measured and its implications discussed in the next chapter.

The relative adsorption of *trans* and *cis* surfactant can lead to a plus or minus velocity—meaning inward or outward flow. For concentrations above the CMC, we assumed only the gradient in *cis* adsorption was relevant.

Surface in pure water has a negative surface charge. When surfactant adsorbs, the total charge of the surface becomes positive (shown in **Chapter 7**). When the surfactant is in the *trans* state, it is likely to pack densely forming surface aggregates. Under UV irradiation, *trans* surfactant is switched to *cis*. Since the transition from *trans* to *cis* can create osmotic pressure in the EDL due to space suddenly necessary for isomerization and a fast change in surface-surfactant interaction. This might explain the outward wave-like flow at the beginning of irradiation. When molecules are switched to *cis* they interact with the surface and may reorientate at the surface. During these steps it is possible that the total surface charge, which has been positive due to adsorption of (positively charged) surfactant, becomes negative. Isomerization leads to desorption of surfactant molecules (shown in **Chapter 7**), releasing most of the molecules and, thus, changing the electrostatic diffuse layer. Differences in the diffuse layer create a gradient leading to a hydrodynamic flow. Adsorption on a hydrophobic surface is lower than on a hydrophilic surface (shown in the next section). Under UV irradiation at the glass surface, total surface charge remains positive. Isomerization most likely does not lead to a strong desorption because hydrophilic *cis* molecules remain at the hydrophilic surface. Only reorientation of *cis* surfactant occurs at the surface. When surfactant remains adsorbed, total surface charge remains positive. This is in contrast to UV irradiation on a hydrophobic surface. A switch from hydrophobic *trans* to hydrophilic *cis* pushes surfactant molecules away from the surface. Desorption can be so large that the total surface charge drops into the negative regime. The negative total surface charge appears only in the vicinity of the laser spot. Farther away it remains positive. Between those points, surface charge should pass the isoelectric point and change from negative to positive. At this point, the diffuse layer in which flow is

generated, disappears. When there is no diffuse layer, flow stops. From this point, flow is created toward and away from the laser spot. Below the CMC, the picture might look different. When above the CMC, micelles and hemi-micelles decompose.
Under green irradiation, *cis* molecules are switched to *trans*. It is unclear how *cis* molecules adsorb to the surface because they are more hydrophilic than *trans*, which should cause them to adsorb less to a hydrophobic surface. Surfactant in *cis* state should adsorb more easily to a hydrophilic surface. However, when surfactant adsorbs beyond the isoelectric point (IEP), at which surface charge is compensated, hydrophobic interaction drives further adsorption. That is why the elongated and more hydrophobic *trans* state adsorbs much more easily at concentrations above the IEP. The gradient in *cis* concentration is responsible for the flow. When *cis* is switched to *trans* around the laser beam, surfactant adsorption increases

6.3 Motion on a structured surface

This section describes what occurred when the surface was structured with microchannels to examine its effect on the flow and on particle motion.

Stamps made of PDMS were prepared using a thin polymer film that had the morphology of a surface relief grating (SRG). The microchannels had sinusoidal shape, schematically shown in **Figure 6.3d**. Silica particles of different sizes were used to analyze the effect of microchannels on the motion. The depth and grating of the channels were varied to investigate their effect on particle motion.

In **Figure 6.3** particle motion on a grating is shown. A UV laser was focused at a spot in the image center. Seven micrometer-wide particles were dispersed in a solution of azobenzene containing surfactant (AzoC6) at a concentration of 1mM. Before irradiation, the particles lied inside the grooves of the grating. When the laser was switched on, the light-induced flow drove the particles along the channels. The particles were dragged continuously outward and left the observed area, with only a few of them seeming to remain in place. Most of these nonmoving particles were lying along a line that went through the laser spot and was perpendicular to the grooves (**Figure 6.3c**.)

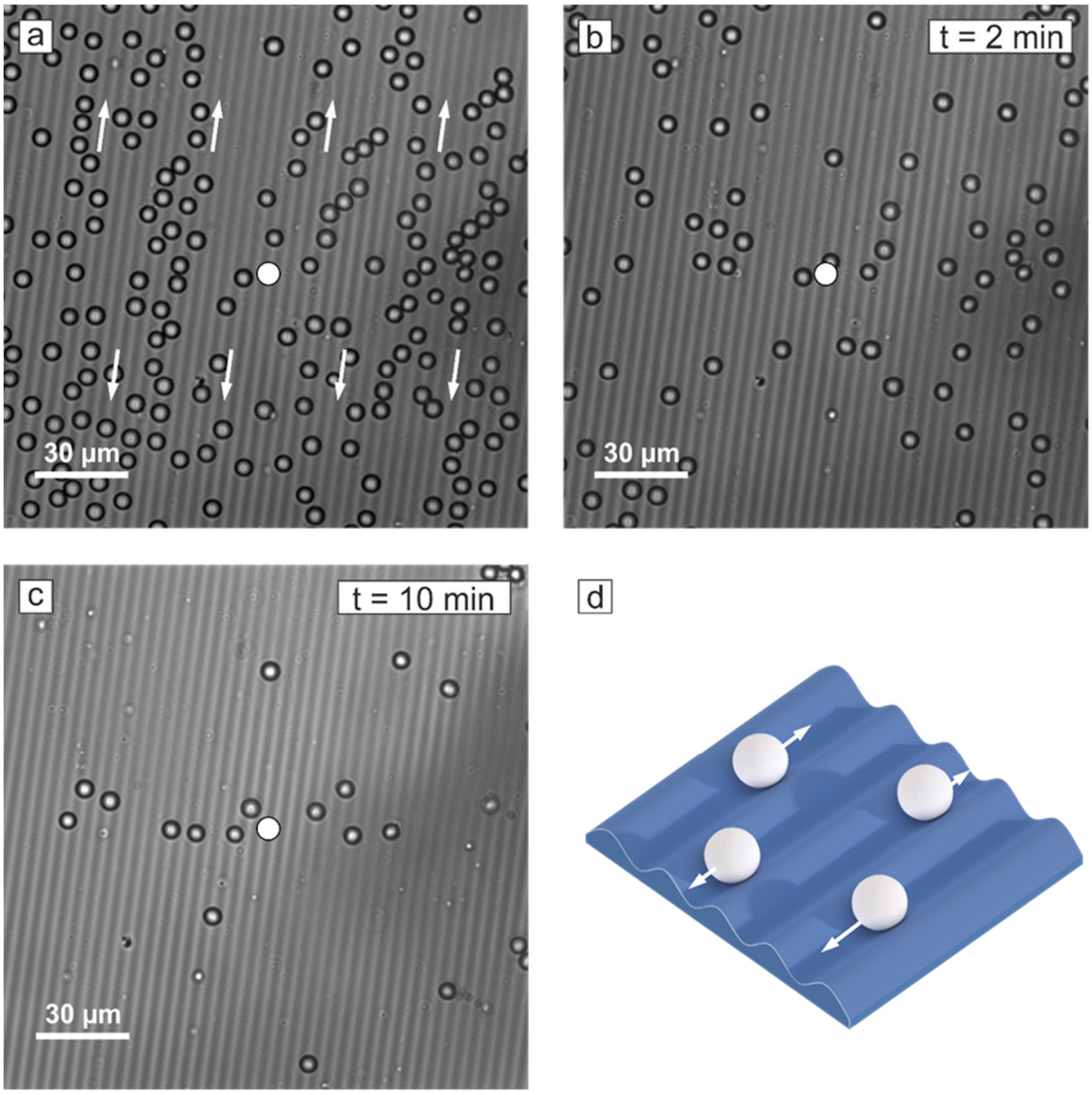

Figure 6.3. Micrographs of the motion of silica particles (5µm in diameter) on a structured PDMS surface. Focused UV light at the white spot induces the motion. Particles are dispersed in a solution of azobenzene surfactant (concentration: 1mM). The grating has a periodicity of 5µm and a height of 800nm. (a) Before start of irradiation, (b) after 2 minutes, and (c) after 10 minutes of irradiation. The white arrows indicate the direction of particle motion. In (d) a scheme of particle motion along the structured surface is shown. The corresponding movie can be found in Appendix C8.

Tracking the particles revealed more details about their motion (

Figure 6.4). The trajectories indicate that most particles move along the channels, however, some particles jumped to neighboring channels. Most of these jumping particles were located near the laser spot, circumscribed by the white line in

Figure 6.4.

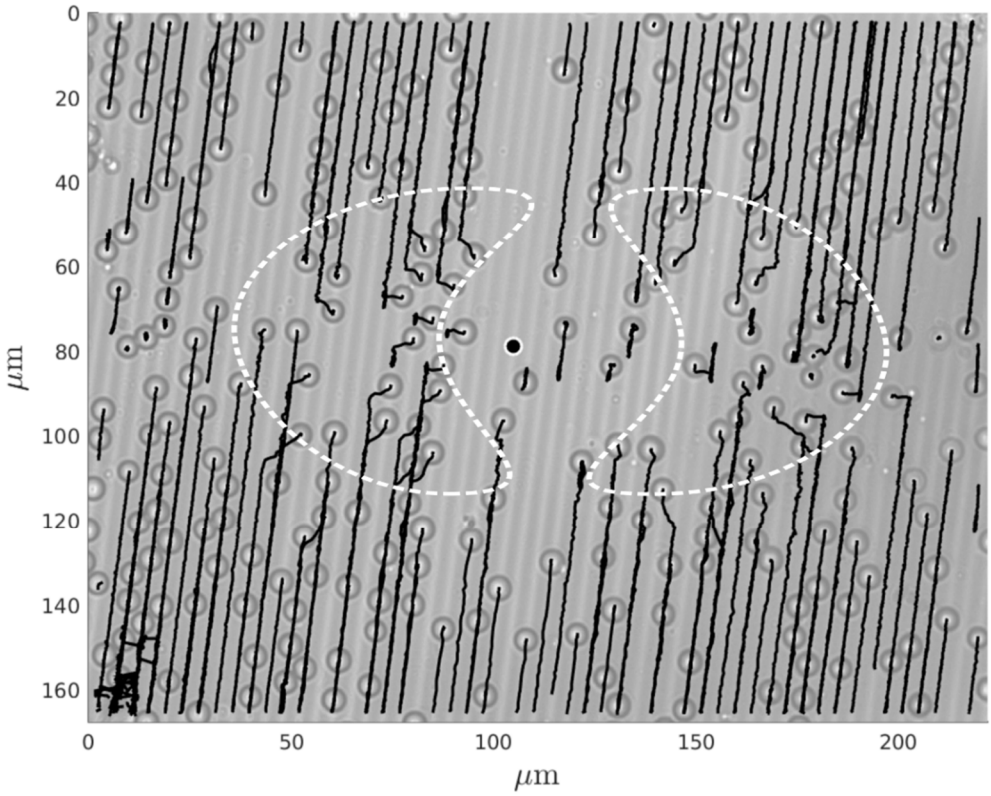

Figure 6.4. Micrograph of silica particles (d = 5µm, c_{AzoC6} = 1mM) including their trajectories. The white dashed line surrounds the area at which the particles jumped across channels. The grating periodicity was 5µm and the grating depth was 800nm.

Particle motion was mostly influenced by the initial position of the particle (i.e., the vector pointing from laser spot to particle). The particles jumped in the direction of this vector when located at a specific distance from the laser spot. The distance travelled by the particles along the channel direction continuously increased (**Figure 6.5a**). When analyzing the motion normal to the channel, the distance increased in multiples of ~5µm (SRG periodicity) but only at the beginning of irradiation, which represented the jumps across the channel (**Figure 6.5b**). This indicates that particles can jump not only one channel but also several channels.

These observations suggest that even though the surface is structured, the circular symmetry of the flow remains. Despite of the radial flow, the channels guided most particles along their direction; only close to the laser spot was the flow strong enough to push particles over the rim of the channel into a neighboring channel. Only the initial flow could create enough force to lift particles over the channels. When the

flow was established, it was no longer strong enough to further lift particles, which is why the particles remain in their channels.

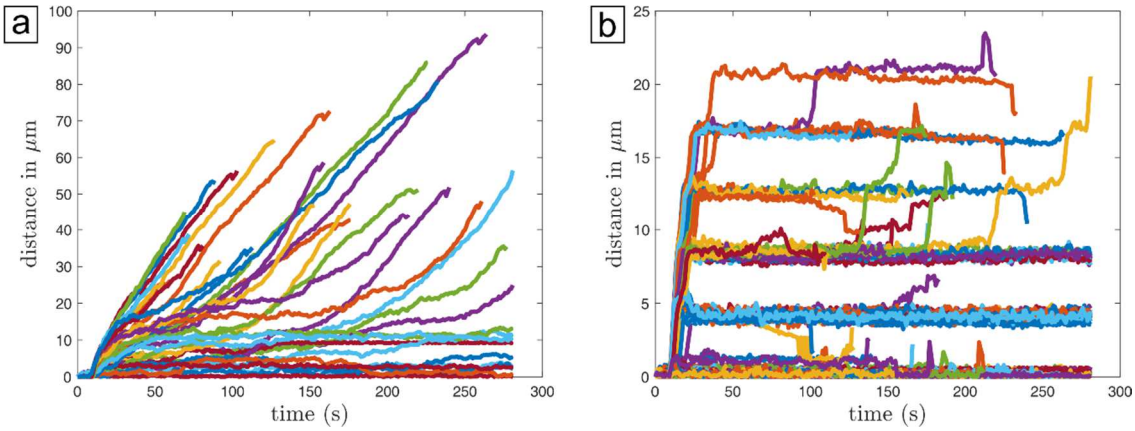

Figure 6.5. Single particle motion displayed as evolving distance from their initial position (a) along channel direction and (b) normal to channel direction. Different colors represent the displacement of single particles.

When the flow was directed away from the laser spot, the velocity component in channel direction, which could be seen as an effective flow, drove particle motion. Thus, the effective flow in channel direction was much weaker than the full flow strength on a flat surface. This explains why particles barely moved when they lied in the line that goes through the laser spot and is perpendicular to channel direction.

This is reflected also in the average velocity of the particles when all particles were considered in the calculation. The maximal velocity in channel direction was 0.3µm/s (**Figure 6.6**).

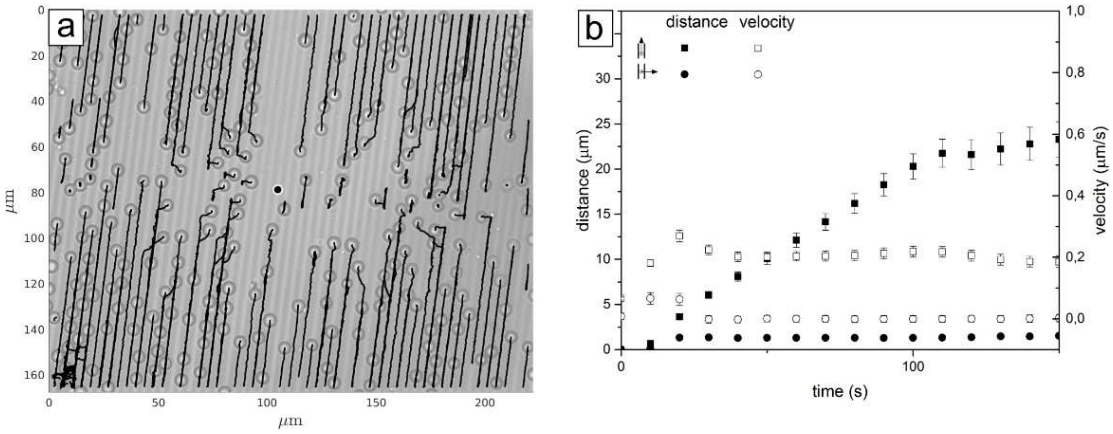

Figure 6.6. (a) Micrograph of light-induced motion of silica particles (5µm) on a surface grating (periodicity: 5µm; SRG depth: 800nm). Black lines show single particle trajectories. (b) Averaged distance (closed symbols) and velocity (open symbols) of all particles normal and perpendicular to the grating.

When particles are not taken into account for velocity calculation that lie in a certain area (**Figure 6.7a**), particle speed almost triples. A closer look into the velocity components that occurred in the direction of the channels and perpendicular to the channels shows that particle motion across the channel was almost negligible (**Figure 6.7b**). The highest velocity was found directly after the laser was switched on but decreased with time, which happens when particles were guided away from the laser spot.

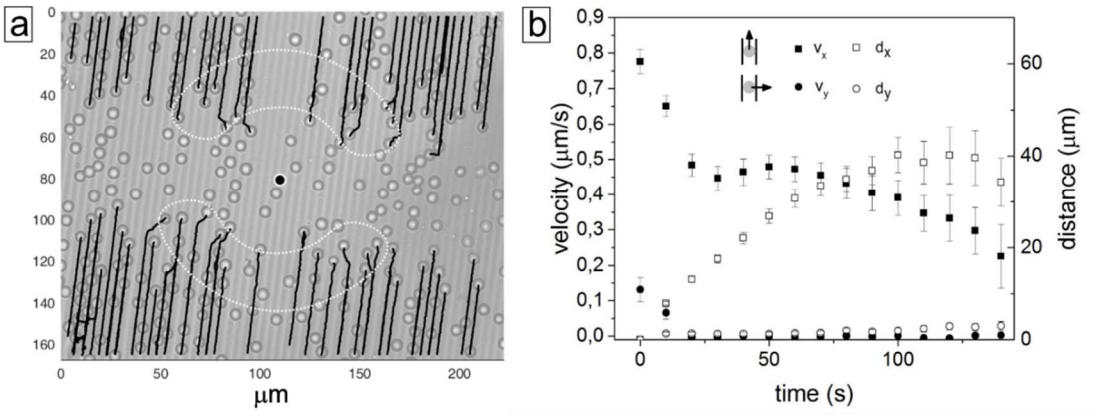

Figure 6.7. Particle motion of selected particles. (a) Micrograph of particles considered for calculation of particle speed surrounded by the white dashed line. (b) Averaged particle speed and distance from initial position as a function of time separated for motion in (squares) and normal (circle) to channel direction.

The detailed view on the motion of single particles (**Figure 6.5a**), revealed that a few particles tended to stay near their initial position but moved on later. This can be due to several reasons. First, particles line up in a queue along the channels. Therefore, they are confined to move one-dimensionally. When other particles occupy the same channel, the particles on the inside cannot move farther until the occupying particles have left, reducing overall particle speed. A second reason for the delayed movement may result from the hydrophobicity of the PDMS. As shown in the previous section, surface hydrophobicity has a strong influence on flow direction. Therefore, particles could be hindered from moving when they are too close to the laser spot. When they arrive at a certain distance from the laser spot, they accelerate and leave this area. A third reason could result from the focus of the laser spot with a 40x objective. In measurements on a flat surface, it was seen that particles near the laser spot tend to remain longer at their position, similar to the motion observed in **Section 5.5**, in which the influence of the focal point of the laser was discussed.

6.3.1 Particle size

To check whether the size of the particles placed in the microchannels alters particle velocity, we varied the diameter from 1.5µm, to 5µm, to 7µm, and to 10µm. The maximum velocity along the channels was measured, and the trajectories were analyzed.

Decreasing the size of the silica spheres to 1.5µm in diameter yields different results. The trajectories of the spheres show that they moved radially outward with a tendency to move along the channel when SRG periodicity was 3.5µm (**Figure 6.8a**). At a higher SRG periodicity of 5µm, the 1.5µm particles exhibited almost radial trajectories (**Figure 6.8b**).

An analysis of particle motion leads to the following conclusion: the motion normal to the channel reveals that particles can jump from one channel to another. When not jumping they stay in a channel for some time, exhibiting motion along the channel (**Figure 6.9b**). In short, particles move partially along the channels and partially jump multiple times. This movement depends on the initial position of the particles. **Figure 6.8a** and **Figure 6.9** show that particles jumped across multiple channels when they were located near the line that goes through the laser spot and lies

perpendicular to the channel direction. Indeed, the initial flow lifted the small particles over many channels. When they traveled far enough (i.e., around 50µm from the laser spot) those particles jumped less often and tended to follow the channel direction. When the particles were located more in the direction of the radial flow (for example, along the vertical line through the laser spot), they tended to stay in a channel but also sometimes jumped to neighboring channels. Similar to the motion observed for the 5µm particles, particles near the laser spot spent more time at their initial position before they moved. The maximal speed along the channel was similar to the speeds found for the silica particles of 5µm size with ~0.5µm/s.

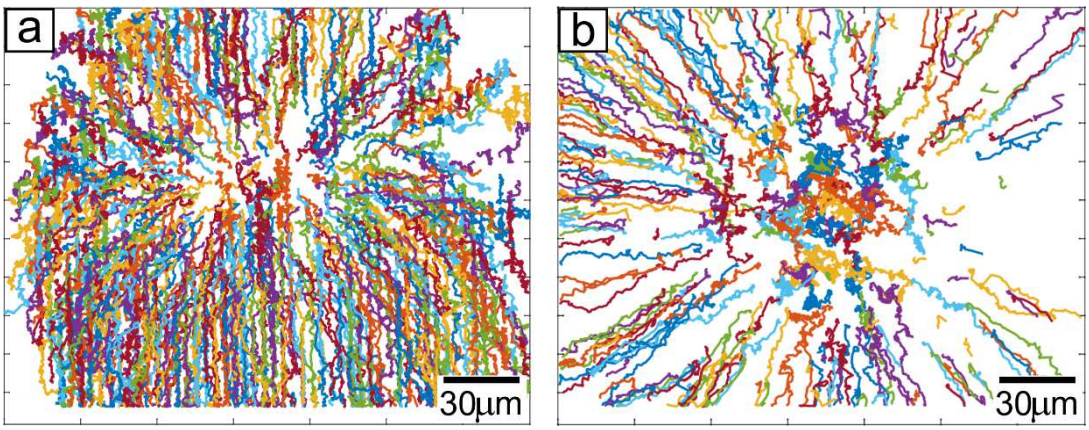

Figure 6.8. The lines display the trajectories of single 1.5µm silica particles on a structured substrate under local UV irradiation: (a) a grating periodicity of 3.5µm and channel depth of 800nm; (b) periodicity of 5µm and SRG depth of 800nm.

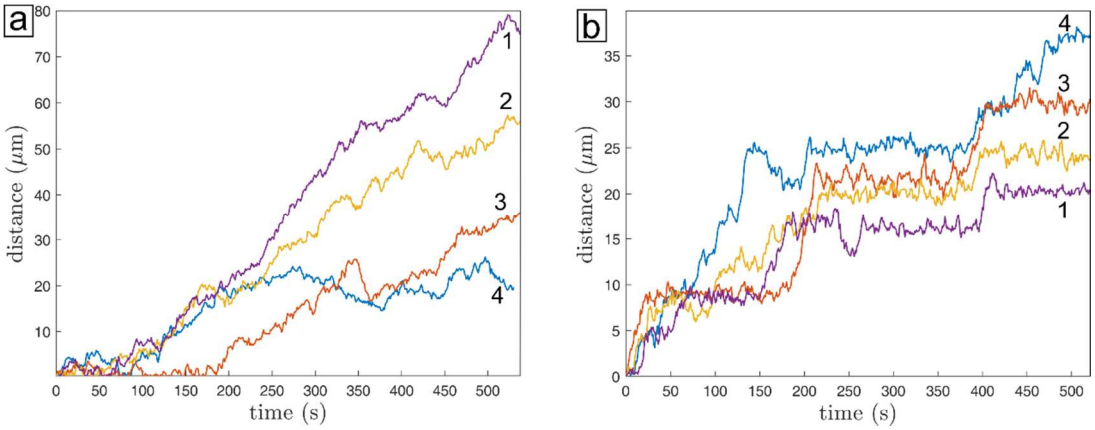

Figure 6.9. Moved distance (a) parallel and (b) perpendicular to channel direction as a function of time for four (numbered) single particles (1.5µm in diameter) on a patterned surface with periodicity of 3.5µm and SRG depth of 800nm, from **Figure 6.8**.

Increasing the particle size to 7µm or 10µm left the type of motion mostly unaffected with results similar to those found for 5µm particles. They preferred to move along the channel, occasionally jumped across one channel, with less jumping probability for 10µm particles. When analyzing particle speeds in and against channel direction, the maximum speeds were similar for sizes from 1.5µm to 10µm (**Figure 6.10a**). An analysis of particle speed normal to channel direction, only for 1.5µm-sized particles motion across the channels could be observed, without taking into account the initial jumps from channel to channel of the larger particles (**Figure 6.10b**).

When particles are smaller, their mobility is higher due to Brownian motion; they are less confined to the channels. Thus, these small particles can jump from channel to channel by Brownian motion, even in the absence of a flow. The flow can lift these particles much more easily from channel to channel so that they tend to jump across several grooves. This indicates that the flow remains radial, regardless of the surface pattern.

The previous results were obtained for SRG periodicities of 3.5µm and a channel depth of 800nm. A change in these parameters can greatly affect the guiding properties of the surface, which is shown in the following section.

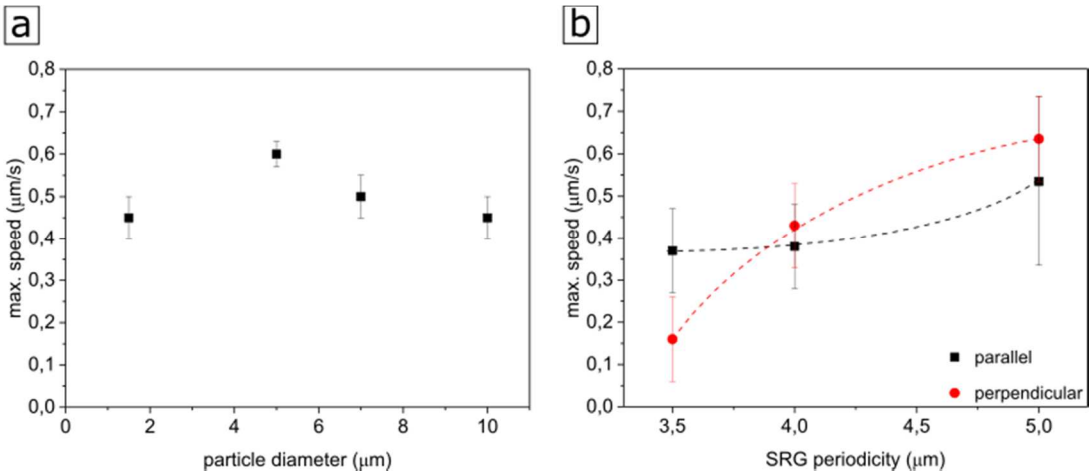

Figure 6.10. (a) Maximal speed in channel direction as a function of the particle diameter for an SRG of 800nm depth and 3.5µm periodicity. The maximal speed normal to the channel direction is negligible despite the jumps of particles larger than 1.5µm. A change in periodicity leaves the particle speed along channel direction constant for all particle sizes. (b) Maximal velocity of particles as a function of the periodicity with grating depth of 800nm.

6.3.2 Dependence on grating depth and periodicity

When varying SRG periodicity, the steepness of the SRG changes. An increase in periodicity lowered the steepness and also gives more space for the particles. **Figure 6.11** shows a scaled view of different particles with varying SRG properties.

An increase in periodicity primarily affected particle motion normal to channel direction for 1.5µm particles. For larger particles, maximal speed along and across channel direction remained the same. A closer look at the trajectories of 1.5µm particles on an SRG with 5µm periodicity (800nm depth) shows that they moved radially outward. This indicates that the grating structure leaves particle motion unaffected. Indeed, when comparing maximal speeds along and across channel direction (**Figure 6.8a** and **Figure 6.10b**), particle speeds at 3.5µm periodicity differ, but an increase in periodicity to 4µm and 5µm correlates with an increase in particle speed across the channel, with similar particle speeds along and across the channel direction. Periodicity seems to have affected particle speeds only partially, showing a slight increase for 1.5µm particles.

The grating depth affected particle speed similarly for all particle sizes. With a decrease in the depth from 800nm to 400nm, particle speeds along the channels were barely affected; particle speeds increased slightly to 0.5µm/s. The grating depth had a greater effect on the motion across the channels, especially for particles of 1.5µm size. At a periodicity of 3.5µm, a decrease in grating depth results in an increase in particle speeds from 0.1µm/s to 0.35µm/s, almost reaching the particle speed along the channel with 0.45µm/s. For larger particles, a decrease in depth resulted in jumps over numerous channels, which happens exclusively at the initial switch on of the laser light.Particle motion was affected by SRG periodicity and depth. Mostly the motion across channel direction was affected. Whereas for particles between 5µm and 10µm, the number of jumps increases, 1.5µm particles are more strongly affected. With low grating periodicity and larger depth, they were guided along channels. However, because they are more mobile than larger particles, they were also easily able to jump to neighboring channels. An increase in periodicity or a decrease in depth shows that they begin to “ignore” the underlying structure. A scaled view, as shown in **Figure 6.11**, clarifies how particles fit within the channels. The 1.5µm particles are especially confined within the channels. Due to the strong effect of Brownian motion this picture

does not hold true; they have constantly moved across the channels. That is why they can travel across channels if channel height is too small or periodicity is too large. The flow hardly needs to lift them over the rims of the channels. An increase in channel depth, however, should confine those particles inside the channels.

The larger particles were less affected by Brownian motion. Therefore, they barely moved and remained inside the channels. The flow had to lift the particles over the rims of the channels, which was only possible if the force on the particles was large enough. This did occur for particles close to the laser spot at the initial switch on of the laser.

When periodicity increases or depth decreases, the steepness of the channel borders decreases, and the force needed to push the particles over the rims of the channels also decreases. This jumping was more pronounced for 5µm and 7µm particles. 10µm particles barely showed this jumping motion. The reason for this is a combination of lower mobility and weaker flow because the 10µm particles were more distant from the surface. This is similar to the explanation in **Section 5.2**, in which the flow decreased with distance from the surface, which was schematically shown in **Figure 5.3**.

Along the channels, averaged motion of particles seems to be smaller than for particles on a flat surface. When the full flow could act on the particle, the speed was still lower. For example, on a flat PDMS surface, 5µm particles had a maximum averaged velocity of ~1.4µm/s (~1.6µm/s on glass). Maximum velocities of single particles during a fully effective flow reach only 1µm/s. A lower speed could be a result of the increased distance from the surface. As flow strength decreases with distance from the surface, a weaker flow acts on the particle. Furthermore, friction between surface and particle could reduce the flow speed and trap particles. This seems to affect the 10µm particles to a greater extent.

In addition, some single particles showed unusual behavior. They did not move until they had reached a certain distance, and then they accelerated. The reason for this could be related to the focus of the laser beam, which could have been too broad to create a concentration gradient that is most effective at a certain distance from the laser spot. This is similar to what is presented in **Section 5.5**, in which the focal plane of the laser was changed. Another reason for the unusual behavior of single particles might

stem from the hydrophobicity of the PDMS surface, which could prevent particles from moving away from the laser spot. This effect is shown in **Section 6.2**.

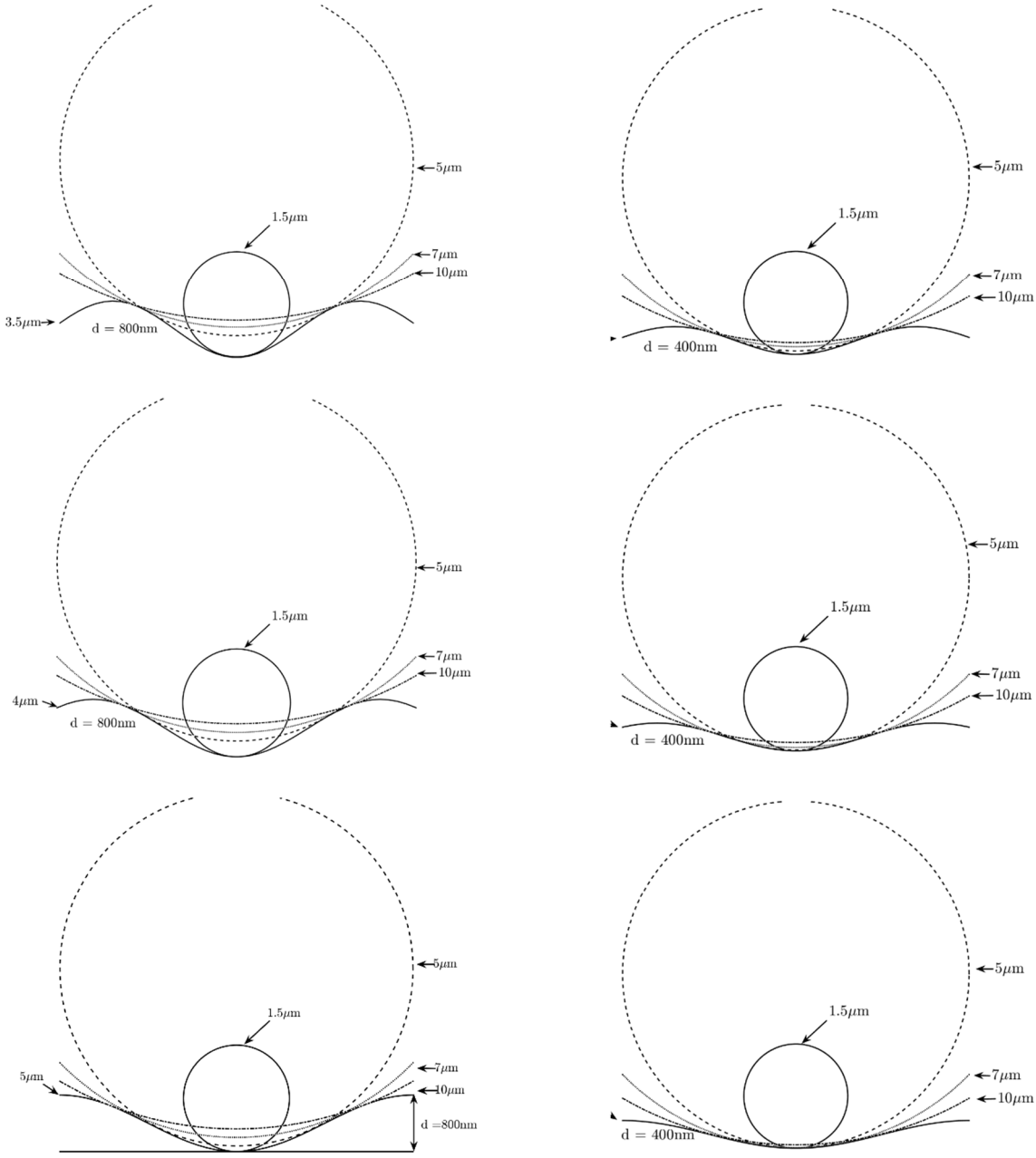

Figure 6.11. Drawings of particles on varying SRGs with increasing periodicities from top to bottom: 3.5µm, 4µm, 5µm; and variation of SRG height from left to right, with 800nm on the left and 400nm on the right.

6.4 Summary and conclusion

It was shown that surface modification affects the speed and flow direction of particle motion. On a hydrophilic and slightly hydrophobic surface, particle motion was directed outward with only slightly lower maximal speeds on surfaces made of mica or ITO. Glass and ibidi polymer resulted in maximal speeds of around 1.5µm/s. Making the surface strongly hydrophobic could invert LDDO flow under UV irradiation when surfactant concentrations were below the CMC. At four times the CMC, the flow turned outward. At concentrations in between, a transition phase appeared at which the flow could be inward and outward depending on the distance of the laser spot. Because inward motion appeared near the laser spot and outward motion at a farther distance away, a specific structure could be formed: particles gathered at the center surrounded by a particle-free area. The initial irradiation generated an outward motion in all cases. Continuous irradiation then led to inward flow. A green irradiation on a *cis*-dominated solution induced inward motion in all cases.

To summarize the effect of an underlying structure (i.e., a surface relief grating), particle motion was analyzed with variations in particle size, SRG periodicity, and depth. Most particles moved along the channel direction with some restrictions. Small particles could move normal to the channel. Especially at high periodicity and low depth, they followed the radial flow profile. As particles became larger, they were more confined to channels. Only the initial flow could lift 10µm particles to neighboring channels. Some particles remained in their position. This was influenced mostly by the angle between flow and channel direction—that is, when flow and channel direction formed a 90° angle. Thus, single particle speeds have shown to depend on the initial position, which was a result of an effective flow. This effective flow has shown to depend on the distance to the laser spot and on the angle between flow and channel direction. The flow was most effective when the channel direction coincided with the radial direction of the flow. For the large particles, a change of periodicity and depth barely affected the motion in the channel direction. Only the number of jumps across the channels was increased by decreasing the depth or increasing periodicity. Averaged particle speeds were similar for all particle sizes along channel direction.

The findings of this chapter show that surface modifications affect flow profile

and particle motion. When a channel structure was inscribed, particles could be guided; however, this guidance was limited due to the maintained profile. Because the guidance of large particles was an expected result, the complex flow observed for a hydrophobic surface is somewhat puzzling and leads to new questions. This is especially true for the fact that green irradiation caused an inward flow in all cases. When an SRG channel structure is used as a guide, one should consider particle size. Particles larger than 5µm in diameter can be guided. Smaller particles need deeper gratings and a suitable periodicity. A more suitable way to manipulate particle motion is shown in **Section 8.3**, in which the beam shape is modified. The flow profile was unaffected by the investigated surface morphology because the EDL has a thickness of less than 10nm compared to a micrometer-sized structure. Additionally, the smooth up and down of the SRG leaves the flow unaffected. Surface flow induced by EDL is affected mostly with abrupt changes and only if the size of the EDL is similar to the size of the nanochannels.[118] Surface hydrophobicity alters the surface-surfactant interaction. This has, according to the theory, an effect on the surface excess of *trans* and *cis* surfactant. An interpretation of the result is rather difficult and requires further experimental observation. Therefore, surfactant adsorption is measured and discussed in the following chapter.

7 SURFACTANT ADSORPTION*

Light-driven diffusioosmosis depends on surfactant-surface interactions, and this is reflected in the parameter Γ_{EDL} (i.e., the surface excess of surfactant in the diffuse layer). In the last chapter, it was shown that the direction of LDDO flow depends on the hydrophobicity of the carrying surface. Under focused UV irradiation on a hydrophobic surface, an inward flow develops for concentrations below the CMC. The flow profile changes to a more complex form; it is both inward and outward at 1mM and finally turns outward only at 2mM. On hydrophilic glass substrates, irradiation with UV light always leads to simple outward flows, and, regardless of surface hydrophobicity, the flow points inward under irradiation with green light.

In this chapter we investigate how surfactant adsorbs on hydrophilic and hydrophobic substrates when the sample solution is either in the dark state (100% *trans*) or UV illuminated (~90% *cis*) state. From adsorption isotherms and kinetics as well as surface zeta potential measurements, we are trying to determine 1) how irradiation alters surfactant adsorption, 2) how LDDO can be explained, and 3) why motion on the hydrophobic surface flow direction changes under UV irradiation.

Surfactant adsorption isotherms were measured on both hydrophilic (glass) and hydrophobic (Teflon AF1600) substrate for the two isomers as a function of surfactant concentration and time. Additionally, the surface zeta potential adds knowledge about electrostatic surfactant-surface interaction of both states.

7.1 Surfactant adsorption on surfaces

A glass surface in contact with water is negatively charged. When surfactant molecules are added to the water, an excess of surfactant near the interface occurs due to electrostatic interactions resulting in the electrostatic diffuse layer. The adsorbed

* The experiments were conducted by Maren Umlandt in the framework of her master thesis supervised by myself.

surfactant molecules reshape the surface properties by changing its surface charge and hydrophobicity. From the total amount of adsorbed molecules, information about surface potential and type of interaction can be obtained.

Surfactant adsorption on hydrophilic surfaces, such as silicon dioxide, has been measured extensively and has been summarized in several review articles.[35, 36, 119–123] Surfactant adsorption is driven by different types of interactions. It can be expressed in terms of Gibbs free energy change when a surfactant molecule is adsorbed. The adsorption density in the Stern plane Γ at a surface is given by the following:[124]

$$\Gamma = lCe^{-\frac{\Delta\overline{G^0_{ads}}}{RT}}$$

where l is the effective length of the molecular chain, C the bulk surfactant concentration, R the gas constant, T the absolute temperature and $\Delta\overline{G^0_{ads}}$ the standard free energy of adsorption which is the sum of the following:

- electrostatic interaction ΔG^0_{el},
- chemical interaction ΔG^0_{chem},
- hydrophobic lateral interactions $\Delta G^0_{hyd} = \frac{n(\mathrm{CH_2})\phi}{RT}$ ($n(\mathrm{CH_2})$ – number of $\mathrm{CH_2}$ groups, ϕ – transfer energy for each group ~1kT[125],
- hydrophobic interaction between hydrophobic sites at the solid and the alkyl part of the surfactant ΔG^0_{c-s},
- hydrogen bonding between surfactant and surface sites ΔG^0_H,
- desolvation energy ΔG^0_{H2O}, (i.e., water from the solvation shell of hydrated water around the head group is removed, which is unfavorable for adsorption).

In systems of cationic surfactant and a negatively charged surface, all these interactions have different loading. The major contribution to the free energy comes from electrostatic and hydrophobic interaction. Electrostatic interaction can be attractive at low surfactant concentration and repulsive at large concentrations—that is, when surfactant overcompensates surface charge. In the latter case, hydrophobic interaction drives adsorption. Previous research has shown that hydrophobic interaction can become dominant over electrostatic interaction: anionic surfactant adsorbs on negatively charged surface when hydrophobic sites are present on the surface.[126]

Adsorption depends on several factors, such as surface hydrophobicity, surface charge, pH, surfactant structure and type, surface preparation, electrolytes, and nature and concentration of counterions.[36] Surfactants adsorb on solid-liquid interfaces in a great variety of structures below the CMC, such as spherical admicelles (adsorbed micelles), rod- and worm-like structures, or cylindrical structures. What kind of structure they form depends on various parameters—for example, geometry of the surfactant, type of surfactant (ionic, nonionic, zwitter-ionic), surface charge, pH, surfactant mixtures, and others.[121, 123, 124, 127–135] Surface aggregates can also be reshaped when transferring, for example, from spheres to cylinders on an increase of concentration.[36, 124]

The adsorption of photoswitchable azobenzene containing surfactants has not yet been well studied. Only an adsorption study of cationic surfactant containing a light-switchable spiropyran group has been conducted by solution depletion method.[33] It was shown that isomerization can lead to adsorption differences as well as a reshaping of surface morphology.

Because azobenzene-containing surfactant solution can have different photostationary states and in order to ensure a clear difference between *trans* and *cis* adsorption, a dark solution was compared to a UV-irradiated solution, in which surfactant was ~100% in the *trans* state or ~90% in the *cis* state, respectively. The solutions were illuminated before the measurements. In the following section, when *cis* adsorption/solution is mentioned, it refers to UV-irradiated solution. Similarly, *trans* adsorption/solution refers to surfactant solution in the dark state. In the following, the CMC always corresponds to the CMC of dark solution (i.e., surfactant in the *trans* state) when not stated otherwise.

Adsorption was measured by a QCM-D that provides time-resolved information on the adsorbed amount and includes information regarding the energy dissipation related to the viscoelasticity of the adsorbed layer. Because QCM-D essentially measures the weight of the adsorbed material, incorporated water in surface structures can lead to an overestimation of adsorption.[134]

7.2 Adsorption isotherms on borosilicate glass

Surfactant concentration for both states (*trans* and *cis*) were varied over a broad

range, between 10^{-4}mM and 10mM. Frequency and dissipation shifts were monitored for successively increasing surfactant concentration. The surface excess was calculated by the Sauerbrey relation.

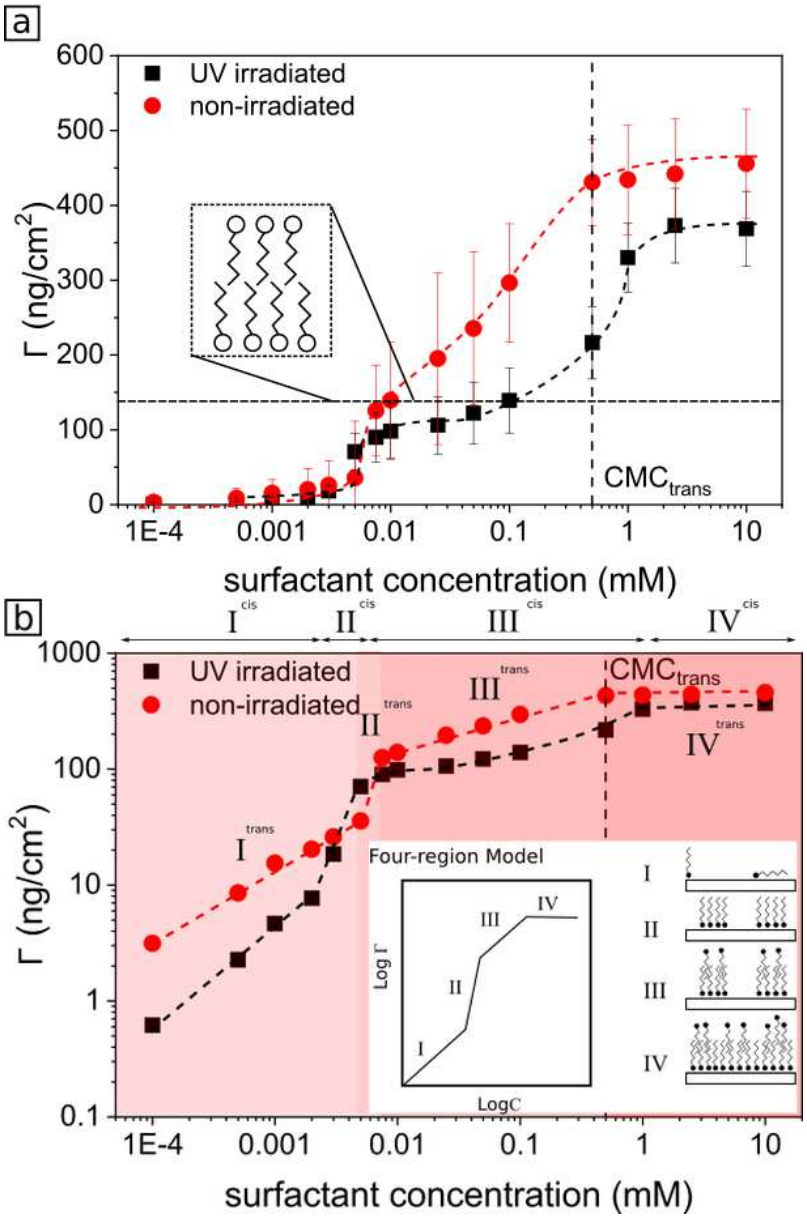

Figure 7.1. (a) Adsorption isotherms show the dependence of the adsorption density Γ as a function of the surfactant concentration (AzoC6) in the *trans* (nonirradiated) and *cis* (UV irradiated) state. The corresponding CMC in *trans* state is 0.5mM (dashed vertical line). The horizontal dashed line marks the adsorbed amount at which a bilayer is formed, schematically shown in the inset. (b) Corresponding adsorption isotherms are shown in a log-log plot. Four phases of adsorption are shown for *trans* in different colors or for *cis* by arrows on top of the plot (I^{cis}, II^{cis}, III^{cis}, IV^{cis}). For clarity, error bars are omitted. Inset: The 4-region model of surfactant adsorption. Adapted from Tyrode et al.[136]

The mass changes are given as a function of the concentration, which is known as adsorption isotherm (**Figure 7.1a**). Adsorption of surfactant in both isomeric states increases slowly at low concentrations, in which adsorption between both isomers is almost similar to *trans* surfactant but adsorbs slightly more. A clear increase is found around 0.003mM. Whereas *trans* adsorption increases almost linear with surfactant concentration with a steep slope, *cis* adsorption follows a more parabolic increase with concentration. The largest difference between adsorption for both states is found at the CMC, at which *trans* adsorption is almost twice as high as *cis* adsorption. For concentrations above the CMC, adsorption saturates only for *trans* surfactant, whereas *cis* surfactant has its steepest increase between 0.5mM and 1mM and reaches a saturation at around 2mM. In the saturated region, the difference in adsorption yields around 80ng/cm^2 with around 450ng/cm^2 for maximal *trans* adsorption and 370ng/cm^2 for maximal *cis* adsorption. Similar adsorption areal densities were found for Cetyltrimethylammonium bromide(CTAB), which were measured by QCM-D on a hydrophilic gold surface with a saturated adsorption of around 500ng/cm^2 at concentrations twice the CMC (1mM).[137, 138] CTAB has the same head group and length compared to the azobenzene containing surfactant lacking only the azobenzene group.

Adsorption of ionic surfactant at the hydrophilic solid-liquid interface has been analyzed for different surfactants and surfaces.[34-36, 120-122, 124, 129-134, 136, 139–144] Most surfactants follow a typical model, either a 2-step model that shows two plateaus in a linear-linear plot or the 4-region model that is plotted in a log-log style. These models are based on certain adsorption characteristics. Below, both adsorption isotherms are compared to the 4-region model, and details about adsorption characteristics are discussed. In **Figure 7.1b** the corresponding log-log plots of the *cis* and *trans* adsorption isotherms are shown. For comparison, a scheme of the 4-region model is given in the inset, with adsorption characteristics for each region.

Comparing the log-log plot of the measured isotherm to the 4-region model, it follows a similar shape—the isotherms reveal the four regions of adsorption.

Region I results from attractive electrostatic interactions between positively charged surfactant head groups and negatively charged surface groups.[129] In this region, adsorption increases faster for *cis* but is higher for *trans.*

In region II, surfactant from the bulk attaches to hydrophobic sites on already attached surfactant. These attached molecules act as anchor molecules. Surfactant molecules adsorb onto hydrophilic silica with a head-to-surface orientation. With head down and tail up, the aggregates formed on the surface are called hemi-micelles. These surface aggregates create hydrophobic patches on the surface. In this regime, lateral hydrophobic interaction and electrostatic attraction drive surfactant adsorption. At the end of region II, surface charge is compensated, and adsorption works against electrostatic repulsion. Therefore, the increase of adsorption is lowered.

In region III, surfactant from the bulk adsorbs mostly by hydrophobic interaction on the already adsorbed surfactant layer. Surfactant in *trans* state adsorbs more efficiently with a linear increase until saturation.

In Region IV, the surface is saturated with surface aggregates, such as hemi-micelles, bilayers, or other structures.

Cis adsorption reaches a saturation at around four times the CMC of *trans* solution. Adsorption effectiveness (i.e., the maximum concentration at the surface at saturation) is larger for surfactant in *trans* state than in the *cis* state.

The adsorption isotherms differ mostly in region III of the 4-region model. In the log-log plot, *trans* adsorption increases linearly with bulk concentration. This is in contrast to *cis* adsorption, which shows a more parabolic increase. In region III, adsorption is primarily driven by hydrophobic interaction. Since surface charge is compensated at the end of region II, further adsorption has to overcome electrostatic repulsion. Due to the higher hydrophobicity of *trans* surfactant, the molecules attach much better compared to *cis* surfactant, which tends to stay in the bulk due to its larger polarity. Only when bulk concentration reaches the CMC, does a larger increase in *cis* adsorption occur, thus overcoming the slope of *trans* surfactant. The largest differences in adsorption between *trans* and *cis* are found between 0.1 and 1mM. In this range, particle velocity in LDDO increases with a much steeper increase at the CMC, which is where *cis* adsorption strongly increases and *trans* adsorption remains constant. Above the CMC, *cis* and *trans* adsorption remains constant, but LDDO only slightly decreases.

Compared to surfactant in *trans* state, the mutual interaction between *cis* isomers is less favorable due to steric hindrances and less hydrophobicity, which is why

they are less likely to aggregate. Therefore, the interaction between surfactant molecules is too weak to overcome electrostatic repulsion at the onset of the third region. It is difficult to determine the onset of region III for *cis* solution. It is the concentration at which hemi-micellization starts. One could argue that after the rapid increase in region II, a plateau is reached in which surfactant can barely adsorb. Thereafter, region III would commence around the CMC at which the adsorption has its steepest increase. From these results, it is unclear at which concentration hemi-micellization starts. However, surfactant adsorption rises (albeit slowly) between 0.01mM and 0.5mM.

It should be emphasized that 10% of the surfactant is still in the *trans* state. That 10% could contribute to the pronounced adsorption increase. That would mean that *trans* surfactant triggers adsorption by hydrophobic interaction and stacking. However, a clear differentiation of the contributions of either surfactant is impossible because a fully 100% *cis* solution or interpolation by investigation of solutions with different fractions of *cis* content, such as 30%, 50%, 70%, 90%, would be required.

Adsorption of surfactant in the *trans* state can be explained by the 4-region model which provides valuable information about the driving mechanisms that depend on the concentration. Adsorption of *cis* surfactant differs from the typical 4-region model in the range of region III, where there is no linear increase in the adsorbed amount. It is unclear at which concentration hemi-micellization starts. Because of both isomers present in solution, it could be useful to consider the solution as a mixture of two surfactants with each contributing differently to adsorption. Regarding LDDO, the differences in the adsorbed amount of *trans* and *cis* isomers at fixed surfactant concentration can be interpreted as a desorption of surfactant molecules in the illuminated area. It should be noted that adsorption isotherms only refer to equilibrium adsorption.

7.3 Adsorption isotherms on a hydrophobic substrate

Adsorption isotherms for *trans* and *cis* solution were obtained from equilibrium adsorption of surfactant moleculeson a gold sensor covered with Teflon AF1600 (**Figure 7.2**). The 4-region model proved to be helpful in interpreting the results obtained in **Section 7.2**. Therefore, the isotherms were analyzed with respect to this

model.

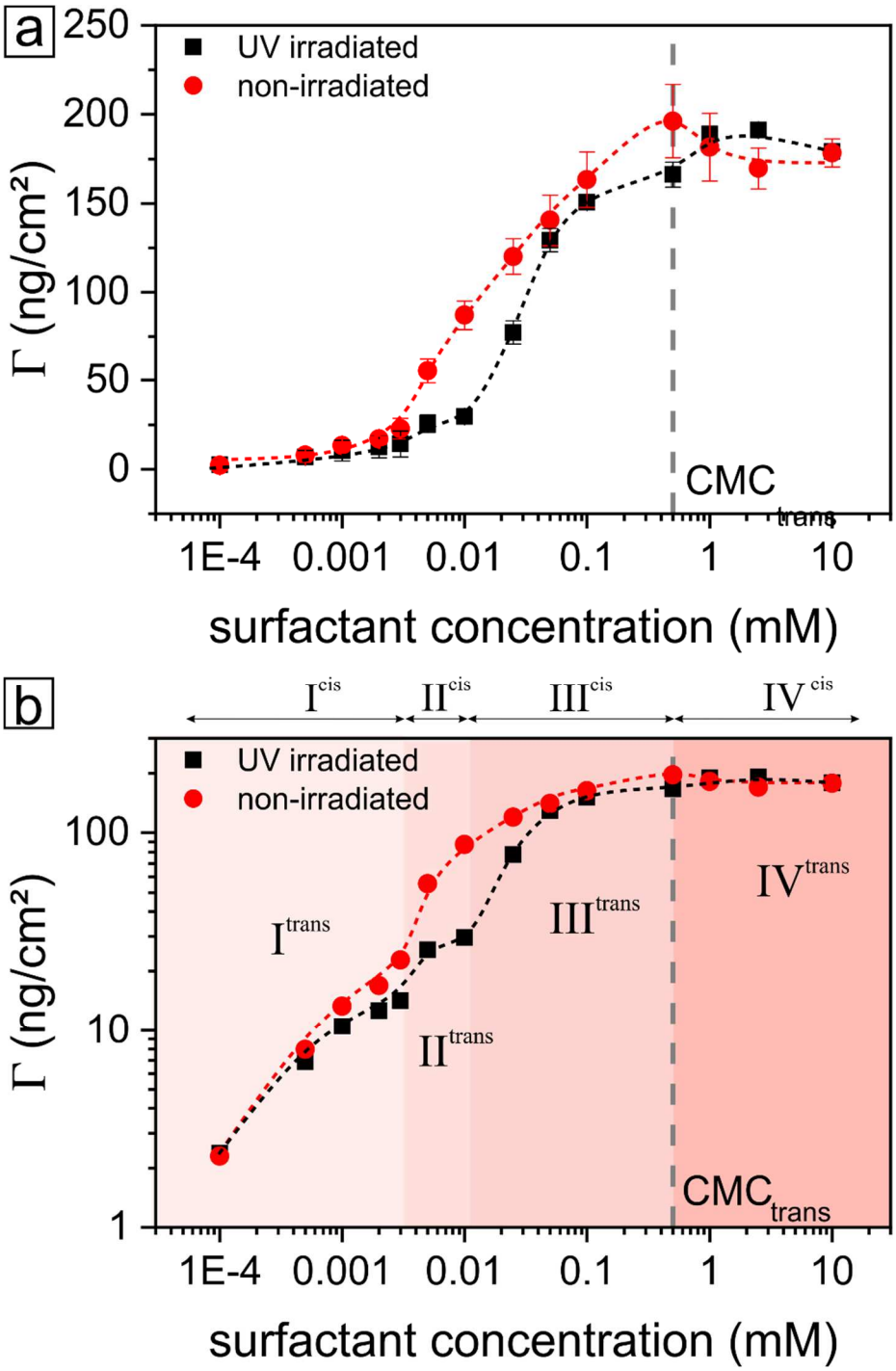

Figure 7.2. (a) Adsorption isotherms show the dependence of the adsorption density Γ as a function of the surfactant concentration (AzoC6) in the *trans* (nonirradiated) and *cis* (UV irradiated) states on a hydrophobic surface (covered with Teflon AF 1600). The corresponding critical micelle concentration (CMC) in *trans* state is at 0.5mM (dashed vertical line). (b) Corresponding adsorption isotherms are shown in a log-log plot. Four phases of adsorption are shown for *trans* in different colors or for *cis* by arrows on top of the plot (I^{cis}, II^{cis}, III^{cis}, IV^{cis}). For clarity, error bars are omitted.

Trans adsorption follows the pattern of a typical 4-region model up to the CMC. The adsorption at low surfactant concentration is mainly driven by electrostatic interactions and shows a linear dependence up to 0.002mM reaching region II, at which a steep increase is the result of mutual hydrophobic interaction. Region III starts at roughly 0.01mM with a linear increase in adsorption, at which electrostatic surface charge is compensated and adsorption is mainly driven by hydrophobic interactions. [†] Region IV, however, differs from the model. Instead of reaching a saturation at the CMC, adsorption decreases at first, reaching a saturation at 4mM.

The adsorption isotherm of *cis* solution follows a sigmoidal shape in the linear-log plot but shows a more distinct deviation in the low concentration range. It differs from the 4-region model at some points. In region I, the slope levels off diverging from a linear relation. The second region is difficult to assign but seems to coincide with the onset found in *trans* solution. In contrast to the *trans* state, a short second plateau follows the steep increase in region II. This plateau could be assigned to the third region, in which the surface charge is compensated. However, what follows after the plateau is a further steep increase, at which the adsorbed amount increases until saturation is reached around 1mM.

Comparing both isotherms, they mostly deviate in the concentration range between 0.002mM and 0.05mM. It is interesting that the increase in region II is shown for both solutions at the same concentration (i.e., at 0.003mM). Whereas *trans* adsorbs better over a larger concentration range, *cis* appears to adsorb in a small plateau before a pronounced enhancement drives adsorption to comparable values at 0.05mM. Stronger deviations appear above the CMC. Whereas *cis* solution takes the usual route to saturation, which is reached around 1mM, *trans* adsorption decreases before reaching saturation with matching adsorption for both solutions around 10mM.

Adsorption increases in *cis* solution can be explained by contributions of residual *trans* surfactant because 10% of *trans* isomers are present in *cis*-enriched solution. Adsorption of *cis* surfactant largely differs between regions II and III, with a

---

[†]Due to the auto-dissociation of water into OH^- and H_3O^+ ions Teflon AF 1600 charges negatively in water solution with a measured zeta potential of -60mV.[158]

small plateau in region II. The small plateau indicates a decrease in adsorption because of charge compensation. The following steep increase could be accounted to surfactants in the *trans* state that reach a critical concentration at which mutual interaction between *trans* surfactant becomes measurable. The increase after the short plateau appears around 5 to 10 times the concentration, at which *trans* solution turns into region II. Assuming 10% of surfactant in the *trans* state is present in solution, this could explain the second increase.

The adsorption isotherms in **Figure 7.2a** demonstrate the differences between *trans* and *cis* solutions. Compared to adsorption of pure *trans* solution, in the *cis* solution the steep increase related to region II of the 4-region model appeared at a ten times larger concentration. This suggests that the hemi-micelle concentration (i.e., onset of formation of aggregates) shifts to larger concentration. This seems reasonable because surfactant in *cis* state is more hydrophilic and because the kinked shape retards aggregation.

7.4 Comparison of adsorption isotherms between hydrophilic and hydrophobic substrates

Comparing adsorption isotherms between hydrophilic and hydrophobic surface isotherms for *trans* and *cis* isomers shows striking differences (

Figure 7.3). At first, adsorption effectiveness (i.e., adsorption at saturation) for the hydrophobic surface is smaller than on the glass surface. In detail, the difference between hydrophilic and hydrophobic surfaces is about four times smaller for *trans* isomers and around three times smaller for *cis* isomers. These results can be compared to those obtained with conventional surfactant of similar hydrophobicity. For example, similar adsorbed amounts of surfactant has been found previously for adsorption of CTAB (cetyltrimethylammonium bromide) [‡] On a hydrophilic gold surface CTAB adsorbs with a mass of ~500ng/cm^2 and on a hydrophobic surface surface, i.e., on a

[‡] CTAB has a similar length like AzoC6 with 16 CH2 groups. When one phenyl rings are considered as effective as 3.5 CH_2 groups the tail has a length of 17 CH2 groups. Both have the same head group. Therefore, surface activity can be very similar to the *trans* form of AzoC6.

gold surface modified with C18 (n-octadecyltrichlorosilane) CTAB adsorbs with a mass of ~140ng/cm^2 .[137] Furthermore, region II and region III differ in concentration range and steepness. Whereas on the glass surface, region II is very narrow and region III wider, region II on the hydrophobized surface spans over a much larger concentration range. In region II, roughly 80ng/cm^2 are adsorbed, which is comparable to the amount adsorbed on glass surfaces until surface charge is compensated, indicating the end of region II. This suggests that adsorption efficiency (i.e., the amount adsorbed at a specific bulk concentration) is worse than on the glass substrate, which also holds true for region III. Markedly, adsorption efficiency is lowered in region III much more on the hydrophobic surface than the hydrophilic one.

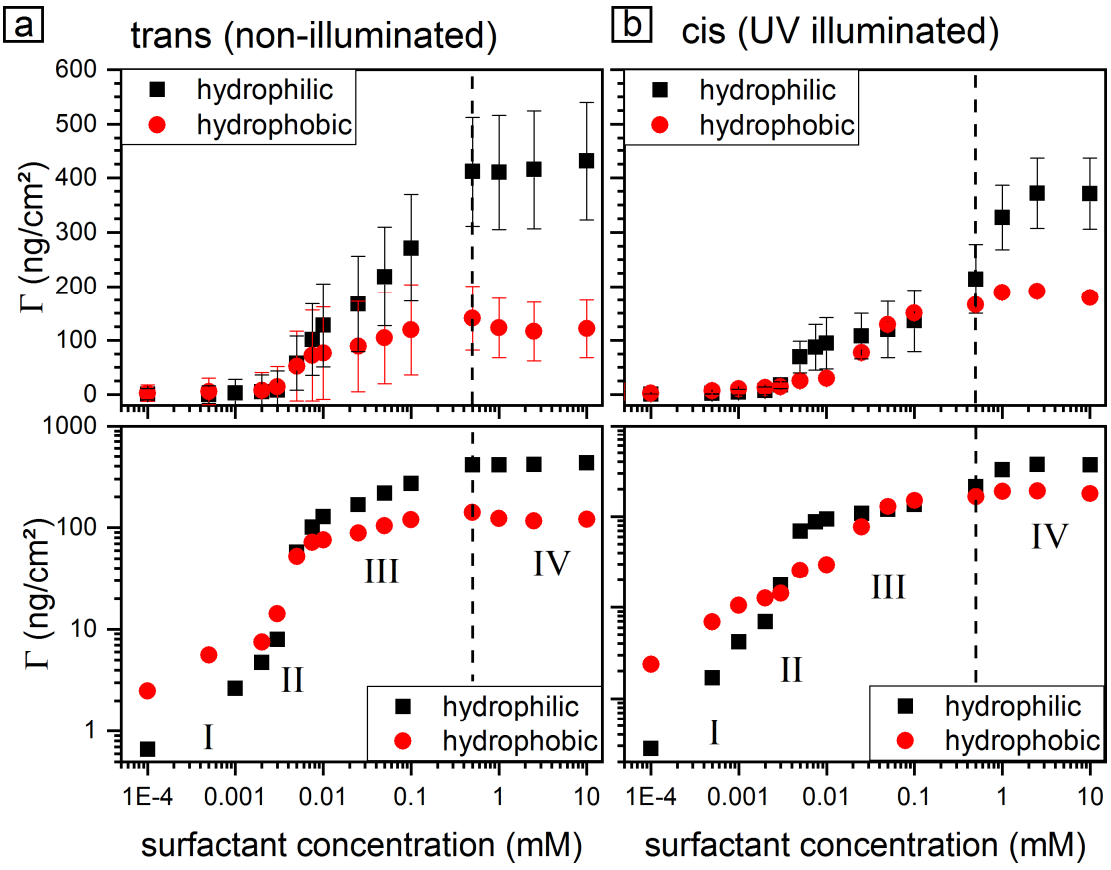

Figure 7.3. Adsorption isotherms measured on hydrophilic borosilicate glass and hydrophobic Teflon AF1600 obtained from QCM-D measurements for azobenzene surfactant (AzoC6) of (a) *trans* and (b) *cis* solution in a lin-log (top) and log-log plot (below). The CMC of *trans* is marked by a dashed line. For clarity, error bars are omitted in the log-log plot. The roman numerals mark the four regions from the 4-region model as shown in **Figure 7.1**.

On a hydrophobic substrate, surfactant molecules prefer to align with their tails toward the surface and heads toward the solution.[135, 137, 145, 146] This contrasts with the adsorption on a hydrophilic surface, which has a reversed orientation: head toward surface, tail toward solution.[36, 124, 136, 137] Thus, on a hydrophilic surface, an adsorbed surfactant layer points its tail toward the solution, thus providing anchor points for surfactant molecules diffusing to the surface. They can interact with hydrophobic tail to hydrophobic tail, building a double layer. In contrast to adsorption on a hydrophobic surface on which the molecules point their charged heads toward the solution. This orientation prevents further adsorption due to electrostatic repulsion. As surfactant in the *cis* state shows almost the same amount of adsorption, this explanation seems reasonable because this isomer adsorbs much less by hydrophobic interaction due to its larger hydrophilicity and kinked geometry.

A decrease at saturation above the CMC, as measured for surfactant in the *trans* state, has been observed by Duan et al. for an anionic surfactant, namely sodium dodecyl sulfate (SDS) on a surface hydrophobized with C18.[147] They ascribed this phenomenon to the formation of micelles in solution, which is more favorable than micellization on the surface just above the CMC. Others have ascribed this to coadsorbed organic impurities, which desorb at concentrations larger than the CMC.[148] Because impurities were not found in solution of *trans* surfactant or in *cis* adsorption on the glass surface this explanation was ruled out.

In summary, both isomers adsorb on glass and Teflon surfaces differently. Adsorption effectiveness and efficiency are better on the glass surface than on the hydrophobic surface. On the glass surface, *cis* molecules adsorb much less than *trans* molecules. In contrast to the hydrophobic surface, at which (at least in the concentration range of LDDO between $c_{surf} > 0.5$mM), adsorption for both isomers yielded similar values with small differences within the error range.

The difference in the adsorption of *trans* and *cis* isomers on hydrophobic and hydrophilic surfaces causes different directions of LDDO flow, as discussed in **Chapter 6.2**. On Teflon, the small difference between adsorption of *trans* and *cis* isomers could explain the inward LDDO flow, when $\Gamma_{tot,cis} > \Gamma_{tot,trans}$, and the outward flow, when $\Gamma_{tot,cis} < \Gamma_{tot,trans}$ (**Equation** (**22**) in **Chapter 4**). But the flow direction does not only depend on overall adsorption but on the relative gradient of

adsorption of *trans* and *cis* surfactant with concentration: $\frac{\partial \Gamma_{tot,cis}}{c_{cis}}$ and $\frac{\partial \Gamma_{tot,trans}}{c_{trans}}$. In the case of the glass surface both have equal signs, and $\Gamma_{tot,cis} < \Gamma_{tot,trans}$; therefore, we have an outward LDDO flow. On the hydrophobic surface, $\frac{\partial \Gamma_{tot,trans}}{c_{trans}}$ becomes negative above the CMC. This decrease above the CMC could invert the flow, and, indeed, this takes place but depends on the distance from the laser spot (**Figure 6.2** in **Chapter 6.2**). A further increase of concentration to 2mM resulted solely in an outward flow.

The unusual adsorption decrease of *trans* surfactant goes into a saturation, at which adsorption remains largely constant. The complex flow pattern discussed in **Chapter 6.2** (**Figure 6.2**) seems to result from this unusual decrease in adsorption, which could be seen as a transition phase in which the inward flow below the CMC turns into an outward flow above the CMC. This difference appears between 0.5mM and 2mM. A view on the adsorption isotherms shows that this range is between the saturation of *trans* surfactant and *cis* surfactants because *trans* surfactant micelles appear at 0.5mM. At 2mM, however, the CMC of the UV-illuminated solution could be reached. In this range, the maximum concentration gradient should be found because above the CMC of the UV-illuminated solution, a destruction of *trans* micelles follows a construction of *cis* (most probably combined with *trans*) micelles. As a result, monomer species increase from 0.5mM in *trans* to 2mM in *cis* under UV irradiation.

Definite conclusions about the complex motion on hydrophobic surfaces cannot be drawn from adsorption isotherms because LDDO experiments are typically conducted under more complicated conditions (i.e., in-situ local laser irradiation, which cannot be modeled by QCM-D measurements). Nevertheless, these results give indications about inward and outward motion under irradiation. Whereas on the glass slide, UV irradiation should lead to a desorption of surfactant, on a hydrophobic surface, illumination can lead to adsorption and desorption because of similar adsorption of *trans* and *cis* isomers. This suggests that inward and outward flows are possible, which, indeed, was observed. Better insights into adsorption could be gained with in-situ adsorption experiments combined with analysis of adsorption kinetics.

7.5 Adsorption kinetics on borosilicate substrate

Adsorption isotherms show the equilibrium adsorption obtained from QCM kinetics measurements in which time-dependent frequency shift and energy dissipation are monitored. **Figure 7.4** shows an example of frequency and dissipation shifts for *trans* and *cis* surfactants with an initial baseline measured in milliQ water. Surfactant solution was injected stepwise, starting with the lowest concentration of $1x10^{-5}$mM. In the low concentration range, the frequency shifts barely exceed the frequency noise. The frequency drops distinctly at first for *trans* adsorption at $c_7 = 7.5x10^{-3}$mM and for *cis* adsorption at $c_6 = 5x10^{-3}$mM. Each following concentration increase enhances the frequency shift in a step-like manner. Below, the discussion is focused on the adsorption speed and the dissipation factor for *trans* and *cis* solution, showing *trans* adsorption first and then *cis* adsorption for comparison.

After each injection of *trans*-solution, the frequency drops quickly within one minute, followed by only small changes around 1Hz until frequency equilibration occurs within several minutes. A distinct and fast drop is found after an injection of 0.5mM (CMC_{trans}, c_{12} in **Figure 7.4a**), with a shift of ~7Hz. A further increase in concentration leads only to minor changes in frequency of not more than 1.5Hz. To analyze adsorption rates, the frequency drop is fitted by an exponential function. The fits (not shown) yield decay times between 25s and 1 minute. However, for some concentrations, for example, at 0.5mM, a biexponential function yields more accurate fits with fast decay times below one minute and a longer decay time of more than 10 minutes.

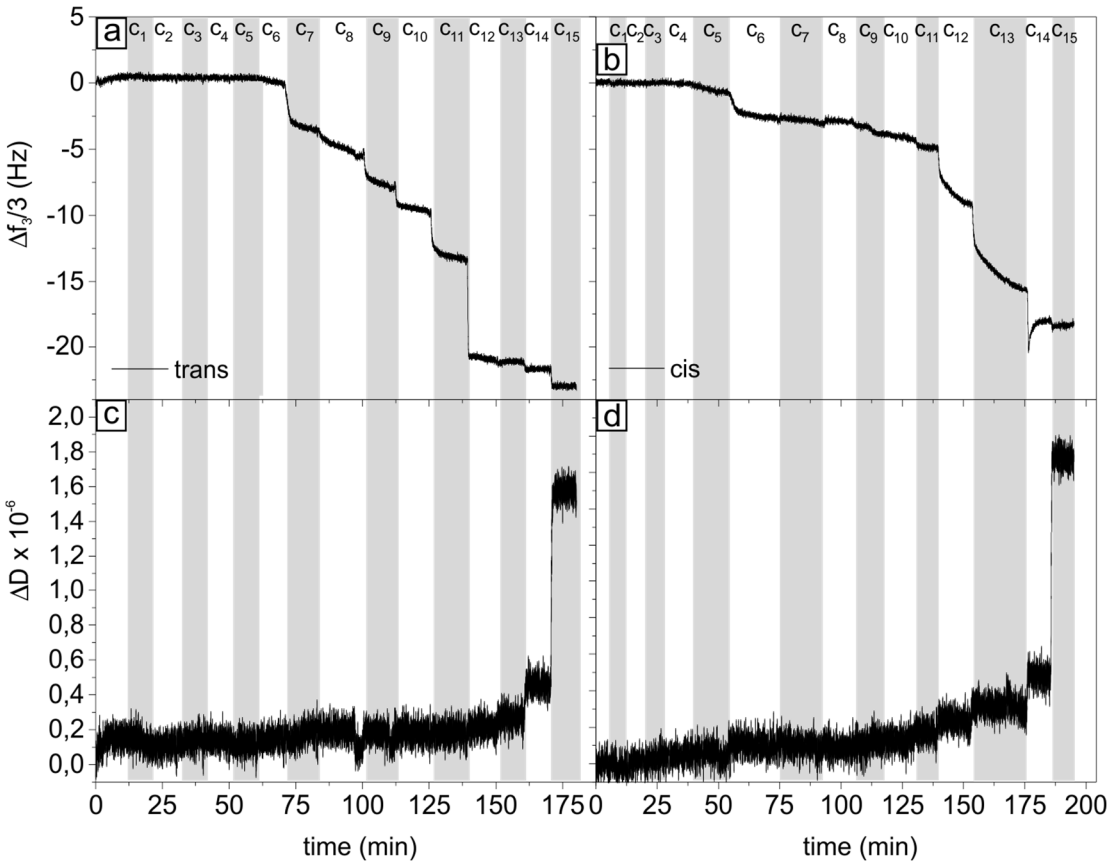

Figure 7.4. Frequency change (top) and dissipation change (bottom) as a function of time directly monitored by QCM-D at sequential increase of azobenzene containing surfactant concentration for surfactant in the *trans* (a) and (b) *cis* state on a borosilicate glass surface. Each sequential concentration step is marked. Surfactant concentrations from c_1 to c_{15} were used in the following steps with concentrations given in mM: $c_1 = 1x10^{-4}$, $c_2 = 5x10^{-4}$, $c_3 = 1x10^{-3}$, $c_4 = 2x10^{-3}$, $c_5 = 3x10^{-3}$, $c_6 = 5x10^{-3}$, $c_7 = 7.5x10^{-3}$, $c_8 = 0.01$, $c_9 = 0.025$, $c_{10} = 0.05$, $c_{11} = 0.1$, $c_{12} = 0.5$ (CMC_{trans}, patterned background), $c_{13} = 1$, $c_{14} = 2.5$, $c_{15} = 10$.

In the case of the dissipation factor describing the energy dissipated over the energy stored in the layer, most information is lost due to strong noise. However, one can see that the dissipation factor increases markedly at concentrations above the CMC, with the largest increase in D at 10mM and a shift from around 0.5 to 1.6 (**Figure 7.4c**).

Adsorption of *cis isomer*s differs slightly from the kinetics of the *trans* isomer (**Figure 7.4b**). Below the CMC, frequency shifts are small, typically below 1Hz. At the CMC, the frequency drops quickly at first, followed by a slow decrease. The frequency drops in the first 30s to around 3Hz and then declines at a lower adsorption rate reaching equilibrium after more than 20 minutes. During this slow adsorption, the frequency

declines around 2Hz. A biexponential fit of the frequency shifts yields decay times of 30s for the fast drop and around 450s for the slow decline. The latter time is similar to decay times at concentrations below the CMC. At a 1mM concentration, the adsorption behavior shows a similar shape but is more pronounced. During the first 30s, a fast adsorption is indicated by frequency drops of ~3Hz which are followed by a slow decline of about 3Hz in more than 20min. A further increase in concentration to 2.5mM contrasts with the kinetics described before. A steep drop is followed by a slow rise in frequency (**Figure 7.4b**).

Energy dissipation is similar to what occurs with a *trans* solution. Most noise covers the signal at low concentrations. However, a stepwise increase appears from 0.05mM, with increasing concentration. Similar to *trans* solution, the dissipation shifts markedly for 2.5mM and 10mM to values of 0.5 and 1.8, respectively (**Figure 7.4d**).

The adsorption kinetics for both *cis* and *trans* solutions can be fitted by either exponential or biexponential decay. For *trans* solution, the biexponential decay fits best below the CMC, whereas it is true for *cis* solution above the CMC. Decay times yield values of less than a minute for the fast adsorption and can be much longer (sometimes more than 20min.) for the slow adsorption, especially for solution primarily in *cis* state. The fast process might be a response of the sudden increase in concentration and concomitant adsorption, whereas the slow process stems from occupation of inhomogeneous adsorption sites on the surface or the reorganization of already adsorbed surfactant. This was proposed in a study involving adsorption of cationic surfactant on a silica surface, in which a theoretical two-step model was developed for systems with similar timescales for mass transport and adsorption.[144] Different behavior was found at 2.5mM for *cis* isomers, with a fast frequency drop followed by a slow exponential increase of the frequency. The reason for such a behavior is not yet clear. The fast adsorption can likely be ascribed to direct adsorption of micelles followed by a reorganization of surface structures. This mechanism was proposed for adsorption of vesicles onto a silica surface showing vesicle rupturing followed by bilayer formation.[149–151] During adsorption and formation of the lipid bilayer, the dissipation factor rises, followed by a decrease after completion of the bilayer formation. While the drop and subsequent increase in frequency are similar (**Figure 7.4d**), the dissipation factor rises but remains constant, without a drop that would

indicate that reorganization has finished. Another contribution could arise from the release of either water entrapped in micelles or hydrated surface water after adsorption. Because QCM-D detects the total mass of the adsorbed layer, including incorporated water, the measurements can overestimate adsorption. A rupture of micelles could release entrapped water, which is reflected in a frequency increase.

The micelle shape and size of *cis* isomers should be different than micelles only composed of *trans* molecules because of different size, shape, polarity, and lower hydrophobicity. In UV-illuminated solution, the residual *trans* surfactant is considered to be incorporated into micelles. Whereas surfactant in *trans* state favors stacking, which can be seen in UV-vis spectra as hypsochromic shift[§] of the adsorption peak above the CMC, surfactant in *cis* state has difficulties stacking because of geometry restrictions. Therefore, the adsorption kinetics of two isomers should be significantly different

The micelle shape can be estimated using the molecular or critical packing parameter (CPP) that takes into account the volume of the hydrocarbon chain *V*, the area of the polar head *A*, and the length of the hydrocarbon tail *L*:

$$CPP = \frac{V}{AL} \tag{32}$$

When the CPP is below 0.3, spherical micelles can be expected. Above 0.3 nonspherical micelles will form.[152] Recently, this parameter was estimated for various surfactant such as AzoC6.[168] It was found that *trans* isomers have a CPP of 0.17,[**] whereas *cis* isomers have a CPP between 0.27 and 0.29 depending on how the length is calculated. The CPP for the *cis* isomer is close to the critical point at which the spherical structure is unfavorable. This parameter illustrates that surface structures can largely change from *trans* to *cis.*

As surfactant adsorption increases monolayers, bilayers and other kinds of hemicelles or admicelles (adsorbed micelles) can be formed. Somasundaran termed the

[§] A hypsochromic shift is accounted to π-π stacking of the azobenzene group shifting the adsorption maximum to lower wavelengths.

[**] $A_{\text{trans}} = A_{cis} = 100\text{Å}^2$, $V_{trans} = 364\text{Å}^3$, $V_{cis} = 367\text{Å}^3$, $L_{trans} = 21.96\text{Å}, L_{cis} = 13.59\text{Å}\backslash 12.43\text{Å}$

surface aggregates solloids.[153] At concentrations above the CMC, surfactant adsorption increases slightly; however, solloids can change their structure.[124] In both surfactant solutions, dissipation increases weakly in the concentrations below 2.5mM.[††] The increase of the dissipation factor at concentrations above 10mM could be due to the following reasons: The damping of the liquid oscillation depends on the viscosity and the density of the solution increasing with surfactant concentration. However, a discussion of the dissipation factor is difficult because many factors contribute to dissipation such as the properties and interrelationships between molecule, solvent, and surface.[154] For example, dissipation can increase when ionic heads trap water molecules or when hydrophobic tails of anionic sodium laureth sulfate monomers adsorbs onto a hydrophobic polymer surface.[155]

7.6 Adsorption kinetics on a hydrophobic substrate

Figure 7.5 shows adsorption kinetics at concomitant increases of surfactant concentration of *trans* and *cis* surfactant on the hydrophobic surface coated with Teflon AF1600. Adsorption kinetics on the Teflon-coated surface show longer adsorption times (compared to glass adsorption) of between 60s and more than 5 minutes depending on the injected concentration. The largest difference between both substrate types regarding kinetics is found above the CMC (compare **Figure 7.4** and **Figure 7.5**). At 0.5mM, the frequency drops, followed by a slow increase. Further injection of larger concentrations leads to very small decreases in frequency in ranges less than 0.1 Hz (not shown in **Figure 7.5**). An exception is found at 10mM, at which a more pronounced decrease is found—equally followed, however, by an increase in frequency. This is similar to the results observed on a glass surface in *cis* dominated solution. Similar kinetics can be found for *cis* solution on the hydrophobic substrate (**Figure 7.5b**). A small drop followed by a slow increase in this case is observed at 2.5mM. In such a case, the frequency drops within 5 seconds of adsorption followed by an almost linear increase in frequency, with a slope of 0.24Hz/s.

Dissipation increases slowly for *trans* solution with a peak at 0.5mM at which

[††] At 2.5mM micelles are present in surfactant solution for both isomers. Surface tension measurements showed a CMC for cis solution at ~4mM, however, the adsorption isotherm shows a saturation already at 2mM indicating the CMC of the solution.

frequency drops and rises slowly again. The maximum is found at 10mM, with similar values compared to the glass slide to be $\Delta D = 1.5$ppm. Dissipation for *cis* solution remains constant with a pronounced increase to roughly 0.4ppm at 0.05mM. An increase in concentration results in slow increases except at 2.5mM, at which a peak follows a decrease in dissipation, similar to that increase found for *trans* solution at 0.5mM.

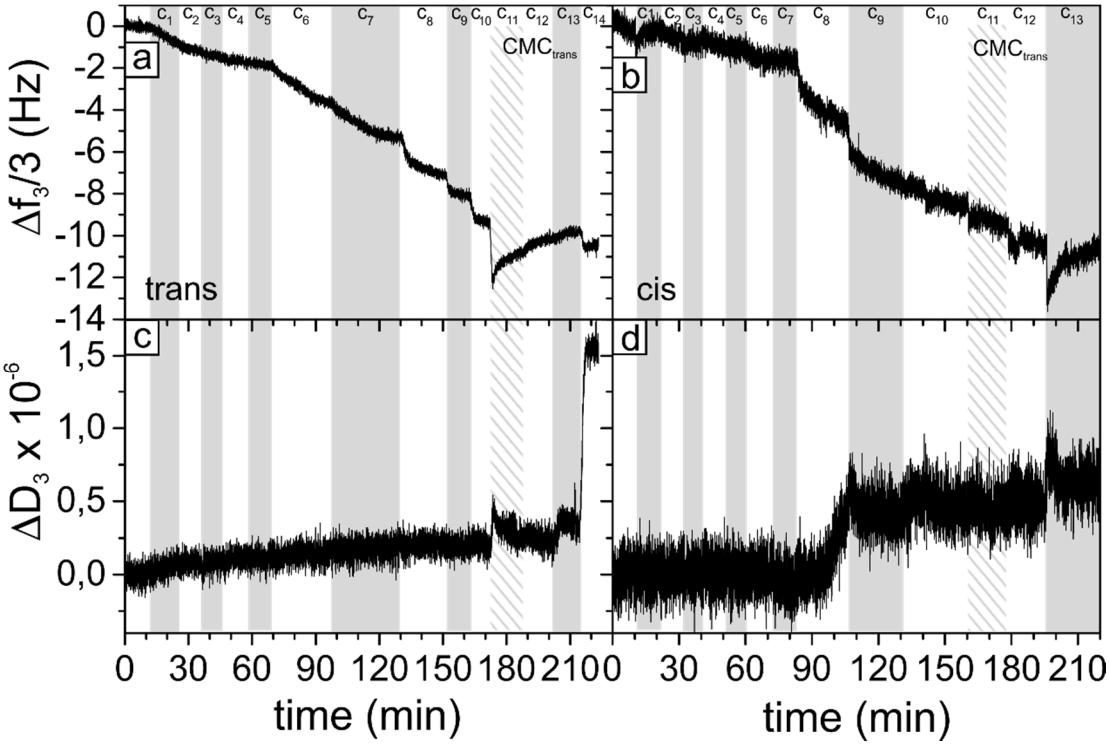

Figure 7.5. Frequency change and dissipation change at the hydrophobic surface as a function of time directly monitored by QCM-D at sequential increase of azobenzene containing surfactant concentration for surfactant in (a) *trans* state and (b) *cis* state. Each sequential concentration step is marked. Surfactant concentrations from c_1 to c_{15} were used in the following steps with concentrations given in mM: $c_1 = 1x10^{-4}$, $c_2 = 5x10^{-4}$, $c_3 = 1x10^{-3}$, $c_4 = 2x10^{-3}$, $c_5 = 3x10^{-3}$, $c_6 = 5x10^{-3}$, $c_7 = 0.01$, $c_8 = 0.025$, $c_9 = 0.05$, $c_{10} = 0.1$, $c_{11} = 0.5$ (CMC_{trans}, patterned area), $c_{12} = 1$, $c_{13} = 2.5$, $c_{14} = 10$.

Adsorption happens more quickly for *trans* surfactant on a glass surface than on a Teflon coated surface. Whereas on glass, this behavior of a frequency drop is followed by a slow increase found only for *cis* solution at 2.5mM, a similar drop was found for concentrations above the CMC for *trans* and *cis* solutions on a hydrophobic surface. For *trans* solution, this appears markedly at the CMC (c_{11} in **Figure 7.5a**) and with increasing concentration. Previously, this behavior has been explained by the

adsorption of micelles, which rupture and then reorganize on the surface, as has been found in previous studies on vesicle adsorption.[149–151] The release of bound water could be the reason for the increase in frequency. Compared to the glass surface, dissipation first increases and then decreases again, which has also been reported in the mentioned studies. This explanation seems to be reasonable because this happens at the CMC. This confirms that micelle adsorption followed by reorganization is responsible for this behavior. This is found for both solutions on the Teflon-coated surface, whereas this appears only for *cis* solution on glass.

On the glass surface, adsorption of *trans* isomers does not lead to this behavior. As *cis* adsorbs to the surface, it could occupy a larger area per molecule. Because of its kinked geometry, attachment efficiencies should be decreased. Therefore, attachment of micelles could lead to the rupture of micelles combined with an exchange of surfactant molecules, favoring the more hydrophobic *trans* molecules present in *cis* solution. *Trans* solution does not lead to reorganization on a glass surface because a fully formed bilayer inhibits micelle attachment. On the hydrophobic substrate, however, the surface structures adopt a different state, in which adsorption of micelles is possible and leads to molecular rearrangements on the surface. This happens for *trans* and for *cis* molecules.

7.7 Surface zeta potential

QCM-D measurements revealed differences in total adsorption of surfactant in *trans* and *cis* state. In addition to these measurements, surface zeta potential measurements (SZP) of a solid glass substrate were carried out in surfactant solution of different concentrations to gain more insight into the electrostatic characteristics of the surface with adsorbed surfactant. With SZP, one can determine the adsorption of surfactant and counterions in the Stern layer (i.e., the directly adsorbed surface molecules).[156, 157] The SZP was measured at the shear plane near the interface between the Stern and the diffuse layer of the EDL. Because salt diminishes the motion under LDDO (**Chapter 5.1**), measurements were conducted in pure water. Since the SZP is related to the surface potential ϕ_0, it is considered in **Equation** (**23**) and (**31**) (**Chapter 4**). Below, a dark solution is referred to as *trans* zeta potential and a UV-illuminated solution as *cis* zeta potential.

The SZP was measured for a series of concentrations of *trans* and *cis* solutions (**Figure 7.6**). In both cases, the SZP follows a sigmoidal shape with some differences. At concentrations below 0.01mM, the slopes are similar within the experimental error. Around 0.01mM, *trans* solution shows a large jump from negative to positive (i.e., from -5mV to 20mV) followed by a saturation and a slow increase up to the CMC. A similar but less pronounced increase in zeta potential is measured for *cis* solution: the zeta potential increases from around -10mV up to 15mV between 0.01mM and 0.1mM. It then remains constant at further concentration increases. In summary, the zeta potential for *trans* surfactant is larger than for *cis* surfactant, with around 30mV for *trans* and 20mV for *cis*.

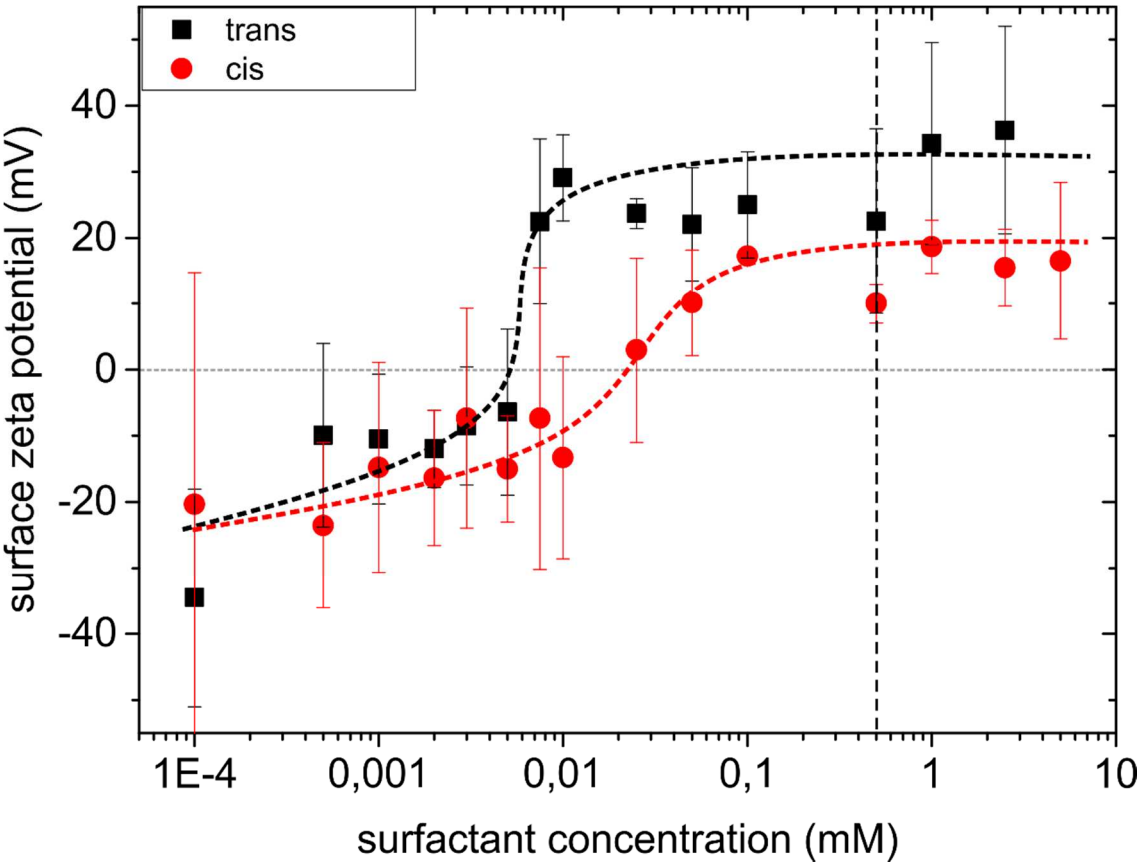

Figure 7.6: Surface zeta potential as a function of surfactant concentration (AzoC6) of *trans* (squares) and *cis* (circles) state. The vertical dashed line marks the CMC of *trans* solution.

The glass surface in pure water bears a negative charge due to dissociation of surface groups, such as silanol, that are mainly present on Borosilicate glass surfaces. In pure water, the zeta potential yields –(50±10)mV. At low concentrations (i.e., when the zeta potential is negative), surfactant adsorption leads to an increase of the SZP. At the IEP, the charge of the adsorbed surfactant compensates for the surface charge and results in an SZP of 0mV. Further surfactant adsorption leads to an overcompensation of the surface charge and renders the surface positive. At this point, electrostatic interaction turns against adsorption. As a result, the driving force is the hydrophobic interaction between surfactant molecules that are already adsorbed and surfactant monomers in solution.

The IEP differs for *trans* and *cis* surfactant. Whereas it appears already below 0.01mM (~0.006mM) for *trans* surfactant, the IEP is at 0.03mM for *cis* surfactant. The concentration at which the saturation takes place for *cis* isomers is 10 times larger than for trans isomers to be around $c_{trans}^{saturation}$ = 0.01mM and $c_{cis}^{saturation}$ = 0.1mM. The differences can be due to the stronger mutual interaction between *trans* molecules, which facilitates adsorption of surfactant (cooperative binding). At the saturation of the SZP, further increase of bulk surfactant concentration does not lead to an increase in SZP. However, QCM-D measurements show saturation at a much larger concentration with deviations for the isomers (i.e., c_{trans}=0.5mM) and a five times larger concentration c_{cis}=2.5mM (**Figure 7.1**). Because SZP measurements only take molecules inside the Stern layer into account, a saturation indicates a full coverage of the surface with surfactant molecules. This means that *trans* isomers form a monolayer at 0.01mM, while *cis* isomers form a monolayer at 0.1mM. Further surfactant is expected to adsorb in the mobile diffuse layer that is sheared off at measurements and, therefore, does not contribute to the zeta potential. For *trans* and *cis* solution, the adsorbed amount of surfactant at the IEP are similar, around 100ng/cm^2. However, the IEP is found for *trans* solution at lower surfactant concentrations (~0.006mM). The saturation of the zeta potential for both isomers appears at around 140ng/cm^2 adsorbed surfactant (see **Figure 7.1** at c_{cis}=0.1mM and c_{trans}=0.01mM).

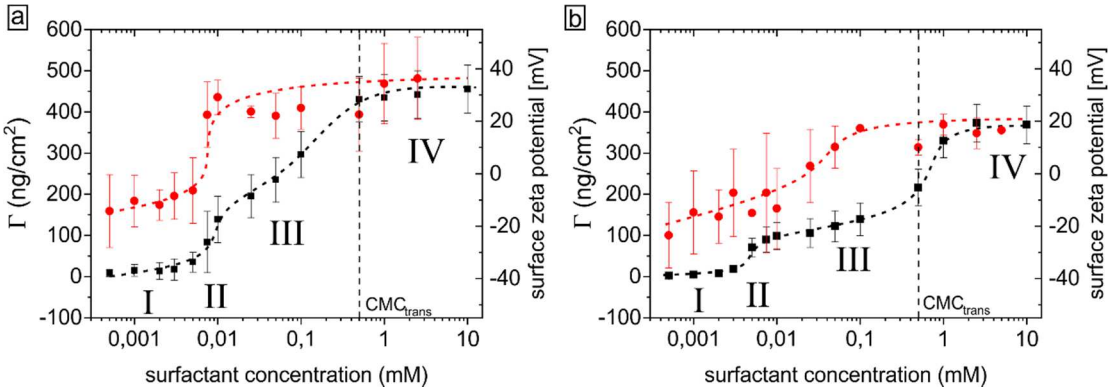

Figure 7.7. Comparison between adsorption isotherms (black squares) and surface zeta potential (red circles) as a function of the surfactant concentration in the (a) *trans* and (b) *cis* state for surfactant adsorbed at a borosilicate glass surface. The Roman numerals roughly mark the fours region of the 4-region model shown in **Figure 7.1**.

At saturation, the number of molecules per unit area was estimated to be 1.75±0.5 molecules/nm^2. Indeed, at saturation for both isomers the adsorbed amount was found to be 140ng/cm^2 with M_{Azo}=397,6g/mol. According to calculations, this means that the area occupied by surfactant head group is $A_{trans} = A_{cis} = 1\text{nm}^2$.[168] Therefore, a double layer should be formed on the surface.

In this way the amount adsorbed in the diffuse layer can be calculated as with $\Gamma_{EDL} = \Gamma_{QCM} - \Gamma_{\zeta(c_{sat})}$, where $\Gamma_{\zeta(c_{sat})}$ represents the amount adsorbed in the first (Stern) layer, and Γ_{QCM} gives the amount of all adsorbed surfactants (including enclosed water). Using the values for Γ_{QCM} and $\Gamma_{\zeta(c_{sat})}$ from **Figure 7.7**, one gets 310ng/cm^2 for *trans* and 240ng/cm^2 for *cis* surfactant at each saturation. Under the assumption of a bilayer in the Stern layer with 140ng/cm^2 in the EDL, much more surfactant is adsorbed, thus indicating multilayers or other solloid structures.

Electrostatic interaction attracts the charged heads to the surface. Therefore, in a monolayer, surfactant molecules would point their tails into solution. This favors further attraction by hydrophobic interaction, attaching incoming surfactant in a tail-to-tail formation. Most likely, this picture looks different in *cis* solution with various formations possible because of its stronger polarity and kinked geometry. Previous studies have suggested a variety of possible surface structures.[36, 124] This gives only an idea of how crowded the surface may look. The formation of the layer lies beyond the scope of the thesis but could be of interest for further studies. Measurements using an

AFM are one possible technique that has proved to be a good source for observations. Nevertheless, a qualitative picture can be drawn from these estimations, giving an idea of the structure of the EDL.

A further comparison between adsorption and zeta potential shows that, for *trans* surfactant, region II of the adsorption model coincides with the steep increase around 0.01mM of the zeta potential (**Figure 7.7a**). This result confirms the interpretation of the adsorption isotherm that mutual interaction becomes important at this point and that further surfactant is adsorbed in surface aggregates against electrostatic repulsion.

In the case of *cis* solution, the picture is more complicated. Indeed, in the 4-region model of adsorption, the plateau of the adsorbed amount (**Figure 7.7b** region II 0.01mM – 0.1mM) at 0.01mM is a result of charge compensation, while SZP measurements indicate charge saturation at 0.03mM (IEP). The possible explanation of this deviation is presented in detail below. The solution of *cis* isomers contains around 10% of *trans* isomers. By increasing of the absolute surfactant concentration, the amount of *trans* isomers also increases. This results in a competing adsorption of both isomers, during which *trans* isomers adsorb more readily. One might think that there is a replacement of *cis* isomers by *trans* isomers at the plateau (0.01mM – 0.1mM).

As discussed above, QCM-D measurements are known to measure the weight of the water occupied at the surface, which does not affect the SZP (i.e., with formation of admicelles (adsorbed micelles)). Incorporated water could cause an overestimation of the adsorbed amount; it cannot, though, explain the deviation from SZP measurements in the low concentration range.

Zeta potential measurements reveal electrostatic properties of the surface layer. At the CMC, it is already saturated for *trans* and *cis* solution. The saturation values for the SZP are between 10mV and 20mV larger for a *trans* solution than for a *cis* solution. Similar to adsorption isotherms, zeta potential increases for surfactant in the *cis* state at larger concentrations than in the *trans* state. Surfactant in the *cis* state is less likely to attach to the surface, which could explain the increased hydrophilicity and larger steric hindrance compared to surfactant in the *trans* state. These differences could explain adsorption and zeta potential differences. Zeta potential measurements and adsorption isotherms coincide in interpreting the mechanisms for solution in the dark

state. In *cis* solution, the four-step model does not adequately explain the behavior in the concentration region between 0.002mM and 0.3mM.

Similar measurements were conducted for a hydrophobic surface (i.e., glass substrates were covered with a thin layer of Teflon AF 1600). Due to large measurement errors, only a qualitative picture is given here. A more detailed interpretation is given in Appendix A. In water solution, the hydrophobic surface was rendered negative with values given in literature to be around -60mV.[158] Both solutions, *trans* and *cis*, follow a sigmoidal shape with saturation reached at 0.01mM for *trans* and 0.1mM for *cis* solution. The maximal SZP for both solutions was measured to be around –(55±10mV), which was much larger than for the glass surface (~20mV). Similar to the SZP on the glass surface, the sigmoidal curve of the *cis* solution was shifted to larger concentrations. Comparison to adsorption isotherms suggest a monolayer or bilayer formation at saturation concentration for both isomeric solutions on the hydrophobic substrate.

7.8 Summary and conclusion of surfactant adsorption

The aim of this chapter was to analyze surfactant adsorption in order to clarify how the diffusioosmotic flow is established and what influence the hydrophobic surface has on adsorption in order to explain the inward and outward flow profile during UV laser irradiation.

It is apparent that surfactant adsorption clearly differs depending on the photostationary state of the solution. Furthermore, the effect of hydrophobicity was investigated with respect to adsorption. From this analysis, the following conclusions can be drawn:

a) On the hydrophilic surface *trans* isomers adsorb better to the surface than *cis* isomers. This could be explained by the cooperative interaction that is superior for the *trans* isomer. Nevertheless, for both *trans* and *cis* solutions, estimations of the number of molecules aligned at the surface suggest a double layer formation. This formation is considered to be facilitated by a head-to-surface and tail-to-solution orientation.
b) Compared to the hydrophilic substrate, maximum adsorption on a hydrophobic substrate is diminished, almost halved for the *trans* molecule. This fact might be

explained by the orientation of the molecules on the hydrophobic surface. A tail-to-surface and head-to-solution configuration creates an electrostatic barrier that hinders further adsorption.

c) Measurements of the surface zeta potential suggest that surfactant adsorption above 0.1mM contributes to surface excess in the diffuse layer. This might explain why LDDO flows appear above this concentration.
d) The differences in adsorption between *trans* and *cis* isomers indicate a desorption of surfactant under UV irradiation, shown for all concentrations above 0.1mM on the glass surface. Focused irradiation, therefore, should induce a decrease of surfactant concentration near the surface, changing the osmotic pressure in the irradiated area and leading to LDDO. However, in concentrations above the CMC, micelle decomposition could lead to a larger concentration in the irradiated area.
e) The flow direction might be explained by the total adsorbed amount and the gradient of surface excess with respect to concentration.
f) Adsorption kinetics indicate micelle adsorption and reorganization for adsorption of *cis* isomers on the glass surface and *trans* and *cis* isomers on the hydrophobic surface.

We should mention that definitive conclusions for LDDO flow cannot be drawn. QCM-D and zeta potential measurements have previously been performed in an equilibrated solution. However, LDDO is a highly dynamic process in a confined, small area. Therefore, these measurements can give only a limited picture of what happens under illumination. As a next step, in-situ illumination could reveal a clearer picture of the dynamics in this process, which could facilitate a better understanding of LDDO.

8 STRUCTURING OF PARTICLE ASSEMBLIES

The previous chapters analyze LDDO by tracking particle trajectories and calculating their speed. The variation of experimental conditions could help in understanding particle motion and its driving flow. Understanding physical phenomena, however, is not the sole motivation driving research. Applications for basic research are often asked for.

This chapter explores the use of LDDO. Especially, it intends to show how particle assemblies are organized and manipulated. Preceding chapters already take a small step into manipulation of particle motion, such as guidance along a channel system or the positioning of single particles or of microrods. This chapter investigates how a combination or single laser beam can be used to control particle assemblies in a different way.

First, it is shown how a single laser could be used to "draw" certain structures into a denser monolayer of silica particles. It also includes a combination of UV and green spot irradiation that leads to lovely structures. The process of cleaning or aggregation with a single spot is effective, but splitting the beam could result in a more interesting structuring. Instead of a single spot that can generate LDDO, an elongated laser beam opens opportunities to manipulate larger particle assemblies, which is shown in the last part. During all measurements, an AzoC6 concentration of 1mM was maintained. Any particle gathering in green light was induced for a *cis* dominated solution (i.e., when the solution was illuminated globally with UV light).

8.1 Drawing structures with a single laser beam and a combination of laser beams

Cleaning and aggregation with LDDO flows can be applied to structure ensembles of objects, such as silica particles of different sizes. Increasing particle density on the surface makes it possible to create shapes, "draw," or "write" into this

2D-like layer. The easiest thing to do is to move the microscope table around to create a less dense area of particles. In this way, the "UP" for "Universität Potsdam" and the "happy man" was drawn (**Figure 8.1a,b**). Because clean surfaces need at least 5 minutes for a diameter of 60µm, a clean picture takes from 15 minutes to an hour depending on the size of the image. Since particles still move with Brownian motion, they tend to move back into the less dense areas when the laser is positioned at another location. Thus, the image blurs with time between minutes and several tens of minutes.

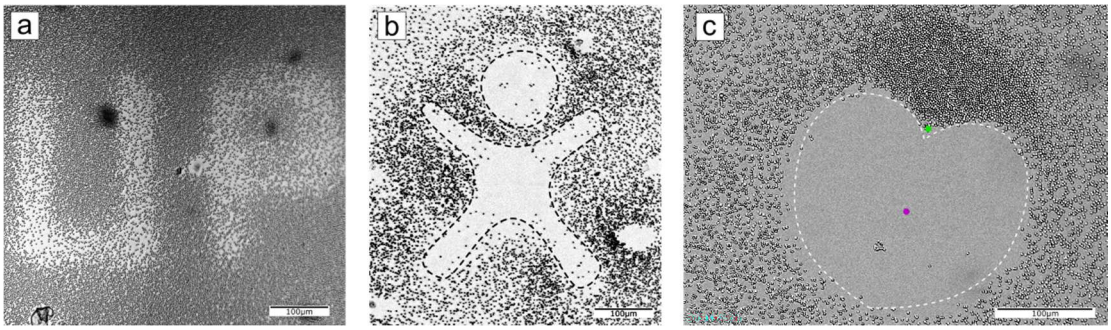

Figure 8.1. (a, b) Structuring of a particle monolayer by lateral repositioning of the laser spot across the solid liquid interface: logo of the University of Potsdam (UP) and the "happy man." (c) "Heart" shaped patterned inscribed by employing simultaneous irradiation with UV (red dot) and green light (green dot).

Particle assemblies can be patterned in a more complex way. Applying both lasers, UV and green, makes it possible to simultaneously aggregate at one position, as well as clean an area partially—for instance, as shown in **Figure 8.1c**, in which particles gather around the green laser spot and escape from the UV laser spot, leaving behind a heart shaped void with high particle density on top.

8.2 Beam splitting

With different techniques, it is possible to customize the patterning of particle assemblies. For example, the beam can be split into multiple beams by a diffracting optical element (DOE). As proof of principle, a polycarbonate multispot DOE (MS-466-Q-N-X, 532nm, HOLO/OR, Israel) was placed in the beam path after collimation of the laser beam. The DOE splits the single laser into a cross-like beam, depicted in the inset of **Figure 8.2**. Under continuous green laser irradiation, the particles resemble the cross-like pattern of the DOE (**Figure 8.2**). The patterning differs depending on the

irradiation intensity. At high intensities, more particles gather around the beam spots (**Figure 8.2a**). With intensities used normally, particles primarily move the central points, only slightly gathering around the peripheral laser spots (**Figure 8.2b**).

This variation in pattern results from the nonuniform intensity distribution of the laser spots. The DOE splits the single beam into multiple beams with a higher intensity near the central region. Therefore, particles primarily are located near the central region at normal intensities. Peripheral points reach only small intensities and LDDO flows are much weaker and assemble considerably fewer particles. To compensate this unequal distribution of intensity, an increase in laser power leads to a larger particle assembly. The intensity used in **Figure 8.2a**, however, was so high that optical pressure affected the particles in such a way that they were pushed away when they came to close to the laser spots. This is why the areas around the laser spots are free of particles. With careful intensity variations, we achieved good control over the resulting particle assembly (**Figure 8.2b**).

A dynamic change of a laser beam can be reached with a spatial light modulator (SLM). An SLM consists of a liquid crystal surface. When a collimated laser beam hits the surface, the light is modulated depending on the surface structure. The key point is that the liquid crystal can be controlled to accomplish almost any desired shape or pattern of the laser beam; even a continuous modulation of the laser spot is possible. For example, a single laser spot can be created that moves in a circle, creating a circular particle assembly. Single particles could be directed to a desired position.

Any type of laser-modifying element can be used to structure particle assemblies located on a surface. In the sample below, a membrane consisting of 2µm periodic structure was used to split the irradiation beam into multiple beams by diffraction. Light intensity diminishes for each order of diffraction; however, a patterned structure can be produced: 1) A UV laser creates voids of space around the laser spots (**Figure 8.3a**); 2) a green laser can be used to accumulate particles around each laser spot (**Figure 8.3b**). The largest accumulation is at the 0-th order with less accumulation around the higher order of diffraction.

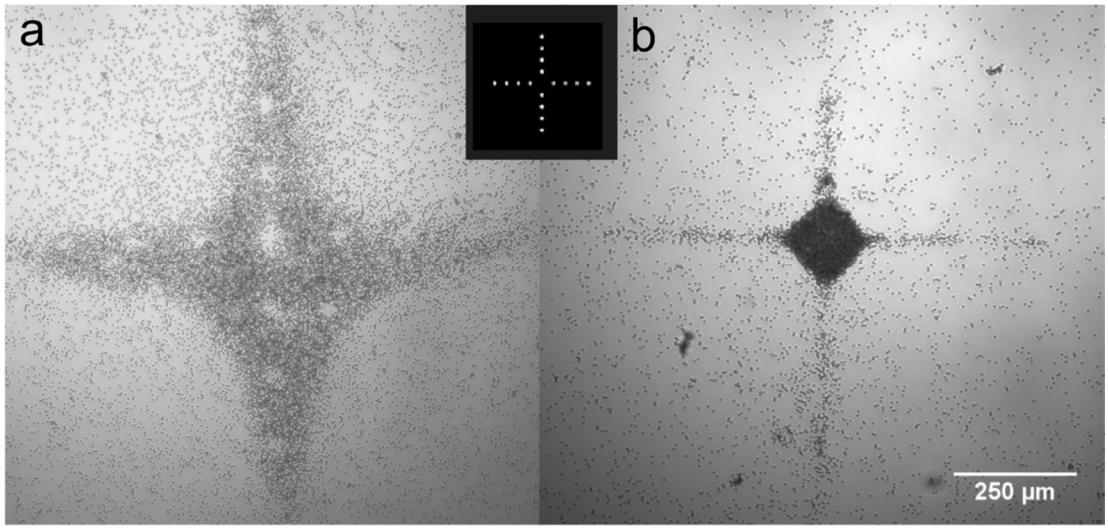

Figure 8.2. Micrographs of patterned assemblies of silica particles (2µm). A green laser (532nm) is split into multiple beams by a DOE with the profile shown in the inset at the top. Under irradiation, particles assemble in a cross-like fashion. Laser intensity is distributed unequally between the resultant laser spots with the highest intensity in the center. a) Under a higher laser intensity, particles create a large assembly with depletion areas in the irradiation centers, which are the result of high radiation pressure due to high intensity. b) At lower (standard) intensity, particles are attracted mostly by the more intense central region. However, a cross-like structure becomes visible.

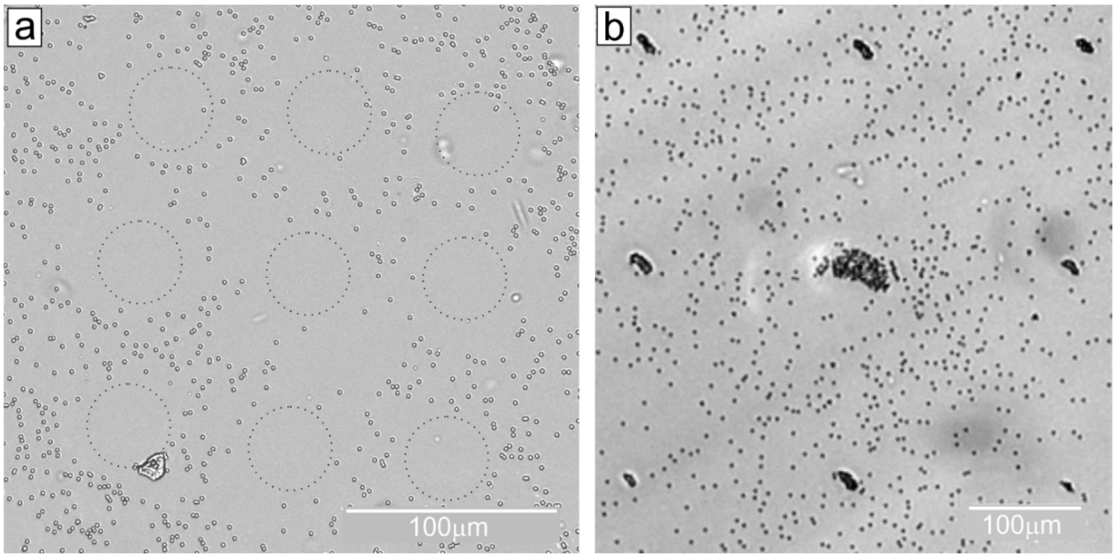

Figure 8.3. Micrographs of particle assemblies after irradiation with laser light split into multiple beams through a periodic mask using: (a) UV light and (b) green light. The aqueous solution contained 1mM of AzoC6. In case of green irradiation, a UV lamp preliminarily illuminated the solution.

8.3 Beam shape

Laser beams cannot only be split into multiple beams but also can be reshaped by other optical elements. For example, using a cylindrical lens changed a single spot into a line. This type of lens was placed into the beam path of the UV laser. When the flow of a single laser spot induced radial outward motion, the flow of a laser line induced a straight outward motion (**Figure 8.4**). Primarily, silica particles are distributed on the surface. Indeed, a vertical laser line leads to a horizontal flow, which drives particles horizontally outward. Thus, with a UV line, it is possible to split a particle assembly into two parts.

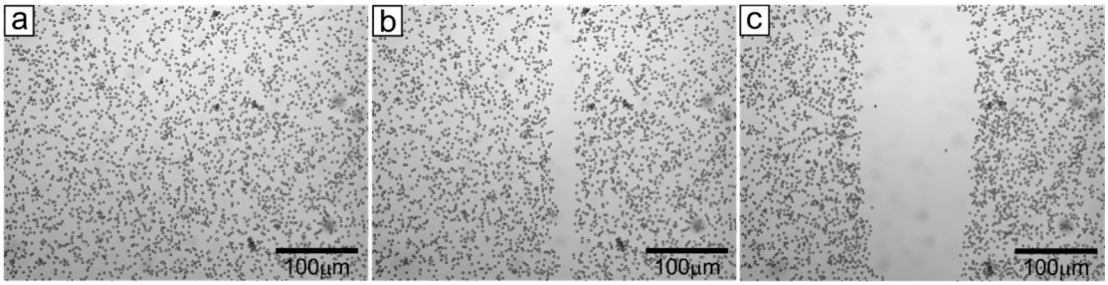

Figure 8.4. Micrographs of particle assemblies divided by a line-shaped laser beam (a) before irradiation, (b) after 1min, and (c) 10min of UV irradiation. Particles were distributed on a glass surface and dispersed in 1mM AzoC6 solution. The corresponding movie is shown in Appendix C9.

8.4 Summary and conclusion

This chapter shows that almost anything can be drawn or written into a layer of particles by manipulating the laser beam. With multiple beams, LDDO could be used to structure any kind of mobile object in a solid-liquid interface. A manipulation of the laser shape opens a large variety of opportunities to structure relatively easily. These manipulations, of course, have limitations. It was found that diffractive patterning of particles depends on the laser beam intensity. Higher order diffraction, therefore, leads to less aggregation or cleaning. It seemshat this has a larger effect on aggregation than on cleaning.

9 LIGHT-DRIVEN COLLECTIVE AND SELF-PROPELLED PARTICLE MOTION

In the previous chapters, the concept of LDDO is introduced, explored, and discussed. It is shown that focused laser irradiation generates a local hydrodynamic flow that drives particles toward or away from the center of irradiation. This is due to a local isomerization of azobenzene containing surfactant, which forms a concentration gradient driving a diffusioosmotic flow. This flow can be utilized to drive passive particles. In this chapter, the photosensitive surfactant extends its capability into the field of active particle motion. It is shown that the collective interactions between porous silica particles can be controlled by global illumination of the sample with different wavelengths.

This chapter gives an overview of this phenomenon and proposes a first mechanism that is based on LDDO. Furthermore, it shows how a symmetry break can induce a superdiffusive motion of so-called Janus particles—porous particles covered on one half with a metal layer.

The chapter is structured into five main sections: 1) a light-induced wavelength dependent reversible clustering and separation of porous colloids using azobenzene containing surfactant; 2) a proposed mechanism based on diffusiophoretic particle motion; 3) an application example (i.e., drawing with light); 4) the introduction of a self-phoretic particle based on the motion described for porous particles by a symmetry break; and 5) a summary and conclusion.

9.1 Clustering and separation under red and blue illumination

Porous particles (d = 5µm, pore size ~ 6nm) as shown in the SEM image and scheme in **Figure 9.1**, were dispersed in aqueous solution of AzoC6 (c_{azo}=1mM) and filled in a closed chamber placed in the optical microscope.

Without illumination (or under red light), the porous particles settle down to the solid-liquid interface and form different aggregates (**Figure 9.2a**). The snapshots below were taken after 5min. Image acquisition was performed under illumination with red light of λ = 600nm, leaving isomerization unaffected. When blue light (λ = 450nm) was switched on, the aggregates separate within tenths of seconds, and the particles form a grid with rather uniform particle-particle separation, as long as the illumination is maintained for at least one hour of irradiation (**Figure 9.2b, c**).

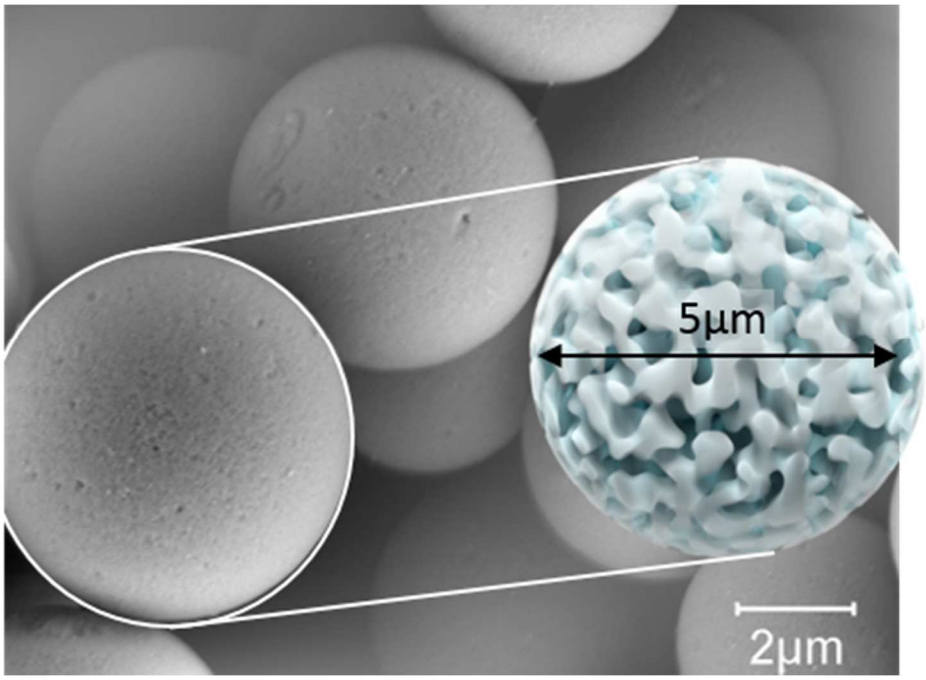

Figure 9.1. (a) SEM image and scheme (insert) of the porous particle of 5µm in diameter and pore size of 6 nm.

For this particular case, the distance between the particles was measured to be of about 15µm (**Figure 9.2f**). Due to Brownian motion, the particles being trapped in certain positions still wiggle. Most likely, the particle separation is driven by a hydrodynamic repulsion of the local hydrodynamic flow generated at each single colloid. Single particles (which can be followed by the eye, two particles "I" and "II" are marked in **Figure 9.2b**) do not show displacement at the beginning of irradiation. Only when other moving particles approach the repulsive interactions alter the position

of the colloids. After switching off the external light source, the long-range hydrodynamic repulsion disappears, and the particles aggregate again within a few minutes (**Figure 9.2d, e**).

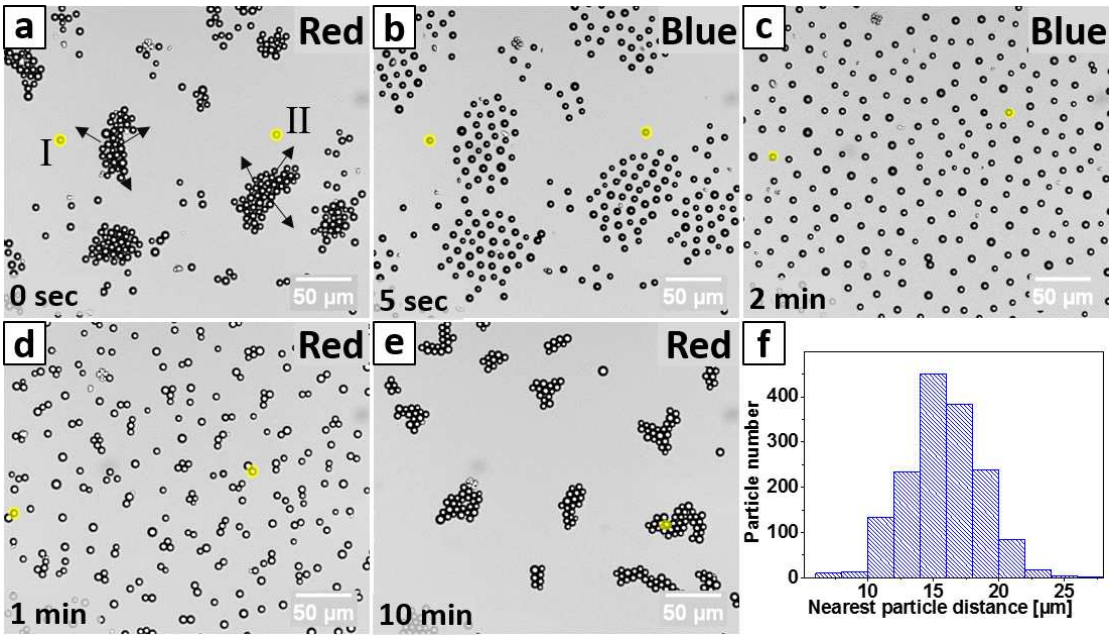

Figure 9.2. Optical micrographs of silica porous particles (d = 5 µm) trapped on a glass surface immersed into azobenzene containing surfactant aqueous solution (cazo = 1 mM). (a) Before irradiation, particles aggregate, (b) after switching on irradiation with blue light (λ = 450 nm, I = 1.5mW/cm2), the particles move apart and reach a stable steady state with a narrow, unimodal distribution of interparticle distances (c). (d-e) After switching off the illumination, the particles resume aggregation within minutes. (f) Nearest particle distance (NPD) distribution calculated from (c). In Appendix C10 the corresponding video is provided.

This separation/aggregation cycle can be conducted many times by applying periodical irradiation with two different wavelengths—blue light (separation) and red light (aggregation) (**Figure 9.3**). To characterize the particle distribution, we introduced the NPD parameter, which is defined as the smallest center-to-center distance to the neighboring particle averaged over the whole particle ensemble. **Figure 9.3a** shows the dependence of the NPD on irradiation time and wavelength for three subsequent irradiations with blue light (λ = 450nm). The particles are separated every time when the blue light is switched on forming a pattern with a well-defined particle distance of 15µm (**Figure 9.3d**, **f**). The separation takes place within seconds of

irradiation (**Figure 9.5b**). When the blue light is switched off, the NPD decreases down to 5µm revealing ongoing aggregation and saturates after about 5 minutes (**Figure 9.3a**).

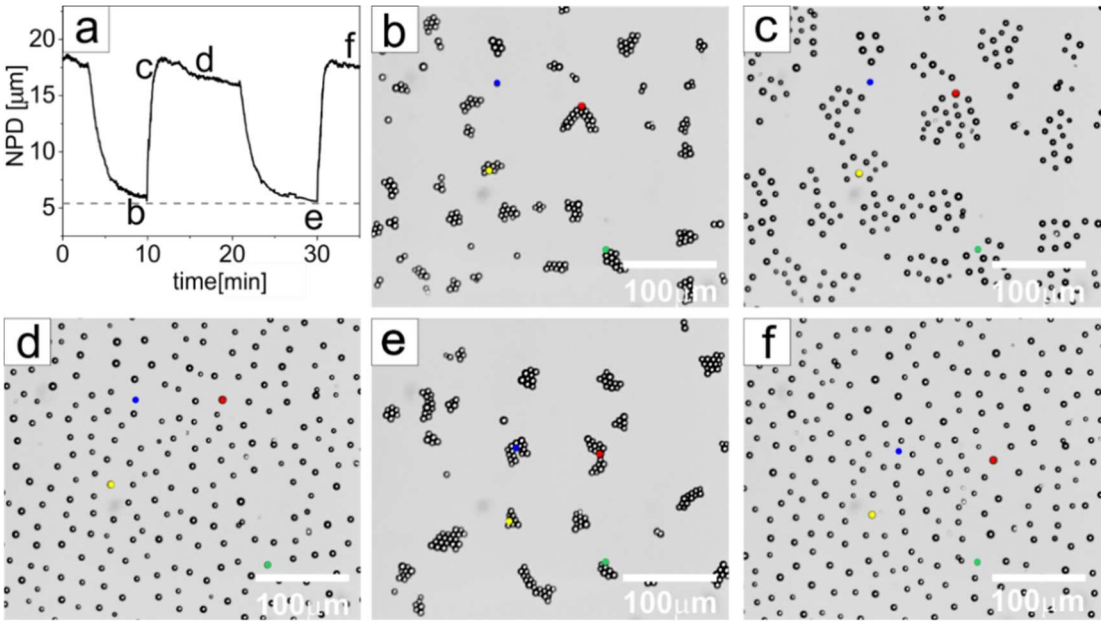

Figure 9.3. (a) Dependence of NPD on irradiation wavelength and time. The starting point on the plot (t = 0) is at the first irradiation event, when the particles are well separated and form a periodic grid with an NPD of 17µm. (b-f) Optical micrographs taken at irradiation steps marked in (a). (b) At the end of particle aggregation under red illumination, (c) beginning of the particle separation (2d cycle) under blue light, (d) stable particle pattern under blue irradiation, (e) end state of the aggregated state, (f) separated particles during 3d irradiation cycle. Single colloids marked in color (red, green, blue, and yellow) help to identify the same area on the micrographs. The corresponding video is provided in Appendix C11. The videos were taken by Pooja Arya.

9.1.1 Particle separation dependence on particle surface density

It was found that the maximal achievable distance between the particles depends on the number of particles per unit area (i.e., the particle surface density (PSD)). **Figure 9.4** shows the dependence of the particle distance on the particle surface density during irradiation with blue light. As can be seen, the hydrodynamic repulsion is governed by a long range interaction potential at each single colloid is and protrudes over distances of up to about 86µm for the PSD of 84 particles/mm^2 (**Figure 9.4a**). By increasing the particle concentration, the distance between the particles decreases, as

shown in **Figure 9.4f**. The minimal measured NPD is 7µm for a PSD of ~10^4 particles/mm^2 (**Figure 9.4e**). When there is a large PSD, switching on blue light at the beginning of the particle separation process causes some particles to "jump" out of the surface, followed by falling back to the surface when a large free area is generated.

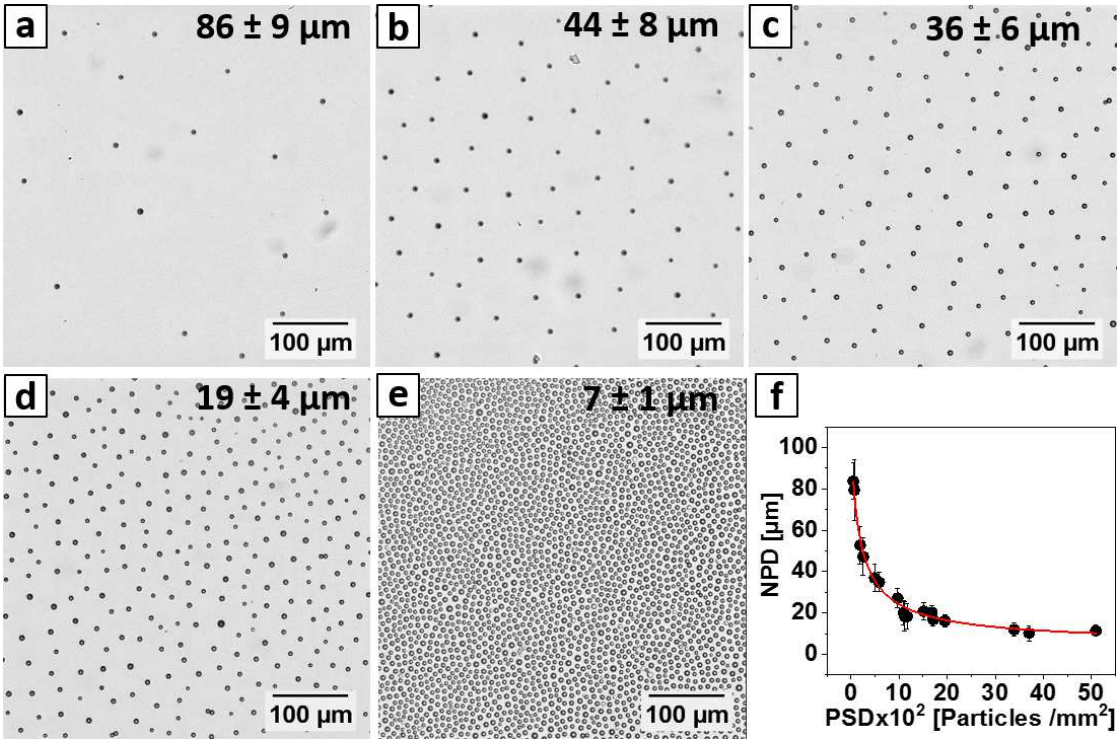

Figure 9.4. Optical microscope images of porous silica particles (d = 5 µm) in 1 mM azobenzene containing aqueous solution under blue illumination at different PSDs: (a) PSD=0.8x$10^2$$mm^{-2}$, b) PSD=3.4x$10^2$$mm^{-2}$, c) PSD=5.5x$10^2$$mm^{-2}$, d) PSD=1.6x$10^3$$mm^{-2}$, (e) PSD = $10^4$$mm^{-2}$. (f) Nearest particle distance shown as a function of the particle surface density for surfactant concentration of 1mM.

9.1.2 Particle separation dependence on surfactant concentration

The process of particle separation also depends on surfactant concentration. When the surfactant concentration is increased, the strength of repulsion increases as well, resulting in a larger NPD at a fixed PSD (**Figure 9.5a**). Starting from about 0.5mM (CMC), the NPD transitions into saturation. Following particle trajectories (recorded during transition from aggregated to well-separated state) reveals that most particles move away from the center of a cluster in a radial direction, except for particles initially located in the center of the aggregate (**Figure 9.5b**, insert). These

particles remain at their initial positions, implying a force balance around the particles. The particles at the outside of the aggregate lack neighbors; therefore, an effective force drives them outward. The velocity of single particles depends on the position of the particle inside the cluster **(Figure 9.5b)**. In the case of moving particles, the velocity increases to a maximal value within the first half second of irradiation and then slowly drops to zero within 10 seconds of irradiation, which is achieved when particles enter the distributed state (**Figure 9.5b**). The maximal velocities reached range between a few microns up to tens of microns per second. Averaging all particles yields values of around 8µm/s as the maximal velocity. Similar behavior of particle velocity change is observed for all surfactant concentrations between 0.2mM and 2mM. The absolute value of the maximal velocities, however, depends on many parameters, such as surfactant concentration, PSD, and the positions of the particles inside the cluster.

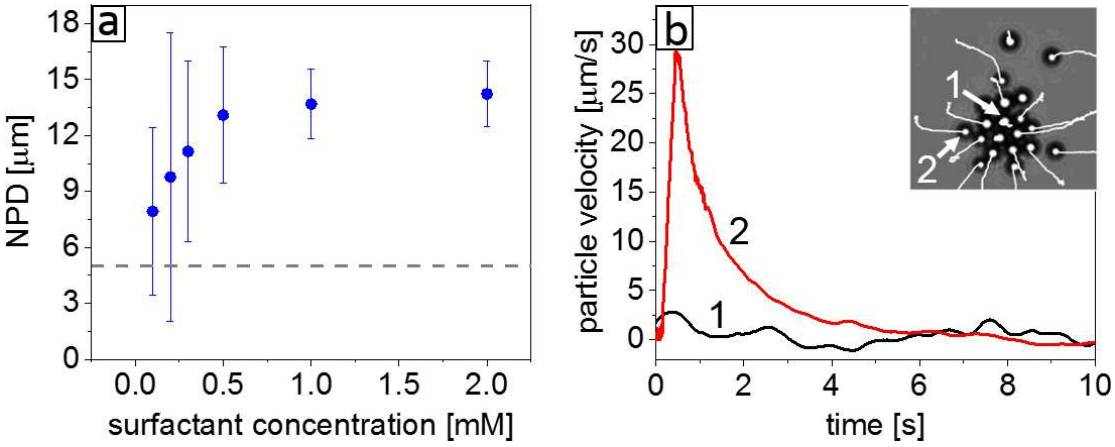

Figure 9.5. (a) The averaged NPD as a function of surfactant concentration at fixed particle concentration (PSD = 3.1mm^{-2}). The dashed grey line indicates particle distance in an aggregated state. (b) The average of all particle velocities from the image, inserted in the right upper corner, as a function of time. The trajectories of the particles are marked by white lines on the inserted micrographs. The red line depicts the velocity of the outer particles, while the black line corresponds to the particles in the middle of the aggregate.

9.1.3 Particle separation dependence on surfactant concentration

Particle repulsion was suppressed by increasing the ionic strength of the surfactant solution. An addition of NaBr decreases of the maximal particle velocity (averaged over all particles), showing complete suppression of particle motion at

10mM NaBr (**Figure 9.6a**). Furthermore, this effect can be observed by analyzing the NPD as a function of salt concentration (**Figure 9.6b**). The difference in NPD in the dark and after 10s of illumination with blue light decreases with increasing of salt concentration. Up to 2mM of NaBr salt concentration, when the Debye length drops down to about 6nm, the particle repulsion is still pronounced. Starting from 5mM NaBr, though, suppresses the particle motion.

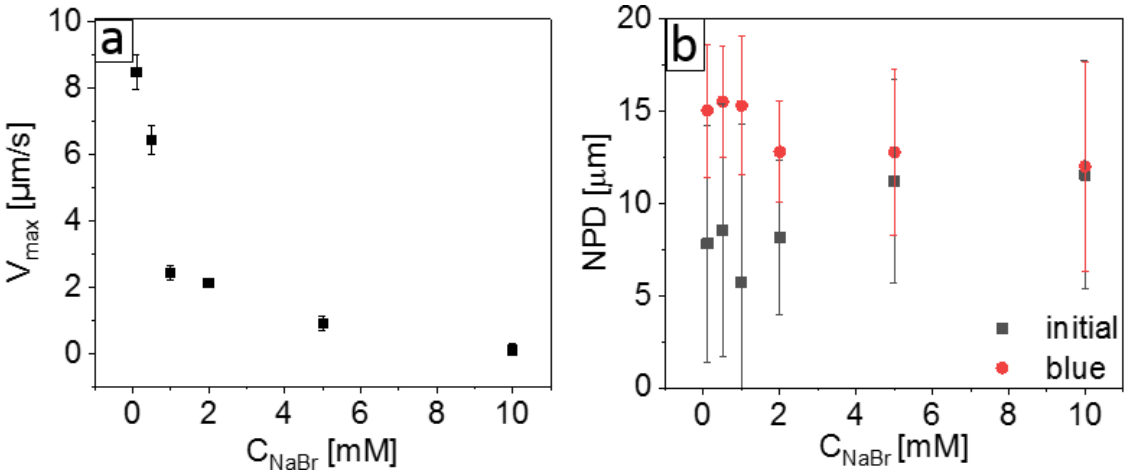

Figure 9.6. (a) Maximal particle velocity under irradiation with blue light and (b) the NPD as a function of the NaBr concentration. Increasing the salt concentration reduces the effectiveness of particle separation under blue light. Particle motion was completely suppressed at a concentration of 10mM. Surfactant concentration was fixed to 1mM, and the PSD was $35x10^{2}mm^{-2}$ for all measurements.

Based on the above results we can propose the following mechanism of light-driven reversible particle repulsion and aggregation. At the initial state (without irradiation), the surfactant molecules in the *trans* state adsorb into the pores of the particles. Due to high particle porosity, the amount of the absorbed surfactant increases significantly with the surfactant concentration. For example, with a surfactant concentration in a solution of 1mM and a particle concentration of 3.33mg/ml, only 0.3mM is left in the solution after porous particles are dispersed (**Table in Appendix B**,). In **Chapter 7** it is shown that surfactant in the *trans* state preferably attaches to the solid surface. Additionally, the energy gain from micellization in the particle interior facilitates adsorption into the pores. The absorption of the surfactant molecules results in a change of the Z-potential of the particles from -20mV (without surfactant) to

+26±7, +33±5 and +40±2mV for surfactant concentrations of 0.3, 1 and 2mM, respectively. In the dark state, the particles settled down at a glass surfaces tend to aggregate into clusters.

9.1.4 Separation and clustering of a mixture of porous and nonporous particles

To picture this process, we visualized a convection zone between repelling particles by adding nonporous small colloids to the solution. A mixture of porous and nonporous particles of 5µm and 1µm, respectively, were dispersed in 1mM surfactant solution (**Figure 9.7**). The particles are initially distributed on the surface as shown in **Figure 9.7a**: porous and nonporous particles appear, forming small aggregates as well as single objects. Under illumination with blue light, the porous particles start to repel from each other and form a well-distributed grid with particle distances of about 14µm (**Figure 9.7b**). At the same time, the small particles are pushed away from the porous colloids and are aligned at the stagnation points of the local hydrodynamic flows (**Figure 9.7b, d-f**). This indicates that a radial symmetrical hydrodynamic flow is generated at each porous particle under illumination. Switching back to red light induces an aggregation, including the smaller particles as seen in **Figure 9.7c**.

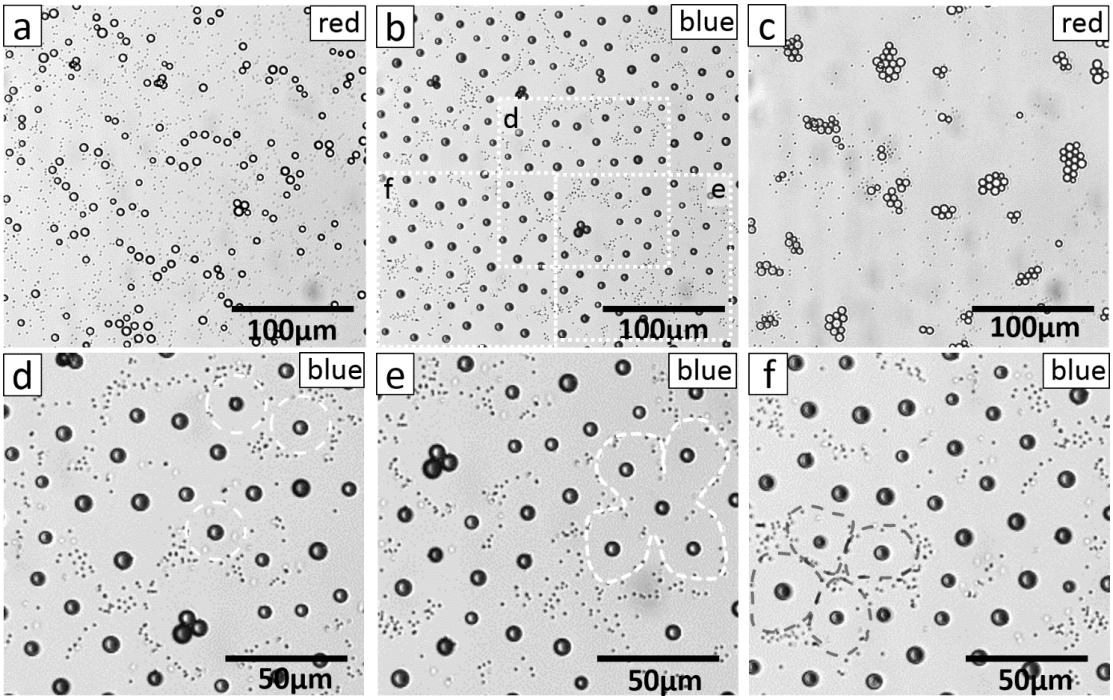

Figure 9.7. Optical micrographs showing the motion of porous (d = 5µm) and nonporous (1µm) silica particles dispersed in 1mM surfactant solution and exposed to illumination with (a) red light, (b) blue light (450nm), and (c) red light. (d-f) show enlargement of the selected areas in (b). The corresponding video can be found in Appendix C12.

9.2 A model for light-induced hydrodynamic repulsion

Under blue light, photoisomerization occurs within solution as well as inside the particles because the particles are transparent to 450nm. The *trans-cis* photoisomerization results in a release of the *cis isomer*s out of the porous particles (**Figure 9.10**). The release of the *cis isomer*s is governed by an increased osmotic pressure within the particles because the aggregates/micelles formed within the particles by *trans* isomers are destroyed during photoisomerization. The CMC of *trans* isomers is much lower than the CMC of *cis* isomers because the entropy gain on micellization is less for the hydrophobic isomers (*cis* state).[159] As a result, a concentration gradient of the isomers around a single particle is generated, inducing a diffusioosmotic flow away from the particles (**Figure 9.8**). In other words, the particles act as an effective source of isomers, which are released out of the interior of the

particles during irradiation. In this way, each single porous particle generates its own local hydrodynamic flow. Due to particle symmetry, that flow points radially away from each particle. When two or more particles are close to each other, these opposing flows generate the repulsive interaction that leads to the particle separation. This process is comparable to LDDO under UV light, generating a local concentration gradient of the *cis* isomers near the irradiated surface. A vanishing of motion with increasing NaBr concentration (**Figure 9.6a**) is explained by a decrease of the Debye length, which prohibits diffusioosmotic velocity (see **Chapter 5.1**).

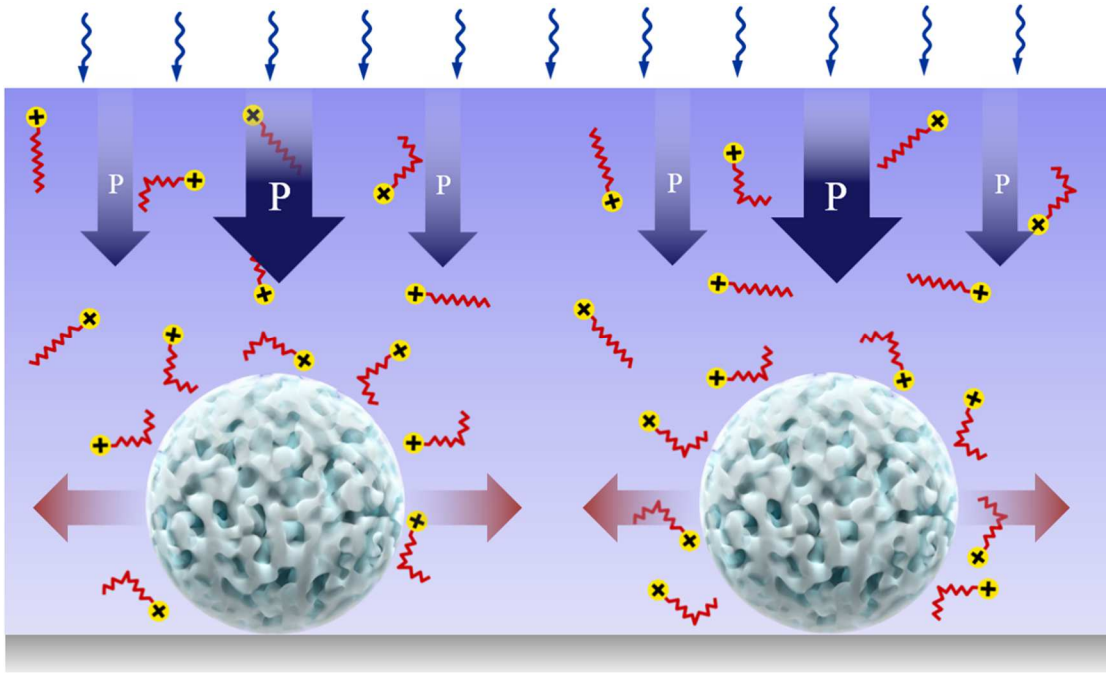

Figure 9.8. Scheme of LDDO flow generated at single porous particles under irradiation with blue light. The excess concentration of the *cis* isomers around the particle is generated during desorption of the surfactant molecules out of the particle.

A continuous blue illumination pumping out surfactant molecules is required for this process. The wavelength of irradiation plays a key role in the long time stability hydrodynamic repulsion. Indeed, under irradiation with blue light, the photostationary state (i.e., the fraction of *trans* and *cis* surfactant molecules in solution) shifts to 66% and 34%, respectively, implying continuous *trans-cis* and *cis-trans* isomerization. In this way, a long time stability of the particle separated grid is achieved because the stationary photoswitched *trans* isomers continuously adsorb into the porous particle,

replenishing surfactant reserves in the particles. In the case of irradiation with UV light, which also promotes *trans-cis* isomerization, the process of the particle motion and repulsion also occurs. However, the time of effective particle repulsion is shorter, around10 minutes of irradiation, depending on the light intensity (video in Appendix C13). This can be explained by the fact that under UV irradiation the photostationary state is achieved within minutes and a conversion from *cis* to *trans* is negligible, with 90% of the surfactant molecules switched to the *cis* state. Under these conditions, the amount of the *trans* isomers is exhausted within minutes, prohibiting continuous pumping of the *trans* surfactant within the porous particle. As a consequence, the LDDO flow vanishes. The repulsion of the particles disappears when the light is switched off. The surfactant molecules in a *trans* state diffuse into the pores of the particles, form aggregates inside, and the system returns to equilibrium. During adsorption of surfactant into the pores, the surfactant concentration around the particles is depleted. Therefore, particles gather on a switch off.

9.3 Writing with light

The process of the particles repulsion can be explored for many interesting applications. Here we would like to demonstrate two of them. The first possible application is light-driven turning of selective transmission of light through the surface covered with colloids (**Figure 9.9**). In the nonilluminated area, the particles scatter the light equally. A local irradiation of blue light induces particle repulsion. Therefore, light scattering is altered. In fact, it is reduced in this example, and the irradiated areas appear darker. In this way, one can, for example, write letters or draw figures (**Figure 9.9**).

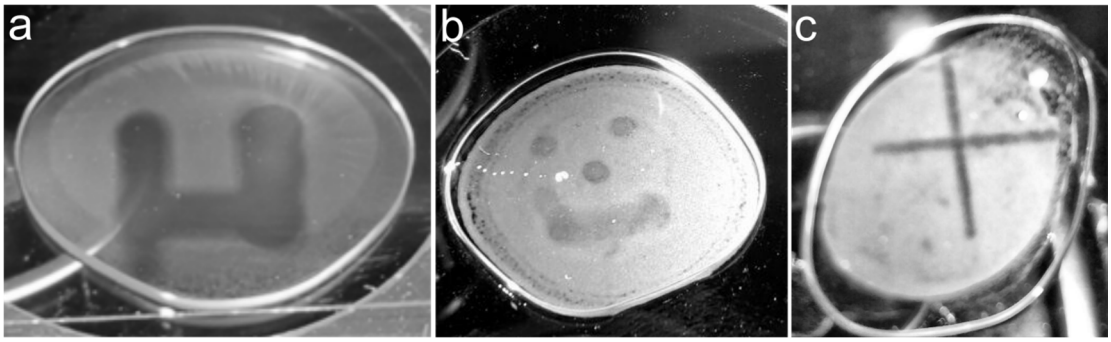

Figure 9.9. Images of a droplet containing AzoC6 (c_{azo} = 1mM) and silica particles (d = 5µm; c_{silica} = 2mg/ml), confined between two cover slips. Drawing of (a) a **µ**, (b) a smiley face, and (c) a cross by focused irradiation of blue light that has changed the particle distribution and, thus, decreased the scattering in the irradiated area.

9.4 From colloidal repulsion to artificial microswimmers

This photoinduced hydrodynamic colloidal repulsion can be used to create single self-propelling microswimmers. Indeed, when half of the particle is covered with a metal layer (forming Janus particle geometry), the symmetry is broken and the local hydrodynamic flow and the surfactant molecules can leave the particle only on one side. Thus, a concentration gradient is created between the capped and noncapped side. As a result a diffusiophoretic motion of the particle is induced by the osmotic pressure gradient imposed between both particle sides when the blue light irradiation is on (**Figure 9.10**). Without irradiation, the colloid is trapped at the surface and undergoes only thermal fluctuations. Example trajectories of a single Janus particle show clear differences between Brownian motion under red light and active motion under blue light (**Figure 9.10b**). When two Janus particles are coupled, they preferably move in spirals (**Figure 9.10c**). In fact, the motion can be more complex with angular velocity depending on the relative orientation of the particles.[160]

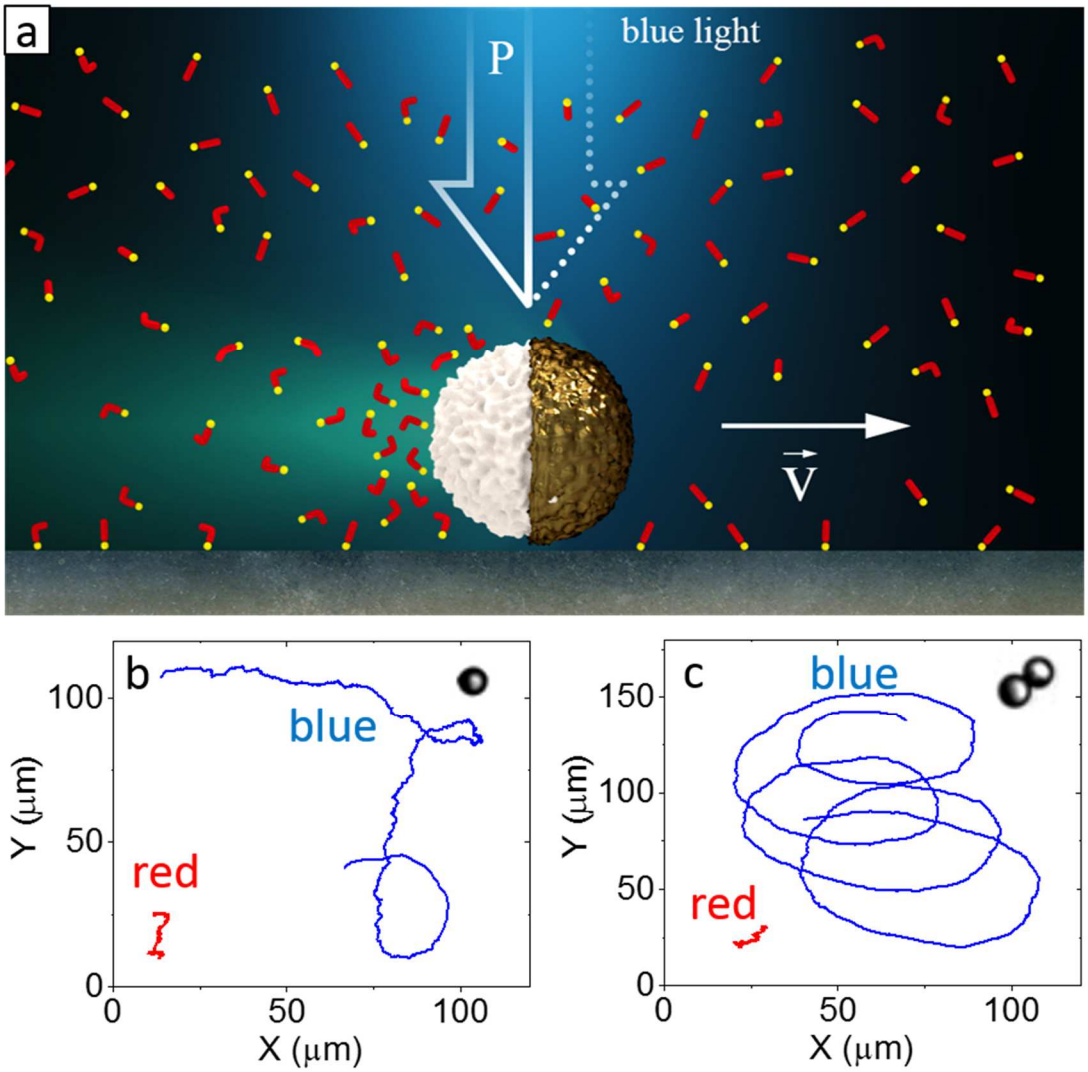

Figure 9.10. (a) Scheme of a Janus particle immersed in a surfactant solution and propelling along the surface under blue illumination. (a) Trajectories of a single Janus particle under red and blue light, (c) trajectory of a single Janus particle's self-propulsion under irradiation with blue light. The corresponding video of the Janus particle self-propelled motion is provided in the Appendix C14 and Appendix C15.

Particle motion of single Janus particles was analyzed by the calculation of the mean square displacement (MSD), which was averaged for five particles (**Figure 9.11**). Indeed, Janus particles show an enhanced MSD. For a propulsive microswimmer the MSD is given by **Equation (16)**:[161–163]

$$\mathrm{MSD} = \langle(\Delta\overrightarrow{\boldsymbol{r}})^2\rangle = 4D_{Trans}\Delta t + \frac{\mathrm{v}^2\tau_\mathrm{R}^2}{2}\left(\frac{2\Delta t}{\tau_R} + e^{-\frac{2\Delta t}{\tau_R}} - 1\right) \tag{33}$$

where D_{Trans} is the translational diffusion coefficient, Δt is the time interval, v is the velocity created by the propulsion mechanism, and τ_R is the rotational diffusion time. For times shorter than the rotational diffusion time this equation can be reduced to the following:[161–163]

$$\mathrm{MSD} = \langle(\Delta\overrightarrow{\boldsymbol{r}})^2\rangle = 4D_{Trans}\Delta\mathrm{t} + \mathrm{v}^2\Delta\mathrm{t}^2 \tag{34}$$

Propulsion speeds can be derived from parabolic fits of the MSD for times shorter than the rotational diffusion time of the particle ($\tau_R = 96$s) to be 0.5±0.1μm/s. Indeed, Janus particles show superdiffusive behavior (slope: 1.65) under blue irradiation and slightly subdiffusive behavior under red illumination (slope: 0.92) (**Figure 9.11** inset). In the case of times longer than τ_R, the MSD takes a linear form with a transition zone in between the short and longer times.

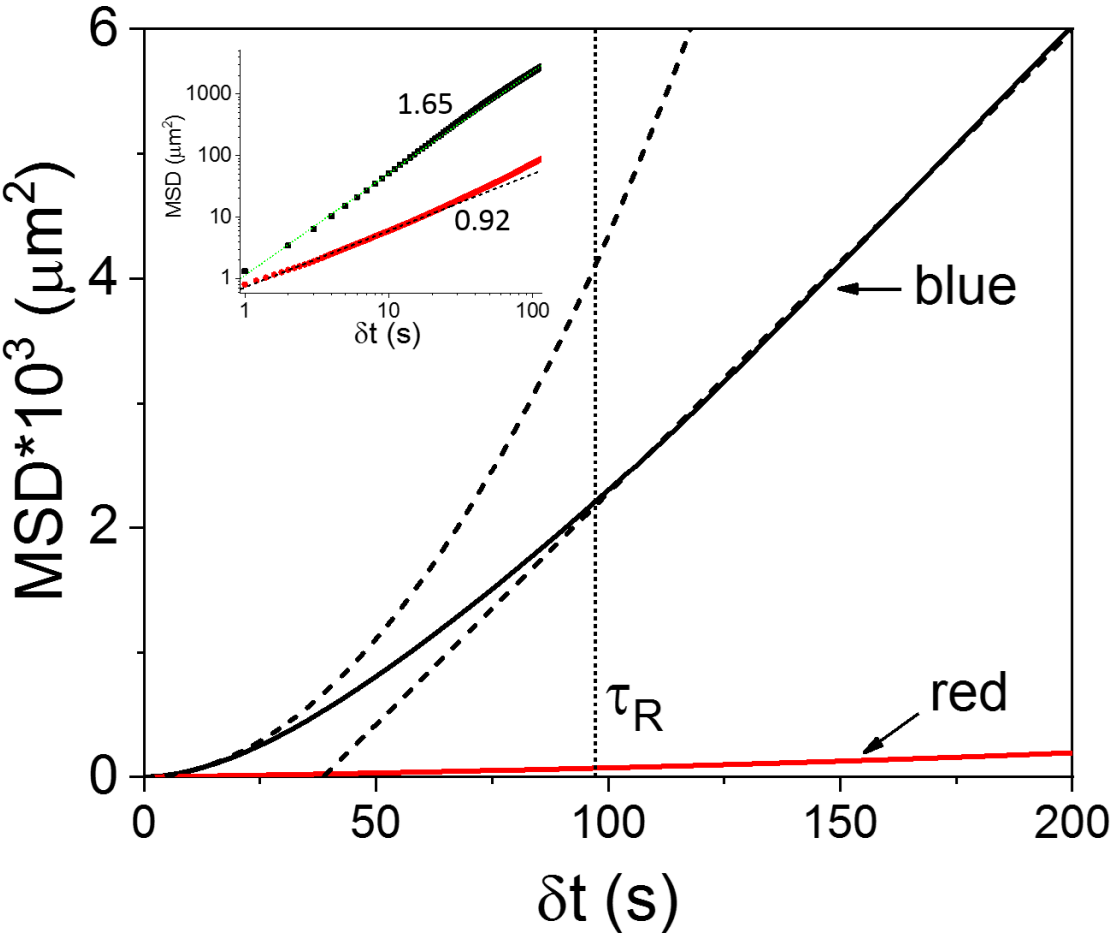

Figure 9.11. MSD as a function of time, comparing the motion of Janus particles under blue and red light. The active motion under blue light is fitted by a parabolic function for $t < \tau_R$ and by a linear function for $t > \tau_R$. From the parabolic function, the propulsion speed is derived to be 0.5±0.1µm/s. Inset: A log-log plot of the MSD with linear fits, at which the slope of the curve is shown. Janus particles show superdiffusive behavior under blue light and subdiffusive behavior under red light.

9.5 Summary

In this chapter, it is shown that azobenzene containing surfactant can promote active motion in porous particles. This is demonstrated by a light-reversible aggregation and separation of colloidal particles and by the self-propelled motion of metal capped porous particles (Janus particles).

When porous micron-sized silica particles are dispersed in the aqueous surfactant solution, the surfactant molecules in *trans* state diffuse into the pores, rendering the colloids positive. The particles settled on a glass surface form aggregates

during thermal motion in the absence of photoisomerizing light. During illumination with blue light ($\lambda = 450$nm), which promotes *trans-cis* and *cis-trans* isomerization, the colloids start to move and repel each other, forming a regularly spaced grid with an equidistant particle ensemble within a few seconds. The distances between particles can be achieved as high as 86µm at the particle diameter of 5µm. On switching off the light, the particles again form aggregates, yet more quickly and densely this time. One can iterate this process (repulsion, aggregation) by changing the irradiation wavelength. This process depends on different parameters, such as surfactant and particle concentration, ionic strength of the solution, and irradiation wavelength. The physical mechanism of the process can be explained by a generation of local hydrodynamic flows at each single porous particle during irradiation with blue light, which leads to local hydrodynamic repulsion at the convection zone. Indeed, at illumination promoting *trans-cis* isomerization, the surfactant molecules adsorbed inside porous particles are expelled out of the particle, which leads to an excess concentration of the *cis* isomer around a single porous colloid resulting in a situation similar to irradiation of the surfactant solution with a focused laser beam, namely LDDO. The mechanism of particle repulsion can be utilized to change light scattering at a densely packed colloidal monolayer, allowing a light-driven writing of different patterns. A single porous particle creates a symmetric concentration gradient around the particle, which does not lead to motion. Breaking the symmetry by closing one half of the particle yields self-propelled Janus particles. The motion can be explained in a similar way to the motion of porous particles: Blue irradiation leads to a concentration gradient on the outside of the particle. Due to the closed half side, surfactant can only escape from the particle on one side creating an asymmetric concentration gradient. Thus, a diffusiophoretic flow is created, driving the particle forward as an active Brownian particle.

10 SUMMARY, CONCLUSION AND OUTLOOK

This work is focused on the phenomenon of light-driven diffusioosmosis (LDDO) discovered in the framework of this thesis. It was shown that a photo-sensitive surfactant is able to drive hydrodynamic flows on the liquid-solid interface. This extends the previously known fact that a photo-sensitive surfactant induces hydrodynamic flows at the liquid-air interface by a change in surface tension upon irradiation. In addition to passive particle motion, a photo-sensitive surfactant has shown to promote a collective active motion of spherical micro-particles and a self-propelled motion of single particles when the particle symmetry is broken.

A radial inward or outward motion of micro-particles was induced by a focused laser beam when they were dispersed in a solution of azobenzene containing surfactant (**Chapter 3**). The outward motion (under UV irradiation) resulted in a surface cleaning, whereas the inward motion (under green irradiation) led to an aggregation of a particle ensemble. Particle velocities were shown to depend on the surfactant concentration and particle motion required a minimum concentration of 0.2mM. A pronounced onset of the motion was found at the critical micelle concentration (CMC). Around 1mM a maximum in particle speed with a slow decrease in speed at a further concentration increase.

In **Chapter 4** a theory was developed to explain the particle motion. It is based on the light-induced relative concentration change of surfactant in the *trans* and *cis* conformation near the solid-liquid interface. The concentration gradients of *trans* and *cis* isomers create a diffusioosmotic flow in the electrostatic diffuse layer (EDL) close to the surface. This concentration gradient does not only depend on the bulk concentration, but also on the interaction potential of the *cis* and the *trans* molecule, which is related to the molecular adsorption in the diffuse layer. An estimation of the diffusioosmotic velocity from the LDDO theory yielded flow velocities of around 7µm/s which is close to particle velocities observed to be about 1.5µm/s. A dependence on the Debye length, i.e. the thickness of the EDL was demonstrated in **Chapter 5**. An

addition of the electrolyte NaBr inhibited particle motion which is consistent with the theory. The fact that particle velocity is virtually independent of the particle size (in the range between 1µm and 10µm) indicates a negligible diffusiophoretic contribution. A variation in surfactant hydrophobicity changed the concentration dependent onset of motion. A change in hydrophobicity shifted the CMC (e.g. to lower concentration for more hydrophobic surfactant) and accordingly the onset of motion. Furthermore, shortening or lengthening led to a decrease of particle speed (i.e., the strength of the flow). These results suggest that micellization is essential in LDDO flow. This importance can be explained by a light-induced micelle decomposition at a *trans-cis* photoisomerization. A localized decomposition creates a larger concentration gradient in the vicinity of the laser beam and an increase in osmotic pressure.

In **Chapter 6** it was observed that the direction of the flow depends on the surfactant concentration on a strongly hydrophobic substrate. Below the CMC, a slow but inward particle motion was observed. At 1mM the particles close to the laser spot moved inwards, but particles farther away moved outwards. At a concentration to 2mM all particles moved outwards. This complex motion was absent under green irradiation where an inward motion was observed independent of the surfactant concentration. Additionally, a surface structure composed of microchannels were used to guide particle motion. However, guidance was limited due to a prevailing radial flow profile.

In **Chapter 7**, the surface-surfactant interaction on a glass and Teflon-coated surface was analyzed by measuring the isomer–dependent surfactant adsorption and the surface zeta potential (SZP). Adsorption isotherms and kinetics were measured by a quartz crystal microbalance (QCM). It was shown that surfactant adsorption strongly depends on the isomerization state of the surfactant and the hydrophobicity of the surface. An adsorption of surfactant in the *trans* conformation was larger for both the hydrophilic and hydrophobic surface. A stronger hydrophobic interaction of the *trans* isomers facilitates the formation of surface aggregates due to an improved surfactant-surfactant interaction (i.e., cooperative behavior). In addition to less hydrophobicity, the geometric constraints of the *cis* isomer might lower *cis* adsorption. These differences indicate that an irradiation induces a detachment of surfactant from the surface on a *trans* to *cis* photoisomerization. On the hydrophobic substrate surfactant

adsorption was decreased—most pronounced for *trans* solution. On the glass surface, adsorption differences between *trans* and *cis* isomers were much larger. In fact, on the hydrophobic surface, *cis* adsorption became almost comparable to *trans* adsorption. In SZP measurements both surfaces (i.e., hydrophilic and hydrophobic) yielded a negative SZP in water. An addition of surfactant increased the zeta potential beyond the concentration at which charge compensation takes place and resulted in a positive SZP to be about 30mV for solution of surfactant in *trans* conformation and 20mV for solution of surfactant dominated by *cis* isomers. The SZP measurements also indicate an adsorption in the diffuse layer, for *cis* solution at 0.1mM, but already at 0.01mM for *trans* solution. This might indicate a relation to the onset of LDDO motion at 0.2mM. The results obtained from QCM and SZP measurements demonstrate a change in the mass inside the EDL. This confirms that under localized irradiation a concentration gradient appears. This supports the theoretical explanation. Therefore, diffusioosmosis can be considered as the driving force of the flow. As these results explain an outward and inward motion under UV and green light, a definite explanation of the complex motion found on the hydrophobic surface could not be given. A tentative explanation might be given: On the hydrophobic substrate a negative slope was found for *trans* adsorption when plotted as a function of surfactant concentration between 0.5 and 2mM. In contrast to *cis* adsorption where a positive slope was observed. This difference could be seen as a cause of inward and outward motion. However, for clarification further research should be conducted. An ex-situ investigation of the adsorption kinetics of a separate *trans* and *cis* solution by QCM measurements revealed most pronounced differences above the CMC. The results indicate a two-phase adsorption. In a first phase, micelles adsorb directly to the surface. In a second phase, micelles decompose and surfactant molecules reorganize. This two-phase adsorption was found for both isomers on the hydrophobic surface at concentrations around each CMC of solution. This differs to adsorption on the hydrophilic substrate where the two phases were only observed for *cis* adsorption at the saturation concentration of 2.5mM (i.e., when surfactant adsorption remains constant at an increase of surfactant concentration).

In **Chapter 8** various irradiation patterns were explored. It was demonstrated that particle ensembles can be manipulated in a large diversity depending on the laser

configuration. It was shown that a motion of the laser beam can be used to inscribe different structures in a dense particle layer. It was also demonstrated that particle separation and aggregation can be used simultaneously inscribe more complex structures (e.g. a heart shaped void). Using multiple beams showed that a layer of particles can be patterned. Furthermore, a change in the laser shape has shown that the radial direction of the flow can be manipulated. In fact, a line-shaped laser spot could induce a straight outward motion perpendicular to the direction of the laser beam.

In **Chapter 9** it was shown that azobenzene containing surfactant can also promote active motion of porous particles. This was demonstrated by a light-induced reversible aggregation and separation of porous particles and by a self-propelled motion of metal capped porous particles, so called Janus particles. In detail, porous particles dispersed in surfactant solution showed a repulsion under global irradiation of blue light (λ = 450nm) which resulted in a particle grid with equalized inter-particle distances. A change to nonphotoisomerizing light (i.e., λ > 550nm) leads to a particle aggregation. A reversible separation and aggregation was found on a switching the wavelength of light. Similar to LDDO, the motion could be inhibited by the addition of salt. A possible explanation was presented that is based on LDDO. Surfactant molecules adsorb into the pores of the particles. Under blue light, a *trans-cis* photoisomerization inside the particles leads to a pumping out of surfactant. The increased concentration around each particle creates a diffusioosmotic flow (similar to LDDO) pointing symmetrically away from the particle. This leads to a hydrodynamic particle repulsion. When the light is switched off, surfactant molecules diffuse back into the pores which results in the depletion of surfactant around the particles and, thus, particle aggregation. Therefore, this process can be seen as a reversible switching of the hydrodynamic interaction. The symmetric flows around the particles induced the separation and aggregation. The repulsive force was used to promote a self-propelled motion of Janus particles that resulted in a superdiffusive motion of single particles and spiral motion of a dimer particle (i.e. one particle attached to another). This is done by breaking the symmetry of the symmetric hydrodynamic flows around each particle. A metal layer was evaporated on one side of a porous particle. An explanation was given based on the model of the motion of porous particles. Similar to porous particles, a

photoisomerization inside the particles pumps surfactant out of the particle. In contrast to symmetric particles, the surfactant can move out only on the unclosed particle side. Therefore, a concentration gradient is generated around the particle. This concentration gradient results in a diffusiophoretic particle motion.

The phenomenon LDDO was discovered in the course of this work. However, only a fraction of the nature of LDDO has yet been unveiled. This work gives a brief overview and derives a simple model that is able to explain the general motion that was observed. To comprehensively analyze and understand LDDO in future studies a large parameter space should be explored, such as the dependence of LDDO on the chemical environment (e.g. pH, liquid viscosity, liquid polarity), surface properties (e.g. charge, chemical groups, roughness), surfactant type (e.g. anionic, nonionic, mixed systems), or illumination conditions (e.g. the size of the laser spot). For the conclusive explanation of LDDO several questions remain open and should be answered in further experiments.

- How does the diffusioosmotic flow expands into the bulk and how is the flow affected by the thickness of the liquid layer (i.e. the distance between the bottom and cover substrate)? Numerical calculations using LDDO theory predict streamlines that expand into the bulk. Due to mass conservation, the closed streamlines should be present. Only motion on the surface has been observed so far. An increase in viscosity or a decrease in particle density could help to visualize the flow profile.
- Why does UV irradiation create a complex LDDO flow pattern on a hydrophobic substrate and why does green irradiation not show a similar but inversed motion? Ad- and desorption kinetics with in-situ irradiation could help to answer this question.
- Why does particle motion exceed the size of the laser spot multiple times and what determines the effective area of LDDO? A variation of the focal length and size of the laser beam could help answer this question.

Despite the fact that open questions have not been answered, the derived model was already successfully applied to explain the collective motion of porous particles and the self-propelled motion of Janus particles when dispersed in a solution of the

photosensitive surfactant. However, the proposed model should be tested in more detail. The following parameters should be explored to gain a more comprehensive understanding of the process: In LDDO, the particles were considered as tracer particles passively moving with the flow. However, the motion of porous particles depends on each single particle. Therefore, particle properties should be varied such as pore size, surface hydrophobicity, or surface charge. Light acts as the trigger for the active motion. Therefore, illumination conditions should be changed such as light intensity or wavelength. Of course, the parameter space of the general LDDO flow as described above could be explored.

Light-driven diffusioosmosis is able to explain passive and active particle motion. The use of the photosensitive surfactant give rise to more phenomena based on LDDO. And in the end, with the words of Purcell, we improved our understanding of elementary physics even if we did not throw much light on the other subject.

.

APPENDIX

A. Surface zeta potential on a hydrophobic surface

Glass substrates were spin-coated with Teflon AF1600 and the zeta potential was measured for consecutive concentration increase for a *trans* and *cis* solution of AzoC6 (**Figure A.1**). Note that because of strong variations of the SZP in the low concentration region that yielded values between -60mV and 20mV, these values were discarded. This large error could be a result of surface roughness due to polarization effects as explained in the methods section. Surface roughness on hydrophobic surfaces contributes to surface hydrophobicity by trapping vapor near the surface, known as the Cassie state.[164, 165] This might influence SZP measurements, in particular, in pure water.

Nevertheless, the results for larger concentrations are presented, showing the qualitative behavior between *trans* and *cis* solutions. Both curves differ from each other, especially in the range between 0.02mM and 0.1mM. For the dark solution, a sigmoidal curve shows a steep increase from 0.001mM, from -20mV to 0.01mM to almost 60mV, and passes the IEP at 0.002mM. At concentrations above 0.01mM, the zeta potential remains largely constant with an unusual drop at 0.05mM to 20mV, followed by an increase back to 60mV at 0.5mM, with constant zeta potential at further concentration increases.

The SZP of *cis* solution takes a similar route. It increases markedly around 0.003mM and then increases slowly up to 30mV at 0.01mM, with the IEP passed between 0.03mM and 0.04mM. An unusual drop appears at 0.03mM down to 10mV, which is followed by a steep increase to around 60mV at 0.1mM. Interestingly, the zeta potential drops at 0.5mM and 1mM to 50mV and 25mV, respectively, but it reaches saturation of 60mV around 2mM. The unusual drops were not taken into account due to measurement errors and further interpretation and were, therefore, omitted.

Both curves show certain differences. The only similarity is an equal saturation value (i.e., around 60mV). The largest differences occur between 0.001mM and

0.1mM. Whereas in dark solution the SZP rises fast (between 0.001 and 0.01mM), the zeta potential of *cis* solution reaches saturation around 0.1mM. The IEP only slightly differs between 0.001 to 0.003 for *trans* solution and between 0.002 and 0.004mM for *cis* solution.

Using these results, the interpretation of the adsorption isotherms can be expanded. The interpretation seems to fit roughly with the 4-region model of the isotherms, but only for *trans* solution: Around the IEP, the slope in the isotherm shifts, indicating the onset of region III, at which surface charge is considered to be compensated. The IEP coincides with the fast increase found in the adsorption isotherms. As discussed in **Section 7.6**, the 4-region model was not suitably applied; therefore, an interpretation was unclear. At the saturation (i.e., at a concentration of 0.1mM, the adsorption isotherm shows an infliction point at which the slope is reduced, indicating that adsorption becomes less effective.

Furthermore, the results from SZP measurements could be used to estimate the amount of surfactant adsorbed at this concentration. For dark solution, this yields values of 65±5ng/cm^2 at the IEP and around 90ng/cm^2 for the SZP saturation at 0.01mM. For *cis* solution, this differs largely, with around 25ng/cm^2 at the IEP and 140ng/cm^2 for the saturation at 0.1mM.

Because the measurements reveal large errors, the interpretation of the values is difficult. The results for dark solution, however, could be used. At the saturation of 90ng/cm^2, when converting this value to molecules/nm^2, it yielded values of around 1.1±0.4. This indicates a monolayer formed on the surface.

The apparatus for zeta potential measurement is highly sensitive to distortions. Therefore, these results should be taken with caution. Nevertheless, it gives some idea of how electrostatic properties change on surfactant adsorption.

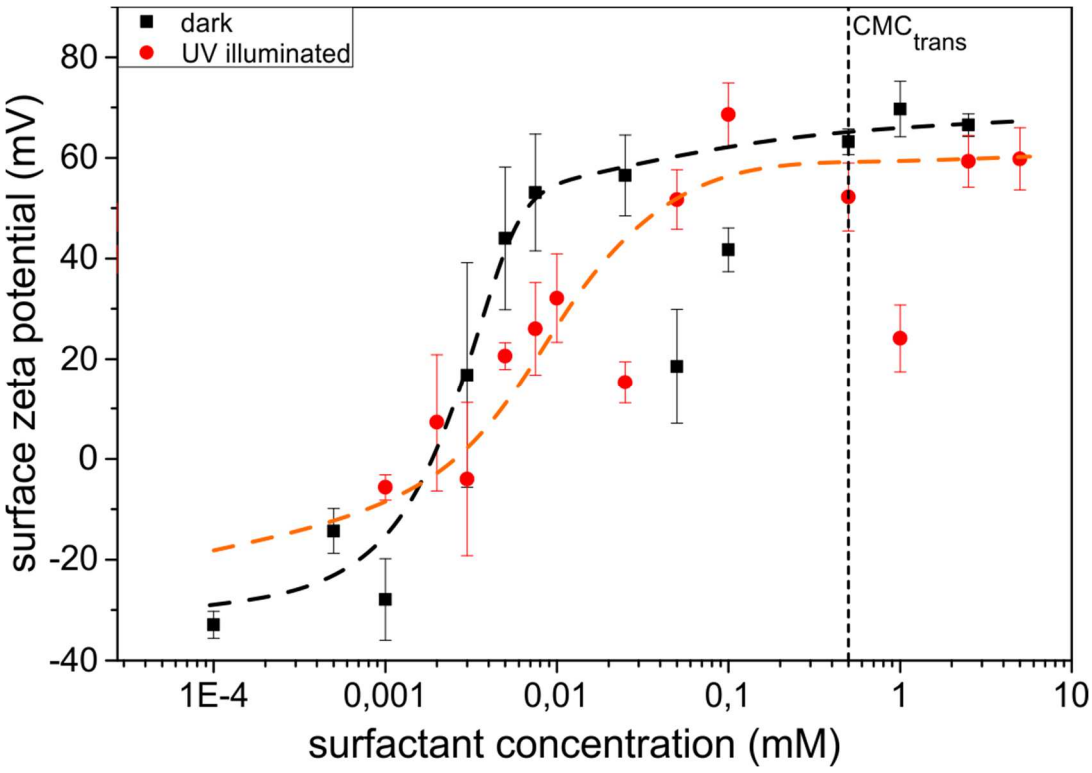

Figure A.1. Surface zeta potential of a glass surface coated with a thin film of Teflon AF1600 as a function of bulk surfactant concentration (AzoC6).

B. Surfactant adsorption in porous particles

Surfactant adsorption to the pores is measured by the depletion method. Porous particles are dispersed in solution of surfactant. Beforehand, the UV/vis absorption spectra were measured. After 80min of particles rested in solution. UV/vis spectra were taken again. Both spectra were compared and the adsorbed amount calculated. The results are presented in **Table B1**.

Table B1. Amount of surfactant adsorbed per mg (first column) when 5µm porous particles with 6nm in pore size are added to the surfactant solution of different concentrations. Concentration of the surfactant left in the solution is in the last column. The adsorption is given in various units.

$C_{surfactant}$, mM	µmol/mg	Molecule/nm^2*	(Molecule/Particle)**	concentration left in solution, mM
0.5	0.06	0.04	$0.5 \cdot 10^{10}$	0.29
1	0.21	0.14	$1.5 \cdot 10^{10}$	0.3
2	0.35	0.25	$2.5 \cdot 10^{10}$	0.8

* the adsorbed density of the surfactant in units of molecules per nm^2

** Number of surfactant molecules absorbed by one particle

C. Surfactant adsorption in porous particles

The following videos can be found on the CD in the booklet with names corresponding to „C1.avi“ to „C15.avi“.

C1. Video: Motion of silica particles (d = 2µm) on a glass surface under focused UV irradiation in 1mM solution of AzoC6.

C2. Video: Motion of silica particles (d = 2µm) on a glass surface under focused UV irradiation in 1mM solution of AzoC6

C3. Video: Motion of silica particles (d = 2µm) on a glass surface under focused green irradiation in a *cis* – dominated solution of AzoC6 (c_{Azo} = 1mM)

C4. Video: Motion of silica particles (7µm) forming a 2D crystal like structure on a glass slide under irradiation with a focused green (λ=532nm) laser. Particles were dispersed in solution of 1mM azobenzene containing surfactant.

C5. Video: Gathering of microrods by LDDO cAzo=1mM). They are directly attracted to the green laser spot (λ=532nm). The suspension was globally illuminated with UV light before the droplet was deposited onto the glass slide to create a cis-enriched solution.

C6. Video: Inward motion of 2µm silica particles in 0.3mM surfactant solution on a hydrophobic surface under focused UV irradiation.

C7. Video: In- and outward motion of 2µm silica particles in 1mM surfactant solution on a hydrophobic surface under focused UV irradiation.

C8. Video: The motion of silica particles (5µm in diameter) on a structured PDMS surface under focused UV irradiation. Particles are dispersed in a solution of azobenzene surfactant (concentration: 1mM).

C9. Video: Particle assemblies divided by a line-shaped UV laser beam. Particles with 2µm in diameter dispersed in 1mM and have been distributed on a glass surface and AzoC6 solution.

C10. Video: Separation and aggregation of silica porous particles (d = 5 µm) trapped at a glass surface immersed into azobenzene containing surfactant aqueous solution (c_{azo} = 1mM).

C11. Reversible aggregation and separation of porous silica particles (d = 5 µm) under red and blue light, respectively. Particles were dispersed in 1mM solution of AzoC6.

C12. Separation under blue and aggregation under red light of 5µm porous silica particles and non-porous 1µm in diameter that were dispersed in 1mM AzoC6 solution.

C13. Particle (d = 5µm, porous) separation under global UV irradiation. Particles were dispersed in a solution of 1mM AzoC6.

C14. Motion of Janus particle under blue light. A porous silica particle (d = 5µm) was coated on one half with a chromium layer of 5nm covered by a gold layer of 50µm. The particle was dispersed in 1mM AzoC6 solution.

C15. Spiral motion of a Janus particle dimer accidentally formed during the preparation process. The porous silica particles (d = 5µm) were coated on one half with a chromium layer of 5nm covered by a gold layer of 50µm. The particle was dispersed in 1mM AzoC6 solution.

BIBLIOGRAPHY

1. B. V Derjaguin, G. P. Sidorenko, E. A. Zubashchenko, E. V Kiseleva, *Kolloidn. Zhurnal*. **9**, 335 (1947).
2. B. V Derjaguin, G. Sidorenkov, E. Zubashchenko, E. Kiseleva, *Prog. Surf. Sci.* **43**, 138–152 (1993).
3. B. V Derjaguin, S. S. Dukhin, A. A. Korotkova, *Prog. Surf. Sci.* **43**, 153–158 (1993).
4. J. L. Anderson, M. E. Lowell, D. C. Prieve, *J. Fluid Mech.* **117**, 107–121 (1982).
5. D. C. Prieve, J. L. Anderson, J. P. Ebel, M. E. Lowell, *J. Fluid Mech.* **148**, 247–269 (1984).
6. J. L. Anderson, D. C. Prieve, *Langmuir*. **7**, 403–406 (1991).
7. J. L. Anderson, *Annu. Rev. Fluid Mech.* **21**, 61–99 (1989).
8. A.-L. M. Le Ny, C. T. Lee, *J. Am. Chem. Soc.* **128**, 6400–6408 (2006).
9. M. Sollogoub *et al.*, *Chembiochem A Eur. J. Chem. Biol.* **9**, 1201–1206 (2008).
10. A. A. Zinchenko, M. Tanahashi, S. Murata, *Chembiochem A Eur. J. Chem. Biol.* **13**, 105–111 (2012).
11. S. Rudiuk, K. Yoshikawa, D. Baigl, *Soft Matter*. **7**, 5854–5860 (2011).
12. Y. Zakrevskyy, E. Titov, N. Lomadze, S. Santer, *J. Chem. Phys.* **141**, 164904 (2014).
13. Y. Zakrevskyy, A. Kopyshev, N. Lomadze, E. Morozova, L. Lysyakova, N. Kasyanenko, S. Santer, *Phys. Rev. E*. **84**, 21909 (2011).
14. Y. Zakrevskyy, J. Roxlau, G. Brezesinski, N. Lomadze, S. Santer, *J. Chem. Phys.* **140**, 044907 (2014).
15. Y. Zakrevskyy, J. Roxlau, G. Brezesinski, N. Lomadze, S. Santer., *Adv. Funct. Mater.* **22**, 5000–5009 (2012).
16. M. Richter, Y. Zakrevskyy, M. Eisele, N. Lomadze, S. Santer, R. v. Klitzing, *Polymer* . **55**, 6513–6518 (2014).
17. S. Schimka *et al.*, *Phys. Chem. Chem. Phys.* **19**, 108–117 (2017).
18. A. M. Rumyantsev, S. Santer, E. Y. Kramarenko, *Macromolecules*. **47**, 5388–5399 (2014).
19. A. Kopyshev, C. J. Galvin, J. Genzer, N. Lomadze, S. Santer, *Langmuir*. **29**, 13967–13974 (2013).
20. A. Kopyshev, N. Lomadze, D. Feldmann, J. Genzer, S. Santer, *Polymer* . **79**, 65–72 (2015).
21. A. Kopyshev *et al.*, *ACS Appl. Mater. Interfaces*. **8**, 19175–19184 (2016).
22. A. Kopyshev, C. J. Galvin, J. Genzer, N. Lomadze, S. Santer, *Polymer (Guildf).* (2016).
23. L. Lysyakova *et al.*, *J. Phys. Chem. C*. **119**, 3762–3770 (2015).
24. Y. Zhao, T. Ikeda, *Smart Light-Responsive Materials: Azobenzene-Containing Polymers and Liquid Crystals* (John Wiley & Sons, 2009).
25. G. Zimmerman, L.-Y. Chow, U.-J. Paik, *J. Am. Chem. Soc.* **80**, 3528–3531

(1958).
26. D. L. Beveridge, H. H. Jaffé, *J. Am. Chem. Soc.* **88**, 1948–1953 (1966).
27. T. Hayashita, T. Kurosawa, T. Miyata, K. Tanaka, M. Igawa, *Colloid Polym. Sci.* **272**, 1611–1619 (1994).
28. L. Yang, N. Takisawa, T. Hayashita, K. Shirahama, *J. Phys. Chem.* **99**, 8799–8803 (1995).
29. H.-C. Kang, B. M. Lee, J. Yoon, M. Yoon, *J. Colloid Interface Sci.* **231**, 255–264 (2000).
30. B. Song, J. Zhao, B. Wang, R. Jiang, *Colloids Surfaces A Physicochem. Eng. Asp.* **352**, 24–30 (2009).
31. Y. Zakrevskyy, J. Roxlau, G. Brezesinski, N. Lomadze, S. Santer, *J. Chem. Phys.* **140**, 44906 (2014).
32. R. Lund, G. Brun, E. Chevallier, T. Narayanan, C. Tribet, *Langmuir*. **32**, 2539–2548 (2016).
33. K. Sakai, Y. Imaizumi, T. Oguchi, H. Sakai, M. Abe, *Langmuir*. **26**, 9283–9288 (2010).
34. R. Atkin, V. S. J. Craig, S. Biggs, *Langmuir*. **16**, 9374–9380 (2000).
35. R. Atkin, V. S. J. Craig, S. Biggs, *Langmuir*. **17**, 6155–6163 (2001).
36. R. Atkin, V. S. J. Craig, E. J. Wanless, S. Biggs, *Adv. Colloid Interface Sci.* **103**, 219–304 (2003).
37. Y. Zakrevskyy, J. Roxlau, G. Brezesinski, N. Lomadze, S. Santer, *J. Chem. Phys.* **140**, 44906 (2014).
38. X. Liu, N. L. Abbott, *J. Colloid Interface Sci.* **339**, 1–18 (2009).
39. P. Brown, C. P. Butts, J. Eastoe, *Soft Matter*. **9**, 2365 (2013).
40. D. Baigl, *Lab Chip*. **12**, 3637–3653 (2012).
41. J. Eastoe *et al.*, *Soft Matter*. **1**, 338–347 (2005).
42. H. Sakai *et al.*, *J. Am. Chem. Soc.* **127**, 13454–13455 (2005).
43. C. T. Lee, K. A. Smith, T. A. Hatton, *Macromolecules*. **37**, 5397–5405 (2004).
44. S. Chen, Y. Zhang, K. Chen, Y. Yin, C. Wang, *ACS Appl. Mater. Interfaces*. **9**, 13778–13784 (2017).
45. S. Chen, W. Zhang, C. Wang, S. Sun, *Green Chem.* **18**, 3972–3980 (2016).
46. A. Mamane, E. Chevallier, L. Olanier, F. Lequeux, C. Monteux, *Soft Matter*. **13**, 1299–1305 (2017).
47. E. Chevallier, A. Saint-Jalmes, I. Cantat, F. Lequeux, C. Monteux, *Soft Matter*. **9**, 7054–7060 (2013).
48. S. Chen, C. Wang, Y. Yin, K. Chen, *RSC Adv.* **6**, 60138–60144 (2016).
49. H. Sakai, A. Matsumura, S. Yokoyama, T. Saji, M. Abe, *J. Phys. Chem. B*. **103**, 10737–10740 (1999).
50. Y. Orihara *et al.*, *Langmuir*. **17**, 6072–6076 (2001).
51. R. F. Tabor *et al.*, *Soft Matter*. **5**, 78–80 (2009).
52. Lee C. Ted, K. A. Smith, T. A. Hatton, *Biochemistry*. **44**, 524–536 (2005).
53. J. Zou, F. Tao, M. Jiang, *Langmuir*. **23**, 12791–12794 (2007).
54. Y. Wang, H. Xu, X. Zhang, *Adv. Mater.* **21**, 2849–2864 (2009).
55. Y. Wang, N. Ma, Z. Wang, X. Zhang, *Angew. Chemie Int. Ed.* **46**, 2823–2826 (2007).
56. C. Lee, C. Cottin-Bizonne, R. Fulcrand, L. Joly, C. Ybert, *J. Phys. Chem. Lett.* **8**, 478–483 (2017).

57. A. Würger, *Phys. Rev. Lett.* **98**, 138301 (2007).
58. S. N. Varanakkottu, M. Anyfantakis, M. Morel, S. Rudiuk, D. Baigl, *Nano Lett.* **16**, 644–650 (2016).
59. D. M. Huang, C. Cottin-Bizonne, C. Ybert, L. Bocquet, *Phys. Rev. Lett.* **101**, 1–4 (2008).
60. N. Kavokine *et al.*, *Angew. Chemie*. **128**, 11349–11353 (2016).
61. S. N. Varanakkottu *et al.*, *Angew. Chemie Int. Ed.* **52**, 7291–7295 (2013).
62. C. for H. and N. Media *et al.*, *Langmuir*. **7**, 244501 (2017).
63. V. G. Levich, V. S. Krylov, *Annu. Rev. Fluid Mech.* **1**, 293–316 (1969).
64. B. A. Cicciarelli, T. A. Hatton, K. A. Smith, *Langmuir*. **23**, 4753–4764 (2007).
65. E. Chevallier, C. Monteux, F. Lequeux, C. Tribet, *Langmuir*. **28**, 2308–2312 (2012).
66. E. Chevallier *et al.*, *Soft Matter*. **7**, 7866–7874 (2011).
67. S. Kaneko, K. Asakura, T. Banno, *Chem. Commun.* **53**, 2237–2240 (2017).
68. A. Diguet *et al.*, *Angew. Chemie Int. Ed.* **48**, 9281–9284 (2009).
69. T. Shang, K. A. Smith, T. A. Hatton, *Langmuir*. **19**, 10764–10773 (2003).
70. J. Y. Shin, N. L. Abbott, *Langmuir*. **15**, 4404–4410 (1999).
71. J. Eastoe, M. S. Dominguez, P. Wyatt, A. Beeby, R. K. Heenan, *Langmuir*. **18**, 7837–7844 (2002).
72. E. Chevallier *et al.*, *Soft Matter*. **7**, 7866–7874 (2011).
73. E. Chevallier *et al.*, *Soft Matter*. **7**, 7866–7874 (2011).
74. A. Diguet, H. Li, N. Queyriaux, Y. Chen, D. Baigl, *Lab Chip*. **11**, 2666 (2011).
75. A. Venancio-Marques, F. Barbaud, D. Baigl, *J. Am. Chem. Soc.* **135**, 3218–3223 (2013).
76. L. Nurdin, A. Venancio-Marques, S. Rudiuk, M. Morel, D. Baigl, *Comptes Rendus Chim.* **19**, 199–206 (2016).
77. M. Anyfantakis, D. Baigl, *Angew. Chemie Int. Ed.* **53**, 14077–14081 (2014).
78. S. N. Varanakkottu *et al.*, *Angew. Chemie Int. Ed.* **52**, 7291–7295 (2013).
79. N. Kavokine *et al.*, *Angew. Chemie Int. Ed.* **55**, 11183–11187 (2016).
80. *Biological Physics - Energy, Information, Life* (W. H. Freeman and Company, New York, ed. 5, 2014).
81. E. M. Kramer, D. R. Myers, *Trends Plant Sci.* **18**, 195–197 (2013).
82. S. Marbach, H. Yoshida, L. Bocquet, *J. Chem. Phys.* **146**, 194701 (2017).
83. F. F. Reuss, *Mémoires la Société Impériale des Nat. Moskou*. **2**, 327–337 (1809).
84. S. Wall, *Curr. Opin. Colloid Interface Sci.* **15**, 119–124 (2010).
85. B. V Derjaguin, S. S. Dukhin, M. M. Koptelova, *Kolloidn. Zhurnal*, 53 (1961).
86. R. B. Schoch, J. Han, P. Renaud, *Rev. Mod. Phys.* **80**, 839–883 (2008).
87. H. J. Keh, *Curr. Opin. Colloid Interface Sci.* **24**, 13–22 (2016).
88. C. Lee *et al.*, *Phys. Rev. Lett.* **112**, 244501 (2014).
89. K.-L. Liu, J.-P. Hsu, S. Tseng, *Langmuir*. **29**, 9598–9603 (2013).
90. H. Yoshida, S. Marbach, L. Bocquet, *J. Chem. Phys.* **146**, 194702 (2017).
91. D. Dumont, T. V Galstian, S. Senkow, A. M. Ritcey, *Mol. Cryst. Liq. Cryst.* **375**, 341–352 (2002).
92. I. F. Sbalzarini, P. Koumoutsakos, *J. Struct. Biol.* **151**, 182–195 (2005).
93. M. D. Abràmoff, P. J. Magalhães, S. J. Ram, *Biophotonics Int.* **11**, 36–42 (2004).
94. MATLAB, *version 9.0 (R2016a)* (The MathWorks Inc., Natick, Massachusetts, 2016).

95. G. Sauerbrey, *Zeitschrift für Phys.* **155**, 206–222 (1959).
96. D. Johannsmann, *The Quartz Crystal Microbalance in Soft Matter Research* (Springer International Publishing, Cham, 2015;).
97. T. Young, *Philos. Trans. R. Soc. London*. **95**, 65–87 (1805).
98. A. M. Worthington, *Proc. R. Soc. London*. **32**, 362–377 (1881).
99. A. Ferguson, *Philos. Mag. Ser. 6*. **23**, 417–430 (1912).
100. P. S. marquis de Laplace, *Traité de mécanique céleste* (Chez J.B.M. Duprat, 1805).
101. C. F. Gauss, *Principia generalia theoriae figurae fluidorum in statu aequilibrii.* (Gottingae, 1830).
102. J. D. Berry, M. J. Neeson, R. R. Dagastine, D. Y. C. Chan, R. F. Tabor, *J. Colloid Interface Sci.* **454**, 226–237 (2015).
103. N. S. Yadavalli, T. König, S. Santer, *J. Soc. Inf. Disp.* **23**, 154–162 (2015).
104. R. H. Müller, *Zetapotential und Partikelladung in der Laborpraxis: Einführung in die Theorie, Praktische Meßdurchführung, Dateninterpretation.* (Wissenschaftliche Verlagsgesellschaft, Stuttgart, mit 122 Ab., 1996;).
105. P. Debye, E. Hückel, *Phys. Zeitschrift*. **24**, 185–206 (1923).
106. J. C. W. Corbett, F. McNeil-Watson, R. O. Jack, M. Howarth, *Colloids Surfaces A Physicochem. Eng. Asp.* **396**, 169–176 (2012).
107. A. Ashkin, *Phys. Rev. Lett.* **24**, 156–159 (1970).
108. A. Ashkin, J. M. Dziedzic, J. E. Bjorkholm, S. Chu, *Opt. Lett.* **11**, 288–290 (1986).
109. D. Feldmann, S.R. Maduar, M. Santer, N. Lomadze, O.I. Vinogradova, S. Santer, *Sci. Rep*. **6** (2016) 36443.
110. D. C. Grahame, *Chem. Rev.* **41**, 441–501 (1947).
111. J. Israelachvili, *Intermolecular and Surface Forces*, 3rd Edition | Jacob Israelachvili | ISBN 9780123919274 (2016).
112. A. D. Polyanin, *Handbook of Linear Partial Differential Equations for Engineers and Scientists* (CRC Press, 2001).
113. A. Diguet, R.-M. Guillermic, N. Magome, A. Saint-Jalmes, Y. Chen, K. Yoshikawa, D. Baigl, *Angew. Chemie Int. Ed.* **48** (2009) 9281–9284.
114. S. B. Velegol, B. D. Fleming, S. Biggs, E. J. Wanless, R. D. Tilton, *Langmuir*. **16**, 2548–2556 (2000).
115. G. Némethy, H. A. Scheraga, *J. Chem. Phys.* **36**, 3401–3417 (1962).
116. G. Stainsby, A. E. Alexander, *Trans. Faraday Soc.* **46**, 587–597 (1950).
117. R. H. Aranow, L. Witten, *J. Phys. Chem.* **64**, 1643–1648 (1960).
118. J. C. Ramirez, A. T. Conlisk, *Biomed. Microdevices*. **8**, 325–330 (2006).
119. R. Zhang, P. Somasundaran, *Langmuir*. **21**, 4868–4873 (2005).
120. R. Zhang, C. Liu, P. Somasundaran, *J. Colloid Interface Sci.* **310**, 377–384 (2007).
121. R. Atkin, V. S. J. Craig, E. J. Wanless, S. Biggs, *J. Phys. Chem. B*. **107**, 2978–2985 (2003).
122. R. Atkin, V. S. J. Craig, E. J. Wanless, S. Biggs, *J. Colloid Interface Sci.* **266**, 236–244 (2003).
123. M. J. Rosen, *J. Am. Oil Chem. Soc.* **52**, 431–435 (1975).
124. R. Zhang, P. Somasundaran, (2006), doi:10.1016/j.cis.2006.07.004.
125. A. Doren, D. Vargas, J. Goldfarb, *J Inst Met. Trans, Sect C*. **73**, 34 (1975).

126. J. Leimbach, H. Rupprecht, *Colloid Polym. Sci.* **271**, 307–309 (1993).
127. A. Adak, M. Bandyopadhyay, A. Pal, *J. Environ. Sci. Heal. Part A*. **40**, 167–182 (2005).
128. J. M. Cases, F. Villiéras, L. J. Michot, J. L. Bersillon, *Colloids Surfaces A Physicochem. Eng. Asp.* **205**, 85–99 (2002).
129. S. Paria, K. C. Khilar, *Adv. Colloid Interface Sci.* **110**, 75–95 (2004).
130. D. W. Fuerstenau, *J. Colloid Interface Sci.* **256**, 79–90 (2002).
131. J.-F. Liu, G. Min, W. A. Ducker, *Langmuir*. **17**, 4895–4903 (2001).
132. J. C. Schulz, G. G. Warr, P. D. Butler, W. A. Hamilton, *Phys. Rev. E*. **63**, 41604 (2001).
133. K. Sakai *et al.*, *Colloids Surfaces A Physicochem. Eng. Asp.* **410**, 119–124 (2012).
134. J. J. R. Stålgren, J. Eriksson, K. Boschkova, *J. Colloid Interface Sci.* **253**, 190–195 (2002).
135. F. Tiberg, J. Brinck, L. Grant, *Curr. Opin. Colloid Interface Sci.* **4**, 411–419 (1999).
136. E. Tyrode, M. W. Rutland, C. D. Bain, *J. Am. Chem. Soc.* **130**, 17434–17445 (2008).
137. M. M. Knock, L. S. Sanii, in *Amphiphiles: Molecular Assembly and Applications* (American Chemical Society, 2011), vol. 1070 of *ACS Symposium Series*, pp. 175–192.
138. C. Gutig, B. P. Grady, A. Striolo, *Langmuir*. **24**, 13814 (2008).
139. P. Somasundaran, D. W. Fuerstenau, *J. Phys. Chem.* **70**, 90–96 (1966).
140. Y. Gao, J. Du, T. Gu, *J. Chem. Soc. Faraday Trans. 1 Phys. Chem. Condens. Phases*. **83**, 2671–2679 (1987).
141. T. P. Goloub, L. K. Koopal, *Langmuir*. **13**, 673–681 (1997).
142. X. Zhang, B. Chen, Z. Wang, *J. Colloid Interface Sci.* **313**, 414–422 (2007).
143. S. C. Howard, V. S. J. Craig, **5**, 3061–3069 (2009).
144. R. F. Tabor, J. Eastoe, P. J. Dowding, *J. Colloid Interface Sci.* **346**, 424–428 (2010).
145. S. Manne, H. E. Gaub, *Science (80-.).* **270**, 1480–1482 (1995).
146. G. Fragneto, Z. X. Li, R. K. Thomas, A. R. Rennie, J. Penfold, *J. Colloid Interface Sci.* **178**, 531–537 (1996).
147. M. Duan, H. Wang, S. Fang, Y. Liang, *J. Colloid Interface Sci.* **417**, 285–292 (2014).
148. P. Wängnerud, G. Olofsson, *J. Colloid Interface Sci.* **153**, 392–398 (1992).
149. C. A. Keller, B. Kasemo, *Biophys. J.* **75**, 1397–1402 (1998).
150. E. Reimhult, F. Höök, B. Kasemo, *Langmuir*. **19**, 1681–1691 (2003).
151. Formation of Solid-Supported Lipid Bilayers: An Integrated View - Langmuir (ACS Publications).
152. J. N. Israelachvili, D. J. Mitchell, B. W. Ninham, *J. Chem. Soc. Faraday Trans. 2*. **72**, 1525 (1976).
153. *Colloids and Surfaces*. **37**, 245–268 (1989).
154. I. Reviakine, D. Johannsmann, R. P. Richter, *Anal. Chem.* **83**, 8838–8848 (2011).
155. S. X. Liu, J.-T. Kim, *Desalination*. **247**, 355–361 (2009).
156. R. G. Alargova *et al.*, *Langmuir*. **14**, 1996–2003 (1998).

157. *J. Colloid Interface Sci.* **256**, 23–32 (2002).
158. R. Zimmermann, S. Dukhin, C. Werner, *J. Phys. Chem. B*. **105**, 8544–8549 (2001).
159. A. M. Rumyantsev, S. Santer, E. Y. Kramarenko, *Macromolecules*. **47**, 5388–5399 (2014).
160. A. Majee, *Eur. Phys. J. E*. **40**, 30 (2017).
161. R. Golestanian, T. B. Liverpool, A. Ajdari, *Phys. Rev. Lett.* **94**, 220801 (2005).
162. R. Golestanian, T. B. Liverpool, A. Ajdari, *New J. Phys.* **9**, 126–126 (2007).
163. J. R. Howse *et al.*, *Phys. Rev. Lett.* **99**, 048102 (2007).
164. B. Bhushan, M. Nosonovsky, Y. C. Jung, in *Nanotribology and Nanomechanics* (Springer Berlin Heidelberg, 2008.
165. A. Lafuma, D. Quéré, *Nat. Mater.* **2**, 457–460 (2003).
166. S. Brunauer, P. H. Emmett, E. Teller, *J. Am. Chem. Soc.* **60**, 309–319 (1938).
167. S B. J. Berne and R. Pecora, *Dynamic Light Scattering* (John Wiley, New York, 1976)
168. M. Montagna, O. Guskova, *Langmuir*, ***34***(1), 311–321 (2018).

ACKNOWLEDGEMENT

Danken möchte ich allen Menschen, die mich auf dem Weg zur Dissertation wissenschaftlich und persönlich unterstützt haben und von denen ich viel lernen konnte. Sehr vielen Menschen bin ich dankbar, kann aber nur einige nennen.

Auf wissenschaftlicher Seite danke ich besonders Prof. Dr. Svetlana Santer für die gute Betreuung während der Forschung, der ungezählten wertvollen Diskussionen, die Offenheit für neue Ideen, ihr Vertrauen in meine Fähigkeiten und generell die vielfältig bereichernde Unterstützung.

Danken möchte ich Pooja Arya, vor allem für die experimentelle Unterstützung in Bezug auf poröse Partikel, für ihren unermüdlichen Antriebswillen und für die vielen Diskussionen.

Maren Umlandt möchte ich für die experimentelle Unterstützung im Bereich QCM danken sowie für die gute Büronachbarschaft.

Ohne die Synthetisierung des Azo-Tensids wäre die Forschung nicht möglich gewesen. Dafür bin ich Dr. Nino Lomadze sehr dankbar sowie für ihre umfangreiche experimentelle Hilfe.

Ich danke der gesamten Gruppe um Prof. Dr. Carsten Beta, besonders Oliver Nagel, Dr. Marius Hintsche und Dr. Mathias Gerhardt. Ohne den Mikroskopaufbau hätte ich die Experimente nicht durchführen können.

Für Diskussionen um das Thema LDDO und die gemeinsame Entwicklung der Theorie danke ich Prof. Dr. Olga Vinogradova und insbesondere Dr. Salim Maduar, den ich zwar nie persönlich getroffen habe, aber mit dem ich zahlreiche sehr konstruktive Skypegespräche geführt habe.

Dem Max-Planck-Institut für Kolloid- und Grenzflächenforschung danke ich für die Nutzung der QCM-D, hier insbesondere Dr. Emanuel Schneck (Physics of Biomolecular Interfaces), Dr. Klaas Bente sowie Anna Pohl.

Mein Dank gilt Dr. Alexey Kopyshev, sowohl für die experimentelle als auch für die mediale Unterstützung.

Danken möchte ich außerdem meiner ganzen Arbeitsgruppe Experimentalphysik und meinen Doktorandenkollegen Joachim Jelken, Sarah Löbner und Selina Schimka sowie Dr. Nataraja Sekhar Yadavalli, die mir immer mit Rat und Tat zur Seite standen.

Außerdem möchte ich Dr. Juri Zakrevski danken, der trotz seines Weggangs aus der Arbeitsgruppe stets ein offenes Ohr für wissenschaftliche Diskussionen hatte.

Für die finanzielle Förderung danke ich dem Helmholtz-Zentrum Geesthacht für das Stipendium sowie der Universität Potsdam für die Anstellung als Mitarbeiter im Bereich Polymer Science.

Zum Abschluss möchte ich meiner Familie und insbesondere meinen Eltern danken, die mich in jedweder Hinsicht auf meinem Weg durch das Studium begleitet und unterstützt haben.

Außerdem danke ich meinen Freunden, vor allem Dr. Ulrich Hörmann für den persönlichen und wissenschaftlichen Austausch sowie für seine Korrekturhilfe.

Besonders möchte ich meiner Partnerin und Freundin Romy danken, die mir in schweren Zeiten immer motivierend zur Seite steht und stets ein fröhliches Wort, offenes Ohr und eine liebevolle Umarmung für mich parat hat.

DECLARATION

Hiermit versichere ich, dass ich die vorliegende Arbeit selbstständig angefertigt und keine anderen als die in der Dissertation angegebenen Quellen und Hilfsmittel benutzt habe. Alle Stellen der Arbeit, die ich aus diesen Quellen und Hilfsmitteln dem Wortlaut oder dem Sinne nach entnommen habe, sind kenntlich gemacht und im Literaturverzeichnis aufgeführt. Weiterhin versichere ich, dass weder ich noch andere diese Arbeit in gleicher oder ähnlicher Fassung an keiner anderen Hochschule eingerecht haben.

Potsdam, den 06.06.2018

David Feldmann